SYNTHETIC-APERTURE RADAR IMAGING OF THE OCEAN SURFACE: THEORETICAL CONSIDERATIONS, AND EXPERIMENTS WITH SIMULATED AND ACTUAL SAR IMAGERY

By

PARIS W. VACHON

B.A.Sc., The University of British Columbia, 1983

A THESIS SUBMITTED IN PARTIAL FULFILLMENT OF

THE REQUIREMENTS FOR THE DEGREE OF

DOCTOR OF PHILOSOPHY

in

THE FACULTY OF GRADUATE STUDIES

(Department of Oceanography)

We accept this thesis as conforming

to the required standard

THE UNIVERSITY OF BRITISH COLUMBIA

August 1987

In presenting this thesis in partial fulfilment of the requirements for an advanced degree at the University of British Columbia, I agree that the Library shall make it freely available for reference and study. I further agree that permission for extensive copying of this thesis for scholarly purposes may be granted by the head of my department or by his or her representatives. It is understood that copying or publication of this thesis for financial gain shall not be allowed without my written permission.

Department of Oceanography

The University of British Columbia
1956 Main Mall
Vancouver, Canada
V6T 1Y3

Date 87-09-21

Abstract

Three key areas of controversy in synthetic-aperture radar (SAR) imaging of ocean surface waves are considered: first, the nature of Bragg scattering; second, the role, magnitude, and calculation of the scene coherence time; and third, the relevant ocean wave velocities for coherent Doppler modulations.

This work begins with a re-derivation and extension of existing SAR imaging theory for point and diffuse targets. Generic, relatively simple, closed-form expressions for the impulse response, the resolution, and the image bandwidth summarize this unified treatment. Theoretical differences between the imagery of point and diffuse targets are pointed out. Based upon these fundamental differences, a statistical testing procedure is formulated to address the question of scene target density.

Background ocean surface wave theory is outlined in preparation for discussions of SAR ocean imaging. Of central importance is the role of the phase velocity, which is the speed of translation of the mean pattern of reflectivity, and the orbital motion, which leads to coherent (phase) modulation, and hence to velocity bunching, acceleration defocus, and target decorrelation.

Based upon this theoretical background, one- and two-dimensional simulation models are developed. The one-dimensional simulation addresses the effects of various parameters upon the mean image contrast in a velocity bunching model and guides the development of the two-dimensional simulation. The two-dimensional simulation is unique because each target which constitutes the scene is explicitly considered. This leads to a degree of control and flexibility which is not available from actual SAR imagery.

Qualitative and quantitative comparisons are drawn between the simulated and actual SAR imagery to address the key areas of controversy. The assertion that Bragg scattering is a coherent process is defended, despite inability to conclusively verify this

using SEASAT data. Comparisons between simulation and C-SAR imagery of waves propagating into ice verify the roles of the scene coherence time and the wave phase velocity.

Contents

List of Tables

List of Figures

List of Symbols

a	radial component of point target acceleration (page 15)
A	ocean wave amplitude (page 35)
$a(t)$	real, zero-mean, wide-sense stationary Gaussian random variable (page 29)
$b(t)$	real, zero-mean, wide-sense stationary Gaussian random variable (page 29)
B	Doppler bandwidth (page 6)
c	subscript denoting the complex impulse response (page 107)
C	contrast function (page 143)
C_g	ocean wave group velocity (page 54)
C_p	ocean wave phase velocity (page 35)
d	subscript denoting a dynamic target (page 17)
E	ratio of peak defocus contributions of along track orbital velocity to the radial acceleration (page 49)
f	azimuthal Doppler frequency coordinate (page 8)
f_D	Doppler frequency shift (page 19)
f_s	sampling frequency (page 108)
$f(t)$	scene contrast function (page 5)
g	gravitational constant
$g(t)$	output SAR image (page 5)
h	platform height (page 6) or water depth (page 35)
$h(t)$	compression filter (page 5)
H_s	ocean wave significant waveheight ($2\sqrt{2}A$ for a sinusoidal wave) (page 39)
i	subscript denoting the i^{th} look of a multi-look set (page 9)
I	intensity value (page 143)
j	$\sqrt{-1}$
k	radar wavenumber (page 6)
K	the inverse of the square of the fractional reduction in bandwidth due to application of the processing and look-extraction windows (page 11) or ocean wavenumber (page 35)
K_a	azimuth FM rate (page 8)
K_{emh}	electromagnetic-hydrodynamic separation wavenumber (page 42)
K_B	Bragg resonance wavenumber (page 36)
L	the inverse of the square of the fractional reduction in bandwidth due to application of the processing filter window (page 11)
$l(t)$	look extraction filter (page 10)
m	subscript denoting multi-look processing (page 12)
M	the inverse of the square of the fractional reduction in processor bandwidth due to the look-extraction window (page 17) or the number of looks summed of an N-look set (page 65)
MSVR	mean-squared-to-variance ratio (page 29)
N	number of looks processed (page 14)
N_0	power spectral density of a white Gaussian process (page 29)
$n(t)$	white Gaussian noise process (page 5)
p	area of the squared look extraction window (page 12)
PRF	pulse repetition frequency (page 108)
$R(t)$	target range (page 6)
R_0	target range of closest approach (page 6)
$R_\nu(\tau)$	autocorrelation function of the process ν (page 20)

s	subscript denoting a static target (page 10)
$S_\nu(f)$	power spectral density function of the process ν (page 20)
t	azimuthal temporal coordinate (page 8)
t_D	azimuthal temporal Doppler shift (page 17)
t_i	look extraction filter centre time (page 9)
T	available coherent integration time (page 6)
T_l	look extraction filter time extent (page 9)
T_p	compression filter time extent (page 9)
T_w	ocean wave period (page 35)
u	azimuthal component of point target velocity (page 15)
U	wind speed at 19.5 m (page 39)
v	radial component of point target velocity (page 15)
v_E	velocity of the envelope of mean reflectivity (page 57)
v_{rms}	root-mean-square radial velocity component (page 22)
V	platform velocity (page 6)
V_s	ship velocity (page 54)
$w(t)$	azimuth prefilter which includes antenna pattern weighting and Doppler encoding (page 5)
$w_m(t)$	azimuthal antenna pattern (page 6)
W	Weber number (page 36)
W_d	image bandwidth for a diffuse target (page 30)
W_p	image bandwidth for a point target (page 31)
x	azimuthal spatial coordinate (page 8)
α	velocity bunching parameter (page 47)
β	azimuthal antenna pattern beamwidth (page 6)
$\beta(t)$	multiplicative phase term (page 17)
γ	angle of incidence (page 37)
ϵ_d	processor decimation factor (page 105)
ϵ_u	processor interpolation factor (page 105)
ς	vertical displacement of the ocean surface (page 35)
η	fractional azimuthal processor quadratic phase error (page 9)
η_r	fractional range processor quadratic phase error (page 108)
$\hat{\eta}$	fractional scene-induced quadratic phase error (page 17)
$\theta(t)$	wide sense stationary random phase process (page 20)
λ	radar wavelength (page 6)
Λ	ocean wavelength (page 35)
μ	narrow "V" ship wake half-angle (page 54)
ξ	fractional look overlap (page 105)
ρ	azimuthal temporal (or spatial) resolution (page 11) or water density (page 35)
σ	received power (proportional to the radar cross-section) (page 10) or surface tension (page 35)
σ_{rel}	relative radar cross-section (page 120)
τ_c	scene coherence time scale (page 22)
ϕ	angle between ocean wavenumber vector and platform velocity vector (page 44)
ϕ_l	angle between line of targets and platform velocity vector (page 54)
$\chi(t,f)$	ambiguity function (page 22)
ψ	point target intrinsic phase (page 6)
Ψ	point target phase history (page 6)

Ω ocean wave radian frequency (page 35)

Acknowledgements

Many individuals and organizations must be thanked for help given in the production of this thesis.

My supervisory committee, consisting of Dr. W.J. Emery, Prof. P.H. LeBlond, Mr. P.R. McConnell, Mr. D.J. Okerson, and Dr. R.K. Raney, offered guidance, expertise, and encouragement throughout. Dr. R.K. Raney is particularly thanked for the patience exhibited throughout our numerous discussions and in reviewing many working papers and early drafts of this thesis.

More SAR data has been examined than actually appears in this thesis. I am grateful for the opportunity, and wish to thank: Mr. J. Princz, Mr. G. Choma and their colleagues at data processing (CCRS); Dr. C. Elachi and Dr. J. Curlander (JPL); Dr. I. Cumming, Mr. P. Hasan, and Ms. P. Kavanagh (MDA); Mr. A. Haskell and Mr. M. Elkington (RAE); and the LIMEX/LEWEX experimental team.

This work began at the Satellite Oceanography Laboratory at UBC when it was under the direction of Dr. W.J. Emery, and concluded at the RADARSAT Project Office, thanks to the special interest shown by Dr. N.G. Freeman. Staff at both locations must be thanked for their support and the contribution of their expertise and resources. Particular thanks goes to Dr. R. O'Neil.

Personal funding came at various times from an NSERC post-graduate scholarship, teaching assistanceships while at UBC, a DSS contract, and through F.G. Bercha & Assoc. (Ont.) Ltd..

A special thanks for support and encouragement are directed towards my wife Cathy, and our son Philippe. This work is dedicated to them.

1 Introduction

High resolution synthetic-aperture radar (SAR) systems, such as that carried aboard SEASAT or those planned for inclusion in the ERS-1 and RADARSAT payloads, potentially provide the opportunity to measure ocean surface features on spatial and temporal scales never before realized. Such systems are not limited to oceanic research, but can also supply operational measurements on a global scale. However, the ocean imagery produced by this active microwave instrument is not well understood at this time and is subject to controversy in the relevant oceanographic and engineering communities. Problems have arisen in several areas—conflicting hypotheses and interpretations of SAR ocean data sets are frequently encountered.

The following questions summarize the key areas of controversy in current SAR research into the imaging of ocean surface gravity waves:

1. Given that Bragg resonant scattering is the dominant ocean scattering mechanism, is the nature of this scattering specular or diffuse?

2. What is the size and role of the scene coherence time in the degradation of SAR resolution in the presence of surface gravity waves?

3. Is the phase velocity or the orbital velocity the relevant velocity for coherent Doppler modulations?

This thesis does not purport to fully answer each of these key questions. However, each of them is addressed from three points of view: first, via careful re-derivation and extension of the relevant theory for SAR imaging of point and diffuse targets; second, by one- and two-dimensional simulations of certain image phenomena; and third, by comparison of the simulation results with actual SAR imagery.

As an aid in understanding the processes involved in SAR ocean surface imaging, a two-dimensional simulation package has been developed. In the simulation procedure,

careful account is taken of the scene scattering nature; there are no *a priori* assumptions as to the statistical behaviour of each resolution element, and each point target in the scene is explicitly considered. A corresponding degree of control and flexibility is not available when studying actual SAR imagery.

Chapters 2, 3, 4, 5, and 6 provide the theoretical foundations necessary to understand the SAR, its interaction with a dynamic distributed scene, and the simulation model developed for this work. Chapter 2 discusses point target imaging theory starting from the simple case of a static point target, then incorporating target dynamics, and finally target partial coherence. Results are expressed in terms of closed form expressions based upon generic Gaussian weighting functions and fundamental SAR parameters. Many of the expressions which result are new.

Chapter 3 discusses diffuse target imaging theory. The diffuse target is modelled as a dense array of statistically independent point targets. Certain key statistics are derived. Differences between point and diffuse targets which may be quantitatively measured are summarized.

Chapter 4 is a brief summary chapter which outlines background oceanographic information relevant to radar imaging of the ocean. Chapter 5 provides the theory for SAR imaging of surface gravity waves. Scattering mechanisms, the role of the orbital and phase velocity, and calculation of the coherence time are discussed. Two special SAR image cases are considered: ocean waves in an ice-covered sea, a case in which the high frequency image disturbing components are suppressed; and narrow "V" ship wakes, a case in which a line of Bragg targets are explicitly observed. Both of these cases allow new insights into the phenomena of interest.

Chapter 6 continues the discussion of Chapter 5 but focusses upon the imaging of translating patterns of reflectivity, specifically contrasting coherent and noncoherent velocity effects upon the SAR image. New results are offered at this level of discussion.

The analysis methodology is outlined in Chapter 7. Included are the role of the

simulations and implementation of the distinctions between point and diffuse target imagery to test for the presence of each target type.

Comparisons between simulated and actual SAR imagery are performed in Chapter 8. The actual SAR data sets consist of C-band airborne SAR imagery obtained during the Labrador Extreme Waves Experiment (LEWEX) (1987) and L-band satellite SAR imagery from SEASAT (1978). Comparisons are made to study target density, scene coherence time, and noncoherent scene motions. These comparisons directly address the three areas of controversy.

Details of the simulation methodologies and analysis results along with a few supporting discussions are relegated to appendices.

By its inherent nature, the study undertaken in this work is multi-disciplinary. This presents numerous problems with notation and terminology; the list of symbols included in this work should be helpful. Local usage of specific symbols is explicitly indicated. Note that the radar wave parameters are given lower case symbols, while ocean wave parameters are given upper case symbols. So as not to compromise content for readers from either an oceanographic or radar background, relevant terminology is underlined in the text and defined in the Glossary, and essential features from both disciplines are reviewed in the text.

This Introduction offers only a very brief assessment of the state of the art in SAR observation of the ocean surface. It has been a challenging and active research area, particularly for the past ten years. Whereas it is beyond the scope of this Introduction to describe in more detail the situation, known and controversial issues together with commentary on the relevant literature are addressed in the chapters which follow.

2 SAR Point Target Imaging

Abstract

This Chapter discusses the SAR image of an isolated point target, which is proportional to the scene/SAR/processor impulse response. The scene itself has an impact on the impulse response through resolution degradation associated with target motion and partial coherence. The SAR, that is the actual radar mechanism, imposes weighting and Doppler encoding which dictate the best possible resolution. The processor has an impact on the resolution and may impose system partial coherence. Explicit generic forms for the impulse response based upon Gaussian weighting functions are presented. The first order effects of target motion, target partial coherence, processor focus, and processor partial coherence are formulated and discussed. Results are summarized in terms of the single-look of a multi-look set and multi-look impulse responses, and in terms of the impact upon the point target resolution. Contributions consist of a unified treatment of a variety of fundamental cases and the concept of coherence time-bandwidth product as a measure of potential coherent processing support.

The output of a SAR is mathematically tractable in closed form for two distinct target types: first, an isolated point target; and second, a diffuse target consisting of a dense distribution of statistically independent point targets. The SAR image of an isolated point target is the subject of this Chapter. This image is proportional to the scene/SAR/processor impulse response (or point spread function) from which we may infer fundamental performance measures such as the system resolution. We treat static, dynamic, and partially coherent point targets in this Chapter.

2.1 Static Point Target

A SAR is an imaging radar system which achieves a high spatial resolution in both the range (across track) and the azimuth (along track) directions [11,19,78]. High range resolution is achieved by using pulse compression techniques [35]. High azimuthal resolution is achieved by scanning the radar via the platform vehicle motion, storing the amplitude and phase structure thus imposed upon the target returns, and subsequently focussing or compressing the stored data. Azimuthal processing is analogous to range compression, but is a function of range, and is scaled very differently in time. The range scanning is at the speed of light, while the azimuthal scanning is at the speed of the carrier vehicle. This leads to a substantial decoupling of the range and azimuthal

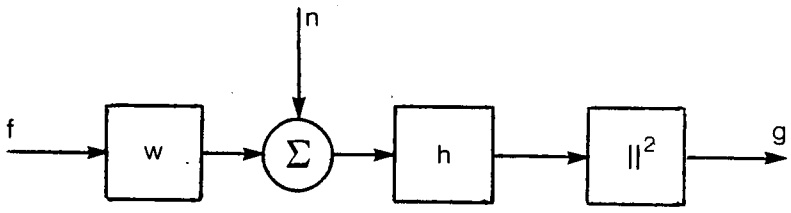

Figure 1: Block diagram for the SAR azimuthal channel.

dimensions for processing purposes (ignoring range migration and curvature effects). In the ensuing discussion, the azimuthal channel is implied, if not explicitly stated. The azimuthal channel is of direct relevance to the dynamic problems encountered in oceanic imaging because the time scales between the system and the scene are of the same order. These are problems to which the range channel is largely immune.

2.1.1 System Description

A compact analysis for the SAR imaging process is based upon a linear convolution model [11,19,88] in which an image $g(t)$ is formed by taking the magnitude squared of (detecting) the output of the convolution of an appropriate prefilter $w(t)$ and processing filter $h(t)$ over an input scene function $f(t)$ (Fig. 1). Then, we may write

$$g(t) = |f(t) * w(t) * h(t) + n(t) * h(t)|^2 \ , \tag{1}$$

where $n(t)$ is the receiver noise. If $n(t)$ is zero-mean white Gaussian noise, which is statistically independent of the signal, then the optimum processing filter for azimuthal compression (from a signal to noise ratio point of view) is the matched filter [49]:

$$h(t) = \overline{w(-t)} \ . \tag{2}$$

The prefilter $w(t)$ consists of two parts: phase encoding due to the platform motion past the target, and amplitude weighting due to the azimuthal antenna pattern. The phase history of a given point target is

$$\Psi(t) = -2kR(t) + \psi \ , \tag{3}$$

where $k = 2\pi/\lambda$ is the radar wavenumber, λ is the radar wavelength, and ψ is the target's intrinsic phase which is introduced upon reflection.

From the SAR geometry of Fig. 2, if the azimuthal antenna beamwidth β (radians) is small, for the flat earth case with broadside antenna pointing, the range for a static target is given approximately by

$$R(t) \approx R_0 + \frac{V^2 t^2}{2R_0} \ , \tag{4}$$

where R_0 is the target range of closest approach, and V is the platform velocity. The appropriate prefilter (up to a constant phase term) may then be written

$$w(t) = \exp\left\{-j\pi \frac{B}{T} t^2\right\} \cdot w_m(t) \ , \tag{5}$$

where $w_m(t)$ is the azimuthal antenna pattern. The quadratic phase modulation (its length, rate, and possible perturbations) is the most important aspect of the prefilter and form the focus of the work of this Chapter. The available coherent integration time T and the Doppler bandwidth B are fundamental parameters. The upper limit of coherent integration time available to the processor is determined by the antenna beamwidth. In this model, the width of $w_m(t)$ is[1]

$$T = \frac{R_0 \beta}{V} \quad \text{(sec)}. \tag{6}$$

The corresponding Doppler bandwidth is[2]

$$B = \frac{2V\beta}{\lambda} \quad \text{(hz)}. \tag{7}$$

[1] If dealing with a satellite SAR, the roles of footprint velocity and spacecraft velocity must be treated carefully, and used appropriately in these expressions [65]. Replace V with the footprint velocity V_f in equation (6).

[2] If dealing with a satellite SAR, replace V with the spacecraft velocity $V_{s/c}$ [65] in equation (7). V_f and $V_{s/c}$ could differ by 15% for a typical low Earth orbit SAR.

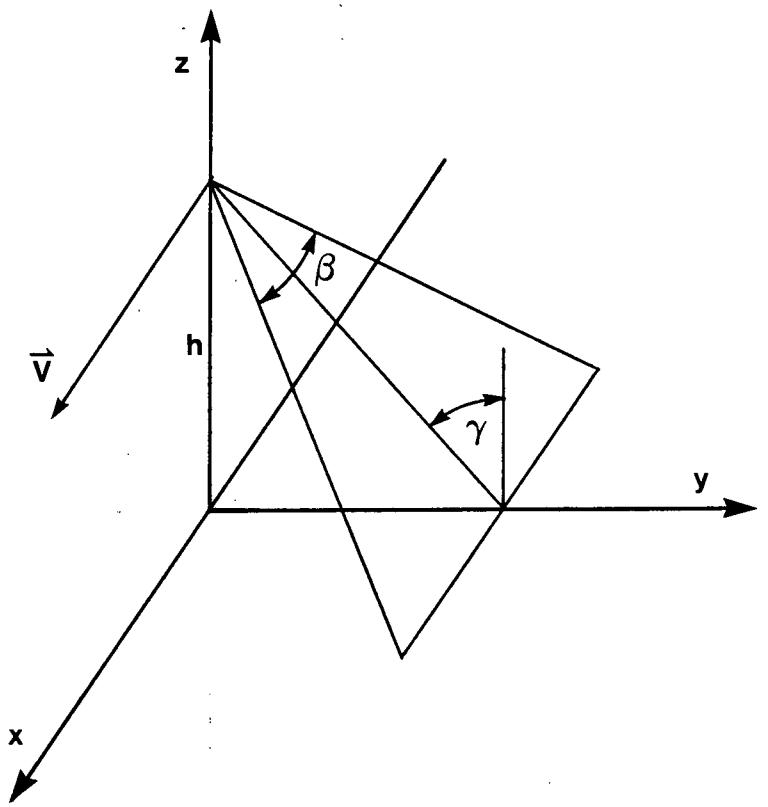

Figure 2: SAR geometry.

The quadratic phase of the azimuthal prefilter leads to a linear frequency modulated encoding of FM rate

$$K_a = \frac{B}{T} = \frac{2V^2}{\lambda R_0} . \tag{8}$$

For practical SAR systems, the time-bandwidth product

$$TB = \frac{2R_0\beta^2}{\lambda} \tag{9}$$

satisfies $TB \gg 1$, a property which allows significant simplifications in analysis through use of the principle of stationary phase [36]. The time-bandwidth product represents the improvement in resolution which may be afforded through coherent processing. (Impulse response-type functions generally satisfy $TB \sim 1$ suggesting that such signals will not support coherent processing for improved resolution.)

In the formulations in this work, the azimuthal spatial coordinate x is related to the azimuthal time coordinate t, and to the azimuthal Doppler frequency coordinate f (if $TB \gg 1$) via

$$x = Vt = V\frac{f}{K_a} , \tag{10}$$

for a static target. This property sets the static impulse response apart from the dynamic impulse response where the azimuthal coordinate may be modified by the target's motion parameters. This is of central interest in this work. Equation (10) shows that the azimuthal time coordinate is proportional to the Doppler frequency, a property specific to large time-bandwidth product signals. It turns out that this is a contributing factor to some of the controversy in the SAR ocean wave imaging problem. Appreciating this relationship helps to resolve an apparent paradox (see Chapter 6).

It is convenient to introduce an explicit generic form for the azimuthal antenna pattern. A convenient choice which represents the antenna pattern's main lobe reasonably well, and allows simple closed form expressions to be found for the SAR/processor

impulse response and resolution, is Gaussian amplitude weighting[3]:

$$w_m(t) = \exp\left\{-\pi\frac{t^2}{T^2}\right\} . \tag{11}$$

The time extent T of this form may be calculated using an equivalent rectangular width[4] norm.

The processing filter, though nominally matched, may contain departures from its ideal form. There is a potential mismatch between the prefilter and processing filter azimuthal FM rates, referred to as a focus error or a quadratic phase error. Such a condition could arise intentionally or accidentally, and always occurs to some degree near segment edges in digital SAR processors which operate in a range-segment mode [9]. Another departure could be in the actual time (hence frequency) weighting of the processing filter. In keeping with our use of generic Gaussian weighting functions, the processing filter may be written

$$h(t) = \exp\left\{-\pi\frac{t^2}{T_p^2}\right\} \cdot \exp\left\{j\pi\frac{B}{T}(1+\eta)t^2\right\} , \tag{12}$$

where T_p is the time extent of the processing filter and η is the fractional error in the processor FM rate[5].

The processing filter is frequently operated in a multi-look mode. That is, N portions of the Doppler spectrum, say those centred at times t_i and of time extent T_l,

[3]It should be noted that some authors [4,77] use

$$w_m(t) = \exp\left\{-2\frac{t^2}{T_a^2}\right\},$$

to define the azimuthal antenna pattern. This form and equation (11) are identical if $T_a = \sqrt{2/\pi}\,T$. The Doppler bandwidth should also be correspondingly scaled when interpreting results derived from these sources.

[4]The equivalent rectangle is the width of the rectangle of height equal to the maximum value and containing the same area. That is

$$\rho = \frac{\int g(t)\,dt}{g(0)}.$$

For a Gaussian function, this resolution measure is related to the full-width-at-half-max (FWHM) by $\rho_{\mathrm{FWHM}} = 0.94\rho$, to the radius-of-gyration by $\rho_{\mathrm{rg}} = 0.80\rho$, and to the standard deviation by $\sigma = 0.40\rho$.

[5]The fractional processor FM rate error is occasionally written as $(1+\eta')^2$ rather than $(1+\eta)$. Then, in the event of a small focus error, these formulations are related by $\eta = 2\eta'$.

are coherently processed, detected, and summed to produce the SAR image. Such a partially coherent processing scheme uses ensemble averaging to trade speckle smoothing (radiometric fidelity) for spatial resolution (see Chapter 3). Each portion of the Doppler spectrum so processed is called a look, and this procedure is termed multi-look processing. An individual look extraction filter may be written

$$l_i(t) = \exp\left\{-\pi \frac{(t - t_i)^2}{T_l^2}\right\} . \tag{13}$$

Since we are dealing with a large time-bandwidth product signal, windowing in the frequency domain is equivalent to windowing in the time domain. Thus, the effective processing filter may be written

$$h_i(t) = h(t) \cdot l_i(t) \tag{14}$$

for the i^{th} look. This equality only applies prior to application of the processing filter when the time-bandwidth product is large.

Ignoring the receiver noise, the SAR/processor response to the static, impulsive target $f(t) = \sqrt{\sigma}\,\delta(t)$ is

$$g_s(t, t_i) = \sigma \left| w(t) * h_i(t) \right|^2 , \tag{15}$$

where $w(t)$ is defined in equations (5) and (11), and $h_i(t)$ is defined in equations (12), (13), and (14). The scaling constant σ is the power received at the radar which is proportional to the impulsive target's radar cross-section, accounting for geometry effects in microwave propagation and reflection through the radar equation [81]. For convenience, σ is set equal to 1 in the ensuing discussion.

The required convolution is conveniently formed using Fourier transform techniques. The forward transforms of $w(t)$ and $h_i(t)$ take advantage of these signal's large time-bandwidth product and use the principle of stationary phase [19,63]. The transformed functions are then multiplied together and inverse Fourier transformed. For $\eta \ll 1$, we

find that

$$g_s(t,t_i) = \frac{T^2}{\sqrt{K^2+\epsilon^2}} \cdot \exp\left\{-2\pi \frac{L}{K}\frac{t_i^2}{T_l^2}\right\} \cdot \exp\left\{-2\pi \frac{B^2}{K+(\epsilon^2/K)}\left[t+\left(\frac{T}{T_l}\right)^2 \frac{t_i}{K}\eta\right]^2\right\}, \tag{16}$$

where $\epsilon = TB\eta$. The fractional reduction in bandwidth due to the processing filter window is $1/\sqrt{L}$ where $L = 1 + (T/T_p)^2$. The fractional reduction in bandwidth due to the processing filter window and the look extraction window is $1/\sqrt{K}$ where $K = 1 + (T/T_p)^2 + (T/T_l)^2$. This response (and all other generic forms derived) are listed in Table II on page 26.

The term $(T/T_l)^2 t_i/K$ in the second exponentiation of equation (16) is the centre of the effective data window consisting of the pre-filter, processing filter, and offset look-extraction windows. This term interacts with a focus error to govern the relative azimuthal locations of the impulse response associated with each look. That is, the response in the individual looks becomes misregistered in azimuth as well as broadened in response to the focus error. This effect turns out to be of importance in resolving the third key controversial question posed in the Introduction, which is discussed in Chapter 6. The misregistration has a further impact on the resolution after look summation. Some digital SAR processors utilize such azimuthal offsets to estimate the degree of processor focus error. Such a procedure has been termed "autofocus" [39].

The static single-look impulse response has an (equivalent rectangular norm) azimuthal resolution (or time duration) of

$$\rho_{si} = \frac{1}{B}\sqrt{\frac{K}{2}\left[1+\frac{\epsilon^2}{K^2}\right]}. \tag{17}$$

(The azimuthal spatial resolution is $\rho_{si}V$.) This resolution (and all other generic forms derived) are listed in Table III on page 27.

A multi-look (or partially coherent) digital SAR processor is normally implemented as a discrete frequency-plane mixed-integrator; only looks from several discrete-look locations are extracted and summed to produce the final SAR image [9]. The block

diagram for this process is shown in Fig. 3 and may be represented by

$$g_{sm}(t) = \sum_i g_s(t, t_i) \tag{18}$$

where the subscript m signifies multi-look summation.

A partially coherent optical SAR processor can operate as a continuous or scanning frequency-plane mixed integrator in that looks extracted from a continuum of frequency locations are summed to produce the final SAR image [91]. This process may be represented by

$$g_{sm}(t) = \frac{1}{p} \int_{-\infty}^{\infty} g_s(t, t_i)\, dt_i \ , \tag{19}$$

where p is a normalization constant which is equal to the area of the squared look-extraction window. It has been shown that discrete and continuous modes of operation produce substantially equivalent results as far as resolution degradation and speckle smoothing are concerned, although some improvement may be enjoyed by overlapping the looks [91]. Either approach is satisfactory for the work of this research, although closed form expressions are more readily obtained with equation (19).

Consider now the multi-look case. Using equations (16) and (19) with $p = T_l/\sqrt{2}$ we find that the multi-look impulse response is

$$g_{sm}(t) = \frac{T^2}{\sqrt{KL + \epsilon^2}} \cdot \exp\left\{-2\pi \frac{B^2 t^2}{K + \epsilon^2/L}\right\} \ , \tag{20}$$

which has resolution

$$\rho_{sm} = \frac{1}{B}\sqrt{\frac{K}{2}\left[1 + \frac{\epsilon^2}{KL}\right]} \ . \tag{21}$$

Observe that in the event of a focus error the resolution of the multi-look response is degraded more than that of a single look of that same multi-look set. Care is required in using published results on focus sensitivity as the single-look of a multi-look set case or the multi-look case is seldom clearly stated.

The susceptibility of SAR/processor resolution to a focus error may be judged by observing when the focus error term becomes of comparable size to the perfect focus

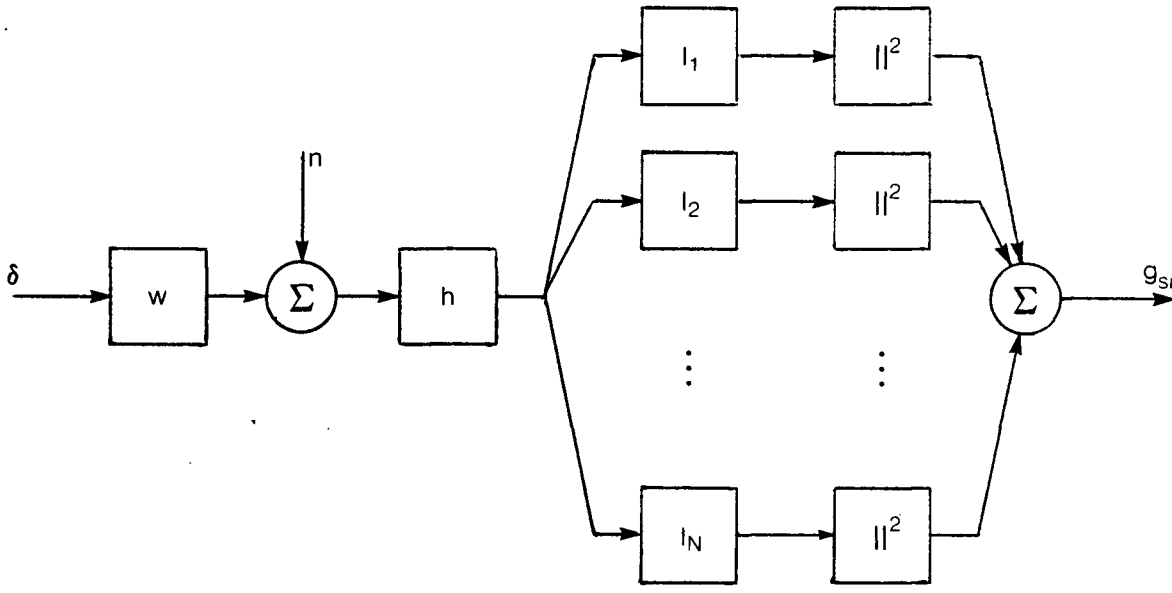

Figure 3: Azimuthal channel block diagram for partially coherent processing.

resolution. For a single-look of a multi-look set, this occurs when

$$|\eta| > \frac{K}{TB} = \frac{2N^2}{TB} \,. \tag{22}$$

For the multi-look case, this occurs when

$$|\eta| > \frac{\sqrt{KL}}{TB} = \frac{2N}{TB} \,. \tag{23}$$

In each case, the second equality applies to matched filter processing. These results demonstrate that a focus error is more limiting in the multi-look case—the normal processor operating configuration. This is largely due to the responses within the individual looks becoming misregistered. An alternative measure of the susceptibility to focus errors is the depth of focus [81], which is the nominal range times the right hand side of the appropriate expression in equation (22) or (23). This represents the error in target range which still allows reasonable focussing properties. For this alternate definition, the same sensitivities result for the single-look versus multi-look cases.

2.1.2 Applications in SAR Ocean Imaging

Two specific processing models are generally found in the SAR ocean literature. The first model is the case of matched filter processing ($T_p = T$) which is what all practical SAR processors attempt to approach. The second model is infinite rectangular filter processing ($T_p \longrightarrow \infty$) which is an unrealizable processing scheme, although somewhat simpler to handle analytically.

It is well known that a single-look of a multi-look set has resolution degraded in proportion to the number of looks extracted N for matched filter processing [19]. Using this result, the derived terms in the impulse response equations developed in this Chapter take the forms shown in Table I in terms of B, T, and N. Note that for matched filter processing ($T_p = T$, $\eta = 0$), we find that $\rho_{sm} = N/B$ and that the peak intensity is $T^2/2N$. These are well known results in SAR analysis.

Table I: Specific forms of the derived variables.
Cases of matched filter processing and infinite rectangular filter processing in terms of the fundamental parameters B, T, and N.

Generic Form	Matched Filter $T_p = T$	Infinite Rectangular $T_p \to \infty$
$K = 1 + \left(\frac{T}{T_p}\right)^2 + \left(\frac{T}{T_l}\right)^2$	$2N^2$	N^2
$L = 1 + \left(\frac{T}{T_p}\right)^2$	2	1
$M = 1 + \left(\frac{T_l}{T_p}\right)^2$	$\frac{2N^2-1}{2(N^2-1)}$	1
ρ_{sm}	$\frac{N}{B}$	$\frac{N}{\sqrt{2}B}$
peak intensity	$\frac{T^2}{2N}$	$\frac{T^2}{N}$

It is helpful to have at hand Table I, since many results available in the literature are based upon one or the other assumptions for the filter weighting, although not always clearly. Since resolution of certain areas of controversy depends upon factors of two, the contents of the Table may be useful.

2.2 Dynamic Point Target

In the event of point target motion, the important target velocity parameters are the radial velocity v (the target velocity component away from the radar along the radial line of sight), the radial acceleration a, and the along-track velocity u [60] as shown in Fig. 4. (If the motion parameters change during observation, the average values should be used. The appropriate average is over the duration of the time domain look-extraction window.) To second order, the moving point target range equation may be written

$$R(t) \approx R_0 + vt + \frac{V^2}{2R_0}\left[1 - \frac{2u}{V} + \frac{R_0 a}{V^2}\right] t^2 \,. \tag{24}$$

The target's dynamic properties may be represented by a multiplicative quadratic

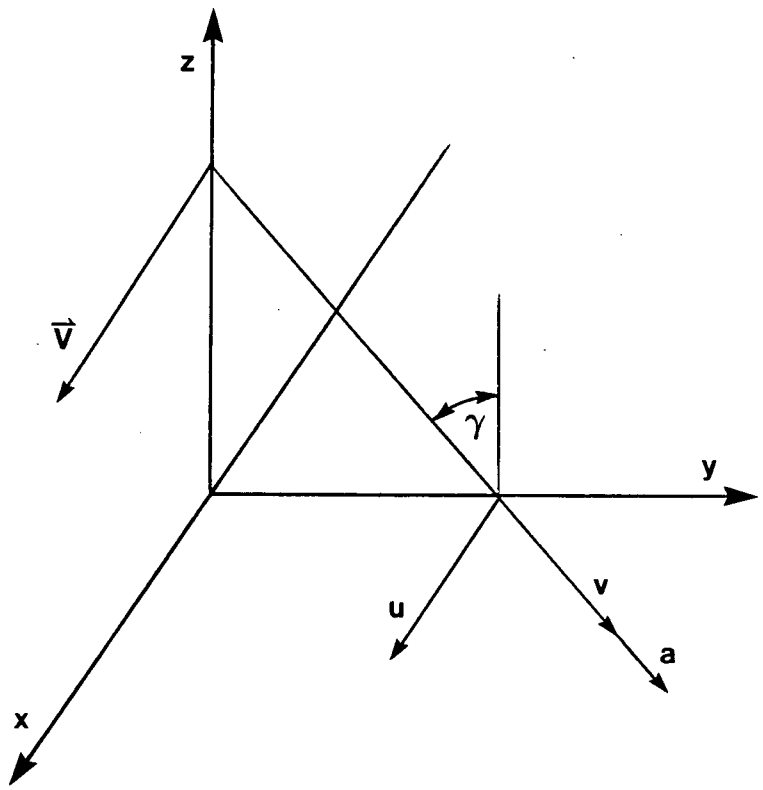

Figure 4: Predominant point target motion parameters

phase term [12,13,51,61,63]. The resulting system block diagram is shown in Fig. 5b in which the multiplicative phase term is

$$\beta(t) = \frac{B}{T}\left[t_D t + \hat{\eta} t^2\right] , \tag{25}$$

where $t_D = R_0 v / V^2$ is proportional to the Doppler shift due to the radial velocity component and where $\hat{\eta} = R_0 a / V^2 - 2u/V$ is the contribution of the target motion to the focus error[6]. We find that the dynamic impulse response of this scene/SAR/processor system is

$$g_d(t, t_i) = \frac{T^2}{\sqrt{K^2 + \epsilon^2}} \cdot \exp\left\{-\frac{2\pi}{K T_l^2}\left[L t_i^2 + 2 t_i t_D + M t_D^2\right]\right\}$$
$$\cdot \exp\left\{-2\pi \frac{B^2}{K + \epsilon^2/K}\left[t + t_D\left(1 - \frac{\delta\eta}{K}\right) + \left(\frac{T}{T_l}\right)^2 \frac{t_i}{K}\delta\eta\right]^2\right\} , \tag{26}$$

where $\delta\eta = \eta - \hat{\eta}$ and now $\epsilon = TB\delta\eta$. The fractional reduction in processor bandwidth due to the look-extraction window is $1/\sqrt{M}$ where $M = 1 + (T_l/T_p)^2$.

The resolution (width of $g_d(t, t_i)$) is

$$\rho_{di} = \frac{1}{B}\sqrt{\frac{K}{2}\left[1 + \frac{\epsilon^2}{K^2}\right]} , \tag{27}$$

the same as equation (17), the result previously derived for the static case. It is possible to compensate for resolution loss due to coherent target motion by matching η, the processor focus parameter, to $\hat{\eta}$ for a given target. This would be at the expense of all other targets not subject to the same motion parameters becoming correspondingly defocussed. Thus, an ensemble of point targets, each with different motion parameters, cannot all be matched simultaneously by the processor. Note also that attempts to

[6]It has become customary in the SAR ocean literature to express the focus error in terms of an equivalent azimuthal velocity u_f. Then, we may write

$$u_f = \frac{V}{2}(\eta - \hat{\eta})$$

expresses the equivalent target velocity necessary to account for the net focus perturbation. This practice has lead to rather misleading interpretations of SAR image phenomena, since it suggests that the targets themselves are moving at such velocities. This is patently not the case from an oceanographic point of view (see Chapter 6).

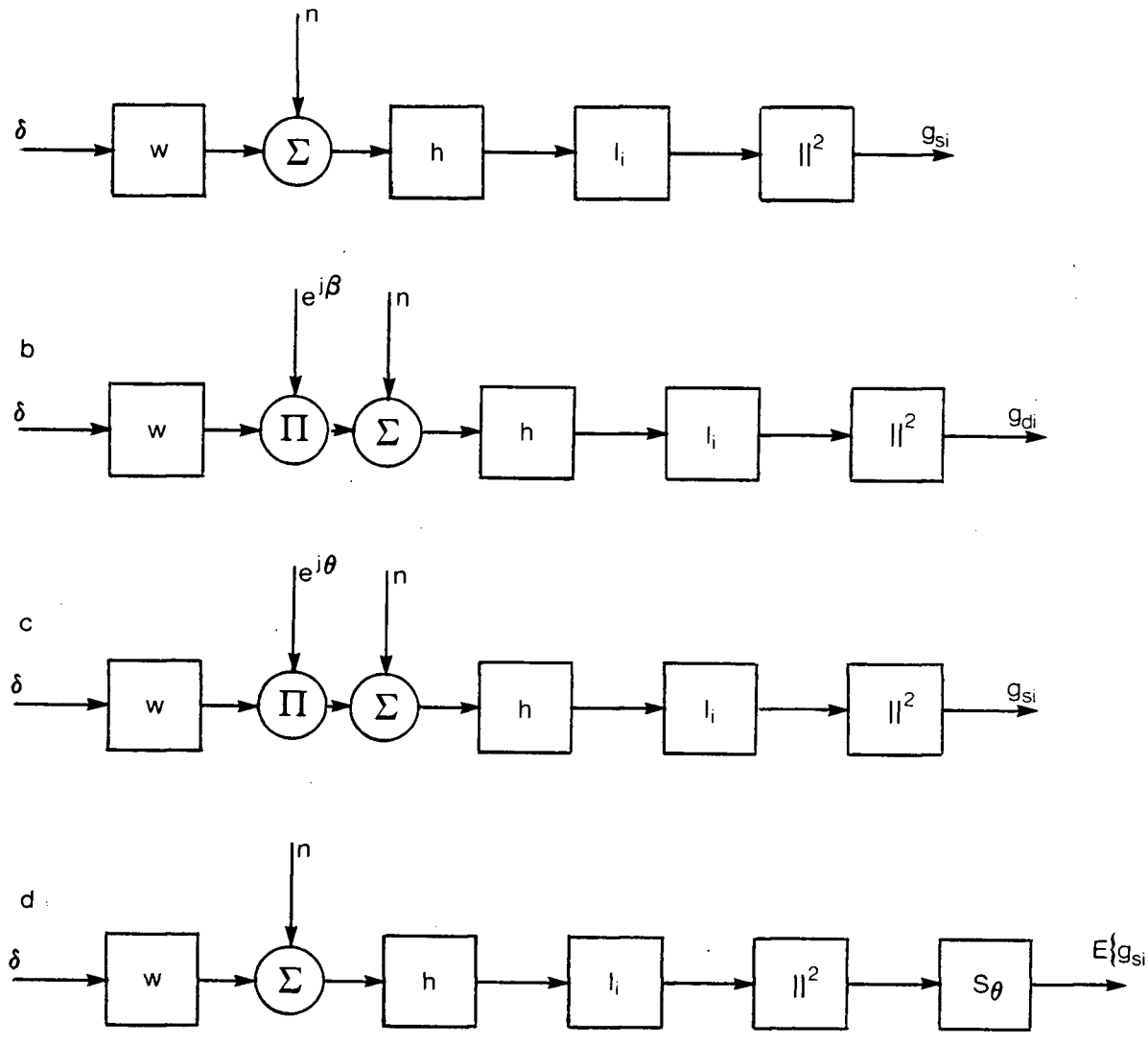

Figure 5: Azimuthal channel block diagrams for single-look of a multi-look set. a) Static point target, b) dynamic point target, c) and d) partially coherent point target. Representations c) and d) are equivalent if $\{\theta\}$ is wide sense stationary in temporal variables.

estimate the focus error of moving targets by comparison of the look offsets produces incorrect results. Likewise, image improvement through focus adjustment ("autofocus") schemes should not be used in conjunction with moving target fields. These points are readdressed in subsequent sections, and cannot be overemphasized given the current state of confusion which is found in the literature [20,25,26,27,50,72,73].

The peak intensity of each look may be severely attenuated by the radial Doppler term t_D if the target Doppler shift is an appreciable fraction of the system Doppler bandwidth. This effect is called Doppler suppression and may be important for an airborne SAR observing the ocean surface. The Doppler suppression may be slightly reduced by increasing the width of the processing filter T_p. However, this is at the expense of an increased signal-to-noise ratio, and could lead to azimuthal ambiguity problems [19].

In the event of multi-look summation, equation (19) gives

$$g_{dm}(t) = \frac{T^2}{\sqrt{KL+\epsilon^2}} \cdot \exp\left\{-2\pi \frac{t_D^2}{LT_p^2}\right\} \cdot \exp\left\{-2\pi \frac{B^2}{K+\epsilon^2/L}\left[t + t_D\left(1-\frac{\delta\eta}{L}\right)\right]^2\right\}, \quad (28)$$

which has resolution

$$\rho_{dm} = \frac{1}{B}\sqrt{\frac{K}{2}\left(1+\frac{\epsilon^2}{KL}\right)}. \quad (29)$$

This resolution is the same as equation (21), the result previously derived for the multi-look static case. The peak of the response is reduced by Doppler suppression (first exponentiation in equation (28)).

The azimuthal location of a given target is governed by the time at which zero Doppler occurs. Thus, the target location is offset in azimuth due to the Doppler frequency shift $f_D = 2v/\lambda$ in accordance with the t_D term in the second exponentiation in equation (28). The spatial offset in response to a radial Doppler shift term (in the absence of focus error) is

$$\Delta x = -V\frac{T}{B}f_D = -Vt_D = -\frac{R_0 v}{V}, \quad (30)$$

which is a well known result. Additional position modulations result from interaction with the focus error terms as indicated in equation (28) and as shown in Fig. 6.

2.3 Partially Coherent Point Target

If target motion is not adequately described by first and second order terms as in equation (24), or the target is subject to a multiplicative complex fading process, an additional phase perturbation parameter $\theta(t)$ should be introduced into the target's phase history (Fig. 5c). Let $\{\theta(t)\}$ be a sample function of a random process, which for convenience may be taken to be zero-mean, wide-sense stationary. This parameter models random phase behaviour for the ensemble of targets which represents a partially coherent scene. The expected scene/SAR/processor impulse response for a single-look may be written

$$E\{g(t,t_i)\} = E\left\{\left|w(t)\cdot\exp[j\theta(t)] * h_i(t)\right|^2\right\} , \tag{31}$$

where $E\{\ \}$ is the ensemble average operator, which is equivalent to a time average for an ergodic wide sense stationary random process. We may write[7]

$$E\{g(t,t_i)\} = \iint w(t_1)\overline{w(t_2)}h_i(t-t_1)\overline{h_i(t-t_2)}R_\theta(t_2-t_1)\,dt_1\,dt_2 , \tag{32}$$

where

$$R_\theta(\tau) = E\left\{\exp[j\theta(t)]\overline{\exp[-j\theta(t+\tau)]}\right\} \tag{33}$$

is the autocorrelation function of $\exp[j\theta(t)]$. Then, we find that

$$E\{g(t,t_i)\} = \int_{-\infty}^{\infty} \left|w(t)\exp[j2\pi\nu t] * h_i(t)\right|^2 S_\theta(\nu)\,d\nu , \tag{34}$$

[7]If the look-extraction windows are explicitly included at this stage, the order of summation and integration may be exchanged to give

$$E\{g(t)\} = \iint w(t_1)\overline{w(t_2)}h(t-t_1)\overline{h(t-t_2)}R_\theta(t_2-t_1)l(t_2-t_1)\,dt_1\,dt_2$$

where

$$l(t_2-t_1) = \sum_i l_i(t-t_1)\overline{l_i(t-t_2)}$$

is a correlation function. This relates the development considered here to the quadratic filter theory formulation [61,63,64]. Unfortunately, the elegant quadratic filter formulation imposes increased mathematical complexity upon some of the issues considered in this work, and does not allow explicit exposure of certain parameter dependencies that are of central interest.

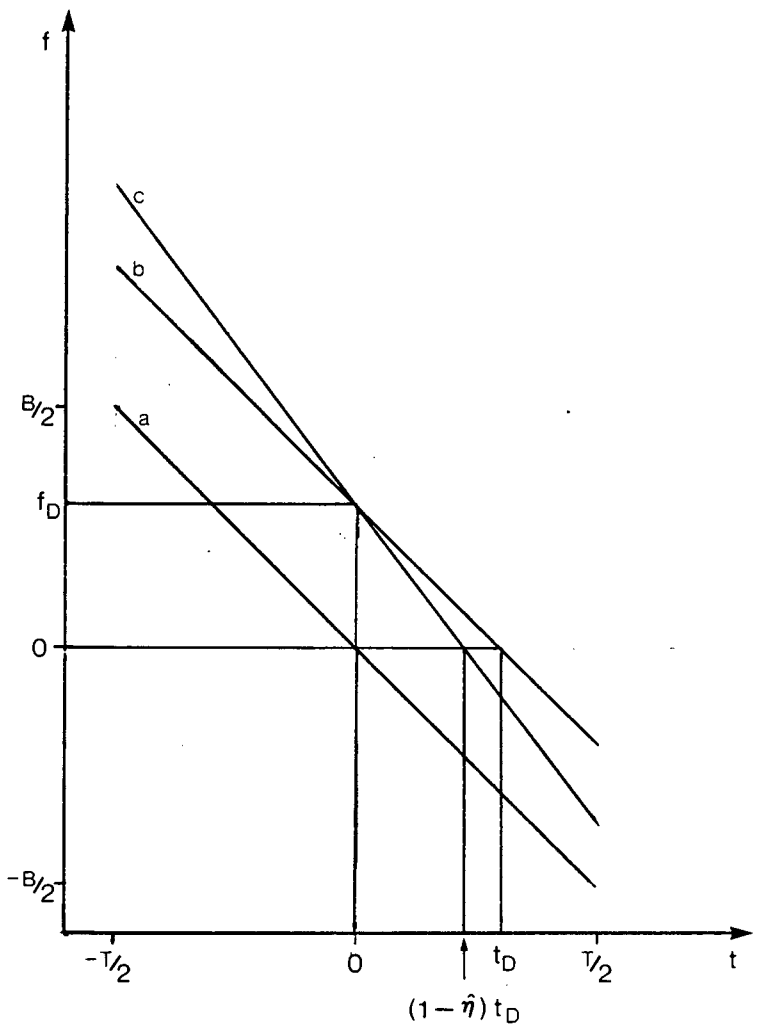

Figure 6: Point target Doppler history.
The time of zero Doppler, hence the target location, is governed by the Doppler shift $f_D = 2v/\lambda$ and the target motion induced focus error $\hat{\eta}$. Three cases are represented: a) $f_D = 0$, $\hat{\eta} = 0$; b) $f_D > 0$, $\hat{\eta} = 0$; and c) $f_D > 0$, $\hat{\eta} > 0$.

where $S_\theta(f)$, the power spectrum of the random process $\exp[j\theta(t)]$, is the Fourier transform of $R_\theta(\tau)$. The expected impulse response may be written

$$E\{g(t,t_i)\} = \int_{-\infty}^{\infty} |\chi_{wh}(t,\nu)|^2 \, S_\theta(\nu)\, d\nu \,, \tag{35}$$

where $\chi_{wh}(f,\nu)$ is the (non-normalized) cross-ambiguity function [70,88] for the SAR azimuthal channel. Thus, for a static target we may write

$$E\{g_s(t,t_i)\} = \int_{-\infty}^{\infty} g_d(t,t_i)\Big|_{t_D=T\nu/B,\hat{\eta}=0} S_\theta(\nu)\, d\nu \,, \tag{36}$$

and for a dynamic target

$$E\{g_d(t,t_i)\} = \int_{-\infty}^{\infty} g_d(t,t_i)\Big|_{t_D\to t_D+T\nu/B} S_\theta(\nu)\, d\nu \,. \tag{37}$$

It is convenient (and adequate for present purposes) to assume a normal correlation function for the random process $\exp[j\theta(t)]$. Then, we may write

$$R_\theta(\tau) = \exp\left\{-\pi\frac{\tau^2}{\tau_c^2}\right\} \,, \tag{38}$$

where τ_c is the coherence time scale. This time may be defined on the basis of the target's rms velocity as

$$\tau_c = \frac{\lambda}{2v_{\rm rms}} \,. \tag{39}$$

This formulation will be examined in greater detail in subsequent sections.

The dynamic single-look impulse response in the face of a finite scene coherence time under the above assumptions is

$$E\{g_d(t,t_i)\} = \frac{T^2}{\sqrt{PK + P\epsilon^2/K + 2(T/\tau_c)^2}} \cdot \exp\left\{-\frac{2\pi}{KT_l^2}\left[LQt_i^2 + 2Rt_it_D + MRt_D^2\right]\right\}$$

$$\cdot \exp\left\{-2\pi\frac{B^2}{K + \epsilon^2/K + (2/P)(T/\tau_c)^2}\right.$$

$$\left.\left[t + \left(1 - \frac{\delta\eta}{K}\right)Rt_D + \left(\delta\eta - \frac{2(1-\delta\eta)/K}{P(\tau_cB)^2}\right)\left(\frac{T}{T_l}\right)^2\frac{t_i}{K}\right]^2\right\} \,, \tag{40}$$

where

$$P = 1 + \frac{2M}{K}\left(\frac{T}{T_l}\right)^2 \frac{1}{(\tau_c B)^2}\,, \tag{41}$$

$$Q = 1 - \frac{2}{KLP}\left(\frac{T}{T_l}\right)^2 \frac{1}{(\tau_c B)^2}\,, \tag{42}$$

$$R = 1 - \frac{2M}{KP}\left(\frac{T}{T_l}\right)^2 \frac{1}{(\tau_c B)^2}\,, \tag{43}$$

and the resolution is

$$\rho_i = \frac{1}{B}\sqrt{\frac{K}{2}\left[1 + \frac{\epsilon^2}{K^2} + \frac{2}{KP}\left(\frac{T}{\tau_c}\right)^2\right]}\,. \tag{44}$$

We now introduce a new measure of fine-scale scene dynamics which is the concept of a coherence time-bandwidth product $\tau_c B$. The magnitude of this product seems to differentiate between two distinct asymptotic operating regimes. If

$$\tau_c B \gg 1\,, \tag{45}$$

we are in either a fully or partially coherent regime. In this case $P, Q, R = 1$, and if $t_D = 0$ we get the simplified and important result [61,63]

$$E\{g(t,t_i)\} = g(t,t_i) * \frac{B}{T} S_\theta\left(\frac{B}{T}t\right)\,. \tag{46}$$

In this case, the mean effects of a finite scene coherence time may be represented by a low-pass filter applied after detection. This case is shown in Fig. 5d. Thus, Fig. 5c and Fig. 5d are equivalent representations if inequality (45) is satisfied.

Equation (46) directly applies to the expected response of an isolated point target only. In this case, the expected single-look static impulse response is

$$E\{g_s(t,t_i)\} = \frac{T^2}{\sqrt{K^2 + \epsilon^2 + (2/K)(T/\tau_c)^2}} \cdot \exp\left\{-2\pi \frac{L t_i^2}{K T_l^2}\right\}$$

$$\cdot \exp\left\{-2\pi \frac{B^2}{K + \epsilon^2/K + 2(T/\tau_c)^2}\left[t + \left(\frac{T}{T_l}\right)^2 \frac{t_i}{K}\eta\right]^2\right\} \tag{47}$$

which has resolution

$$\rho_i = \frac{1}{B}\sqrt{\frac{K}{2}\left[1 + \frac{\epsilon^2}{K^2} + \frac{2}{K}\left(\frac{T}{\tau_c}\right)^2\right]}\,. \tag{48}$$

After multi-look summation, the impulse response becomes

$$E\{g_{sm}(t)\} = \frac{T^2}{\sqrt{KL + \epsilon^2 + (2/K)(T/\tau_c)^2}} \cdot \exp\left\{-2\pi \frac{B^2 t^2}{K + \epsilon^2/L + 2(T/\tau_c)^2}\right\} , \quad (49)$$

which has resolution

$$\rho_m = \frac{1}{B}\sqrt{\frac{K}{2}\left[1 + \frac{\epsilon^2}{KL} + \frac{2}{K}\left(\frac{T}{\tau_c}\right)^2\right]} . \quad (50)$$

These results become identical to those of the static impulse response in the limit of $T/\tau_c \longrightarrow 0$.

The condition of equation (45) is likely well satisfied for all satellite SAR platforms. In this case, B is $O(10^3)$ Hz so that even a coherence time of 10 msec satisfies the condition. However, in the case of an airborne SAR platform, B may be as small as $O(50)$ Hz, and equation (45) may not hold. Then, the impulse response described by equation (46) is not valid. Thus, other operating regimes should be considered.

A second asymptotic operating regime is one which is characterized by

$$\tau_c B \ll 1 . \quad (51)$$

This represents the noncoherent limit. In this case, a SAR is expected to approach the behaviour of a real aperture radar. The expected single-look impulse response is

$$E\{g(t,t_i)\} = \frac{T\tau_c}{\sqrt{2K}} \cdot \exp\left\{-2\pi \frac{t_i^2}{MT_p^2}\right\} \cdot \exp\left\{-2\pi \frac{M}{KT_l^2}\left[t + \frac{\delta\eta - 1}{M} t_i\right]^2\right\} , \quad (52)$$

which has resolution

$$\rho_i = T_l\sqrt{\frac{K}{2M}} . \quad (53)$$

After multi-look summation, we find that

$$E\{g_m(t)\} = \frac{T\tau_c}{\sqrt{2L}} \cdot \exp\left\{-2\pi \frac{Lt^2}{T_p^2}\right\} , \quad (54)$$

which has resolution

$$\rho_m = T_p\sqrt{\frac{L}{2}} . \quad (55)$$

As the target coherence time decreases, the resolution becomes limited by the breadth of either the processing or look-extraction window. Although not of direct relevance to this work, these results illustrate some of the subtleties in passing continuously from a coherent or partially coherent limit to a noncoherent limit [18]. Note that $\rho_m \longrightarrow \infty$ for infinite rectangular filter processing.

The level of coherence being governed by the coherence time-bandwidth product is rather surprising. In fact, it might be expected that the coherence should be governed by the portion of the bandwidth relevant to the coherence time (*i.e.* $K_a\tau_c$), in analogy to the case of a focus error. However, for both the single-look of a multi-look set case and the multi-look case, the impact upon the resolution by the coherence time term is the same and depends upon the entire available coherent integration time T. This is in contrast to the case of a focus error for which the resolution degradation due to the focus error depends upon the specific processing scheme. Thus, the coherence time-bandwidth product is a measure of the degree of coherent, or of multi-look processing, which the signal will support. This restraint is a new result.

2.4 Summary

This Chapter has presented reasonably simple, closed-form expressions for the scene/SAR/processor impulse response. The calculations were based upon generic Gaussian weighting functions and considered the effects of target motion, target partial coherence, and various processor configurations. It was suggested that the scene coherence time-bandwidth product represents a measure of the degree of coherent processing which the received signal from a given point target will support. The general operating regime is either fully or partially coherent. The derivations of this Chapter are summarized in Table II for the impulse responses, and in Table III for the corresponding resolution measures.

Table II: Summary of generic impulse response forms.
Single-look of a multi-look set and multi-look processing for the cases of static, dynamic, and partially coherent targets are included.

STATIC POINT TARGET	
single-look of a multi-look set	$g_s(t,t_i) = \frac{T^2}{\sqrt{K^2+\epsilon^2}} \cdot \exp\left\{-2\pi \frac{L}{K}\frac{t_i^2}{T_i^2}\right\} \cdot \exp\left\{-2\pi \frac{B^2}{K+(\epsilon^2/K)}\left[t+\left(\frac{T}{T_l}\right)^2 \frac{t_i}{K}\eta\right]^2\right\}$ (16)
multi-look	$g_{sm}(t) = \frac{T^2}{\sqrt{KL+\epsilon^2}} \cdot \exp\left\{-2\pi \frac{B^2 t^2}{K+\epsilon^2/L}\right\}$ (20)
DYNAMIC POINT TARGET	
single-look of a multi-look set	$g_d(t,t_i) = \frac{T^2}{\sqrt{K^2+\epsilon^2}} \cdot \exp\left\{-\frac{2\pi}{KT_i^2}\left[Lt_i^2 + 2t_i t_D + Mt_D^2\right]\right\}$ $\cdot \exp\left\{-2\pi \frac{B^2}{K+\epsilon^2/K}\left[t+t_D\left(1-\frac{\delta\eta}{K}\right)+\left(\frac{T}{T_l}\right)^2\frac{t_i}{K}\delta\eta\right]^2\right\}$ (26)
multi-look	$g_{dm}(t) = \frac{T^2}{\sqrt{KL+\epsilon^2}} \cdot \exp\left\{-2\pi \frac{t_D^2}{LT_p^2}\right\} \cdot \exp\left\{-2\pi \frac{B^2}{K+\epsilon^2/L}\left[t+t_D\left(1-\frac{\delta\eta}{L}\right)\right]^2\right\}$ (28)
PARTIALLY COHERENT POINT TARGET	
single-look of a multi-look set	$E\{g_s(t,t_i)\} = \frac{T^2}{\sqrt{K^2+\epsilon^2+(2/K)(T/\tau_c)^2}} \cdot \exp\left\{-2\pi \frac{Lt_i^2}{KT_i^2}\right\}$ $\cdot \exp\left\{-2\pi \frac{B^2}{K+\epsilon^2/K+2(T/\tau_c)^2}\left[t+\left(\frac{T}{T_l}\right)^2\frac{t_i}{K}\eta\right]^2\right\}$ (47)
multi-look	$E\{g_{sm}(t)\} = \frac{T^2}{\sqrt{KL+\epsilon^2+(2/K)(T/\tau_c)^2}} \cdot \exp\left\{-2\pi \frac{B^2 t^2}{K+\epsilon^2/L+2(T/\tau_c)^2}\right\}$ (49)

$$
\begin{aligned}
K &= 1+\left(\frac{T}{T_p}\right)^2+\left(\frac{T}{T_l}\right)^2 \\
L &= 1+\left(\frac{T}{T_p}\right)^2 \\
M &= 1+\left(\frac{T_l}{T_p}\right)^2 \\
T &= \frac{R_0\beta}{V} \quad \text{(sec)} \\
B &= \frac{2V\beta}{\lambda} \quad \text{(Hz)} \\
\epsilon &= TB\delta\eta
\end{aligned}
$$

Table III: Summary of derived SAR temporal resolutions.
The generic resolution and resolution for the case of matched filter processing are included.

	single-look of multi-look set	multi-look
static or dynamic	$\rho_i = \frac{1}{B}\sqrt{\frac{K}{2}\left[1+\frac{\epsilon^2}{K^2}\right]}$ (17),(27) $\rho_i = \frac{N}{B}\sqrt{1+\frac{\epsilon^2}{4N^4}}$	$\rho_m = \frac{1}{B}\sqrt{\frac{K}{2}\left[1+\frac{\epsilon^2}{KL}\right]}$ (21),(29) $\rho_m = \frac{N}{B}\sqrt{1+\frac{\epsilon^2}{4N^2}}$
partially coherent	$\rho_i = \frac{1}{B}\sqrt{\frac{K}{2}\left[1+\frac{\epsilon^2}{K^2}+\frac{2}{K}\left(\frac{T}{\tau_c}\right)^2\right]}$ (48) $\rho_i = \frac{N}{B}\sqrt{1+\frac{\epsilon^2}{4N^4}+\frac{1}{N^2}\left(\frac{T}{\tau_c}\right)^2}$	$\rho_m = \frac{1}{B}\sqrt{\frac{K}{2}\left[1+\frac{\epsilon^2}{KL}+\frac{2}{K}\left(\frac{T}{\tau_c}\right)^2\right]}$ (50) $\rho_m = \frac{N}{B}\sqrt{1+\frac{\epsilon^2}{4N^2}+\frac{1}{N^2}\left(\frac{T}{\tau_c}\right)^2}$

$$
\begin{aligned}
K &= 1+\left(\frac{T}{T_p}\right)^2+\left(\frac{T}{T_l}\right)^2 \\
L &= 1+\left(\frac{T}{T_p}\right)^2 \\
T &= \frac{R_0\beta}{V} \quad \text{(sec)} \\
B &= \frac{2V\beta}{\lambda} \quad \text{(Hz)} \\
\epsilon &= TB\delta\eta
\end{aligned}
$$

3 SAR Diffuse Target Imaging

Abstract

This Chapter discusses SAR imagery of diffuse targets. A diffuse target consists of many point targets per resolution element, and leads to the granular speckle image pattern associated with coherent systems. The second order image statistics of such patterns are calculated. It is shown that image resolution may be traded directly for radiometric fidelity, and that the speckle covariance function is of the same width as the static impulse response. Key issues are summarized which may be used to distinguish imagery of point targets from imagery of diffuse targets. These issues are the correlation between looks, peak-height scaling in response to multi-look processing, and the response of the image spectral width to a processor focus error. This Chapter ties the little known diffuse target analysis into the point target analysis framework developed in Chapter 2.

A diffuse target represents the extreme case of many independent point targets per resolution cell. The SAR response to such a target is distinctly different from the case of the isolated point target which was treated in the previous Chapter. Here, we examine the SAR response to a diffuse target through the second order image statistics, and then, contrast the results with those of the isolated point target case.

3.1 Second Order Image Statistics

A diffuse scene may be regarded as being composed of an ensemble of point targets, each characterized by a (statistically independent) radar cross-section and intrinsic phase [69,71]. Then, for each resolution element, the received complex amplitude is the vector summation of the contributions from each point target. If the number of point targets per resolution element is large (a classical guideline is > 5 [34]), the statistically independent intrinsic phases lead to a two-dimensional random walk and Rayleigh statistics for each image element [71]. The resulting grainy multiplicative noise, known as speckle, is characteristic of all coherent imaging systems.

3.1.1 Static Diffuse Target

Consider the case of infinitely many independent, static, point targets per resolution element. For such a diffuse scene, the input to the azimuthal channel may be modelled

as

$$f(t) = a(t) + jb(t) \,, \tag{56}$$

where $a(t)$ and $b(t)$ are real, zero-mean, statistically independent, Gaussian random variables with identical variances. If $f(t)$ is input to a magnitude squared detector, that is

$$g(t) = |f(t)|^2 \,, \tag{57}$$

then the second-order statistics of the output are [52]

$$R_g(\tau) = 4R^2(0) + 4R^2(\tau) \tag{58}$$

and

$$S_g(f) = 4R^2(0)\delta(f) + 4S(f) * S(f) \,, \tag{59}$$

where

$$R(\tau) = E\{a(t)a(t+\tau)\} = E\{b(t)b(t+\tau)\} = N_0\delta(\tau) \tag{60}$$

and

$$S(f) = N_0 \,. \tag{61}$$

In a SAR system, the input $f(t)$ passes through the linear filters $w(t)$ and $h_i(t)$ prior to the detector. The input spectrum to the detector is modified to

$$S_i(f) = |W(f)H_i(f)|^2 \, S(f) \,, \tag{62}$$

where the subscript i refers to the i^{th} look-extraction filter. Equation (62) may be substituted directly into equations (58) and (59) to give the image spectrum as

$$S_g(f) = 4\left[N_0 \int |W(f)H_i(f)|^2 \, df\right]^2 + 4N_0^2 \, |W(f)H_i(f)|^2 * |W(f)H_i(f)|^2 \,. \tag{63}$$

A norm for radar image radiometric resolution, the expected variation of the radar cross-section for each pixel, is the mean-squared-to-variance ratio (MSVR). Noting that the mean and variance add linearly after look summation, we find that

$$\text{MSVR} = \frac{\left[\iint |W(f)H_i(f)|^2 \, df \, dt_i\right]^2}{\iiint |W(\lambda)H_i(\lambda)|^2 \, |W(f-\lambda)H_i(f-\lambda)|^2 \, df \, d\lambda \, dt_i} \,. \tag{64}$$

Substituting the generic forms for $W(f)$ and $H_i(f)$ of Chapter 2 gives

$$\text{MSVR} = \sqrt{\frac{2K}{L}} = \sqrt{2}N \ , \tag{65}$$

where the second equality applies to matched filter processing[8]. The proportionality to N, the number of looks processed, is a well known result [10,58] and indicates that resolution may be traded directly for radiometric fidelity through the ensemble averaging process of multi-look addition. This is possible since there is very little correlation between the speckle patterns in looks derived from non-overlapping portions of the Doppler spectrum. As the number of independent looks increases, the radiometric fluctuations decrease in proportion to $1/\sqrt{N}$. (The factor of $\sqrt{2}$ in equation (65) arises because the scanning frequency-plane mixed integrator has an infinite scanning bandwidth, and yields some modest improvement over the discrete mixed integrator [91].)

Note that radiometric fidelity is not impaired by multiplicative phase errors since the input signal phase is already a wide bandwidth random process. In other words, scene partial coherence cannot add more independence from look-to-look [64,65].

The azimuthal image spectrum for the diffuse input of equation (56), ignoring a real proportionality constant and a delta function at the origin, is

$$S_{gd}(f) \propto \exp\left\{-\pi\frac{Kf^2}{B^2}\right\} = \exp\left\{-2\pi\frac{N^2f^2}{B^2}\right\} \ , \tag{66}$$

where the equality applies to matched filter processing. This image spectrum has (equivalent rectangular width norm) bandwidth

$$W_d = \frac{B}{\sqrt{K}} = \frac{B}{\sqrt{2}N} \ , \tag{67}$$

where the second equality applies to matched filter processing. An important consequence is that the image bandwidth of a diffuse scene is independent of the processor focus setting. This result may be contrasted with the azimuthal spectral response to the

[8]This is the SAR version of a classic result, known since the 19$^{\text{th}}$ century [69].

image of a static point target (see Table II). Ignoring a real proportionality constant, the azimuthal image spectrum of an isolated, static point target is

$$S_{gp}(f) \propto \exp\left\{-\pi \frac{K}{B^2}\left(1+\frac{\epsilon^2}{K^2}\right) f^2\right\}$$

$$= \exp\left\{-2\pi \frac{N^2}{B^2}\left(1+\frac{\epsilon^2}{N^2}\right) f^2\right\}, \tag{68}$$

where the equality applies to matched filter processing. This spectrum has bandwidth

$$W_p = \frac{W_d}{\sqrt{1+(\epsilon/K)^2}} = \frac{W_d}{\sqrt{1+(\epsilon/2N^2)^2}}, \tag{69}$$

where the second equality again applies to matched filter processing. In contrast to the diffuse case, the bandwidth measure for the point target is dependent upon the processor focus setting. We see also that the speckle covariance function is of the same shape as the zero-focus-error, squared impulse response[9]. This result is used in correcting for the system transfer function in ocean wave spectra derived from SAR imagery [5] as discussed in Appendix E.

3.1.2 Dynamic Diffuse Target

In the event of a dynamic diffuse target, the situation becomes somewhat more complicated [23,61,63]. Each point target which constitutes the scene could be subject to different sets of motion parameters, resulting in each target having a different impulse response. The Doppler shift term t_D causes each target to be shifted differentially in azimuth (and possibly leads to differing Doppler suppression for each such target). If the scene dynamics are random, the target redistribution is also random, and the resulting image will be indistinguishable from the case of a static diffuse target. However, if the scene dynamics are well structured, as can be the case for the ocean surface, otherwise uniformly distributed targets may have their images clustered producing a

[9]This assertion applies to the restraint of Gaussian weighting functions. An upper bound width equivalence applies more generally [63].

nonuniform contrast in the SAR image [37]. This effect is termed velocity bunching and is an important mechanism for SAR imaging of the ocean surface (see Chapter 5).

The scene-induced focus error $\hat{\eta}$ causes the impulse response associated with each target to be broadened independently of the response of the other targets.

3.2 Point vs. Diffuse Scattering

It is useful to be able to differentiate between cases of point and diffuse targets in SAR imagery. As has been previously observed [19,63,81], three fundamental distinctions between SAR imagery of point and diffuse targets are apparent. It has been proposed [64] that these distinctions may be used to test control scenes derived from a given SAR and processor which include known examples of point and diffuse targets. These results may be applied to a test scene to establish the nature of the targets present.

The first fundamental distinction is the correlation between looks in a multi-look set. For an isolated point target, the correlation between looks is large, particularly in the event of no processor focus error. As a focus error is introduced, the peak of the correlation function will remain large, but the responses in the individual looks will become misregistered. This fact is used in the auto-focus technique. For a diffuse target, however, the correlation between looks derived from nominally non-overlapping portions of the Doppler spectrum will be low. It is this property which allows improvement in radiometric resolution through multi-look processing.

The second distinction is the peak scaling in the face of multi-look processing. From Table I on page 14, the peak intensity scales as $1/N$ for point targets. If the processor is a discrete frequency-plane mixed-integrator, a large focus error could misregister the looks enough to cause this property to break down. The standard deviation of a diffuse scene is a measure of the peak heights, and in equation (65) this scaling is shown to be $1/\sqrt{N}$.

Table IV: Behaviour of key image properties for point versus diffuse targets.

property	point	diffuse
correlation between looks	high	low
Peak intensity dependence on N	$\frac{1}{N}$	$\frac{1}{\sqrt{N}}$
focus sensitivity	yes	no
azimuthal spectral width a measure of:	$(\text{resolution})^{-1}$	bandwidth

The third key difference is the response to a focus error. This response may be judged by measuring the image bandwidth. We have seen in equation (67) that in the event of a diffuse scene, the bandwidth will not respond to a processor focus perturbation. However, as shown in equation (69), the impulse response will broaden and the bandwidth will decrease as the processor focus error increases.

These contrasting image properties are summarized in Table IV and are used as a basis for a statistical testing methodology which is found in Chapter 7, and is intended to address the issue of point versus diffuse scattering in SAR ocean surface imaging.

Appropriate and tractable statistical description is awkward for the cases in which the average number of scatterers per resolution element is neither very small (purely isolated point targets) nor very large (purely diffuse target). A modified Bessel-function distribution has been proposed for such cases [29,30] and has been proven successful in describing many natural phenomena [32] including non-Rayleigh radar returns [31]. Unfortunately, a physical basis has not been found for the applicability of these K-distributions[10].

[10]The problem of detecting a specular scatterer in clutter is representative of the difficulties encountered [75,76], although this problem does not directly apply here.

3.3 Summary

This Chapter has cast the imaging of diffuse targets into the framework presented in Chapter 2. The response to a diffuse target is formulated in terms of the second order image statistics. These results are contrasted with those of an isolated point target. The key areas of departure, outlined in Table IV, are the inter-look cross-correlation, the peak-height scaling in response to multi-look processing, and the focus sensitivity which is manifested in the image spectral bandwidth.

4 Ocean Surface Waves

Abstract

This Chapter presents a succinct review of ocean surface waves which is based upon currently accepted oceanographic theory. The content is neither new nor controversial. However, many of the concepts presented become misconstrued when interpreted within the framework of SAR ocean surface imaging. Inclusion in this thesis is essential for an interdisciplinary understanding of the issues involved.

The behaviour, analysis, and observation of ocean surface waves are well developed subjects which can be found in many introductory level [57] and advanced level oceanographic text books [36,38,48,53]. The content of this Chapter is drawn primarily from such sources.

4.1 Subject Overview

We begin by considering the ocean surface displacement in response to the monochromatic sinusoidal ocean surface wave given by

$$\varsigma(x,t) = A\cos(Kx - \Omega t)\,, \tag{70}$$

where A is the wave amplitude, K is the wavenumber, and Ω is the wave frequency. This formulation represents a travelling train of waves of infinite extent with wavelength $\Lambda = 2\pi/K$ and period $T_w = 2\pi/\Omega$. A point of constant phase on the surface of the wave advances with a speed given by the magnitude of the phase velocity, which is

$$C_p = \frac{\Omega}{K}\,. \tag{71}$$

The phase velocity is in the direction of wave propagation.

An important characteristic of ocean surface waves is their dispersive nature. The dispersion relation, based upon a linearized analysis, is given by

$$\Omega^2 = \left(gK + \frac{\sigma K^3}{\rho}\right)\tanh(Kh)\,, \tag{72}$$

where h is the water depth, σ is the surface tension (~ 0.074 N/m), and ρ is the water density ($\sim 1000\text{kg/m}^3$). This result is independent of the wave amplitude, and holds if $A \ll \Lambda$.

In the open ocean, surface gravity waves often satisfy $h \gg \Lambda$. Then, $Kh \gg 1$ and the $\tanh(Kh)$ term approaches unity. This is the deep water or short wave limit.

The role of surface tension as a restoring force is quantified by the $\sigma K^3/\rho$ term in the dispersion relation, while the role of gravity as a restoring force is quantified by the gK term. The importance of these two terms may be judged by their ratio. This number, called the Weber number, is given by

$$W = \frac{\sigma K^2}{g\rho} . \tag{73}$$

The critical value occurs when the two restoring forces are of equal importance, in which case $W = 1$. For typical oceanic conditions this occurs for $\Lambda = 1.73$ cm. If $\Lambda \ll 1.73$ cm, surface tension dominates as the restoring force. Such waves are called capillary waves. If $\Lambda \gg 1.73$ cm, gravity dominates as the restoring force. Such waves are called surface gravity waves. For surface gravity waves

$$C_p = \sqrt{\frac{g}{K}} = 1.25\sqrt{\Lambda} , \tag{74}$$

illustrating that the longer waves will travel the fastest.

As surface gravity waves propagate away from their point of origin, the various wave components separate from each other, with the longer waves moving in advance of the shorter waves. The wave field, at any time and some distance away from the generation area, becomes more purely of one wavenumber, assuming there are no locally generated waves. Such wave systems are called swell and form the basis of assumptions for SAR ocean observation. In contrast, the relatively confused seastates found at the areas of generation are often called wind- waves.

It is well known that microwave scattering from rough surfaces, such as the ocean surface, is dominated by the scattering surface Fourier component whose wavenumber is given by [89,90]

$$K_B = 2k \sin\gamma , \tag{75}$$

where k is the radar wavenumber and γ is the angle of incidence (measured from vertical). This scattering mechanism is called Bragg scattering. The first-order Bragg wavelength is equal to the radar half-wavelength projected onto the ocean surface. For C-band and L-band radars, this wavelength falls into the short gravity wave regime, being typically 6 cm and 30 cm respectively. Thus, a microwave ocean imaging system, such as a SAR, images ocean surface features indirectly; the ocean is seen via Bragg scattering from short gravity waves which are subject to modulations by the longer scale waves (and features) which appear in the SAR imagery. The modulations include velocity changes, straining, and tilting.

There is an important distinction between the velocity of a point of constant phase on the wave surface and the velocity of a packet of water on the ocean surface. While the wave surface advances at the phase speed C_p in the direction of propagation, a packet of water at the ocean surface will be comparatively stationary, yet subject to vertical and horizontal oscillatory velocity components given by

$$u(x,t) = \Omega A \cos(Kx - \Omega t) \,, \tag{76}$$

and

$$w(x,t) = \Omega A \sin(Kx - \Omega t) \tag{77}$$

in deep water. It is apparent that each such water packet is confined to a local domain and describes a circle rather than translating at a large constant rate such as the wave phase velocity. Thus, as a wave passes by a given point on the ocean surface advancing with phase speed C_p, the ocean surface heaves up-and-down and laterally, causing the individual particles on the surface to describe a circle. This orbital motion is illustrated in Fig. 7. Any short waves riding upon the long waves will have their velocities modulated by the orbital velocity rather than the phase velocity.

The straining of short gravity waves riding upon long gravity waves is formulated by appealing to conservation of wave action density and using a WKB-type of perturbation

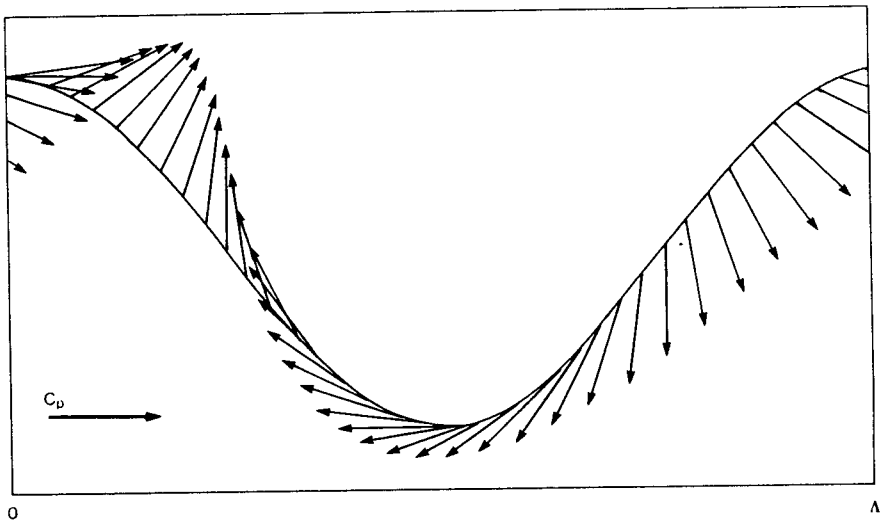

Figure 7: The orbital velocities of points along an ocean wave.

approximation (so that the deep water dispersion relation applies locally to the short waves) [16,53,54]. The effect may be formulated as arising from the currents set up on the ocean surface due to the passage of the wave. As shown by Fig. 7, there is an area of convergence along the wave's leading face, and an area of divergence along the wave's trailing face. It has been proven that the short waves are shortest near the long wave crests and longest near the long wave troughs, that the short waves tend to align with the direction of long wave propagation near the long crests, and that the short waves become higher and steeper near the long wave crests. Thus, the wave crests will be rough relative to the wave troughs, and the small scale structure is dependent upon the large scale wave position.

A sinusoidal ocean wave description can be quite inadequate. Instead, the ocean surface is often described in terms of its one-dimensional frequency spectrum $S_\zeta(\Omega)$. This spectrum is defined by

$$\int_0^\infty S_\zeta(\Omega)\, d\Omega = \langle \zeta^2 \rangle = \frac{A^2}{2}\,, \tag{78}$$

where the second equality applies to the sinusoidal case discussed above. The significant waveheight is defined by

$$H_s = 4\sqrt{\langle \zeta^2 \rangle} = 2\sqrt{2}A\,. \tag{79}$$

Useful generic forms for S_ζ are available [22,55]. The Pierson-Moskowitz wind-wave spectrum is given by

$$S_\zeta(\Omega) = \left(\frac{\alpha g^2}{\Omega^5}\right) \cdot \exp\left\{-\beta \left(\frac{g}{U\Omega}\right)^4\right\}\,, \tag{80}$$

where $\alpha = 0.0081$ and $\beta = 0.74$ are dimensionless empirical constants, and U is the windspeed at 19.5 m above the surface. The windspeed is related to the significant waveheight (in MKS units) via

$$H_s = 2.12(10)^{-2}U^2 \tag{81}$$

in the Pierson-Moskowitz model. This spectral form does not include fetch dependence or wind duration dependence. However, it is illustrative of the richness of the spectral description of a fully developed sea.

4.2 Summary

In this Chapter, we have reviewed some basic oceanographic theory in preparation for the discussions of SAR ocean surface imaging which are found in Chapter 5. An important point is the distinction between the phase and the orbital velocities. These velocities are subject to misleading interpretations within the framework of SAR ocean imaging because of the different ways in which they interact with the observing instrument.

5 SAR Ocean Wave Imaging

Abstract

This Chapter discusses the SAR imaging of surface gravity waves, a topic which remains controversial. The physical scattering mechanisms are outlined. The dominant scattering mechanism is Bragg resonant scattering, which is suggested to be a coherent scattering process. This is contrary to the predominant point of view.

Another controversy surrounds the role and calculation of the scene coherence time. Various decorrelation time estimates are presented and discussed based upon the rms orbital velocity and a relevant cutoff length scale.

Yet another controversy surrounds the roles of the various ocean wave velocity components in the SAR imaging process. It is shown that the phase velocity cannot produce a coherent modulation. Discussion of the noncoherent role of the phase velocity is deferred to Chapter 6. The coherent modulation produced by the orbital velocity leads to velocity bunching. It is shown diagrammatically that the defocussing effects of the orbital acceleration may not be negligible in a velocity bunching model.

Finally, two SAR image phenomena are pointed out, observations of which may help to settle aspects of the ocean imaging controversies: first, waves propagating through ice, a case in which the high frequency wave components are suppressed; and second, narrow "V" ship wakes, which are a result of scattering from Bragg scale waves produced by the ship.

The study of SAR imaging of surface gravity waves is an interesting and challenging problem which has been the subject of many recent review articles [23,47,79,80,84,85]. There are at least three areas of potential controversy: first, the (nature of the) scattering mechanism; second, the importance and calculation of the scene coherence; and third, the appropriate wave velocity for coherent Doppler modulations. Each of these controversial issues are addressed in this Chapter.

5.1 Scattering Mechanisms

It is generally accepted that three physical microwave backscattering mechanisms could be relevant for SAR imaging of the ocean surface. These are specular reflection, wedge scattering, and Bragg resonant scattering.

5.1.1 Specular Reflection

Specular reflection is conventionally understood to be direct reflection by mirror-like planes or facets for which the angle of incidence equals the angle of reflection.

Two conditions must be satisfied by the scattering surface [82]: first, the facet size must be at least of the order of the radar wavelength; and second, the facet must be oriented perpendicular to the radar line of sight. Wave steepness seldom reaches a typical angle of incidence before breaking occurs. Thus, even for a satellite SAR with an incidence angle of 22°, true specular reflection will seldom contribute to the energy backscattered to the radar. However, if the wave is breaking, or becomes concave curled while breaking, this mechanism could have a role. In such a case, the microwave returns are coherently modulated by the long wave phase velocity.

5.1.2 Wedge Scattering

If the ocean wave is cusped, a wedge scattering component may be important in describing the backscattered microwave energy [44]. Such a mechanism applies to regions in which the scattering surface has a radius of curvature which is small compared with the radar wavelength and is most significant when the angle of incidence is relatively large (say $> 45°$). The microwave returns from this mechanism are specular in nature for a given wave crest and are coherently modulated by the velocity of the cusped region which is, again, the long wave phase velocity.

5.1.3 Bragg Resonant Scattering

Bragg resonant scattering is considered to be the most important backscattering mechanism for SAR ocean surface imaging. The separation wavenumber between the long waves and the Bragg scale waves has been estimated to be [23]

$$K_{\text{emh}} = \frac{K_{\text{B}}}{5}\,, \tag{82}$$

where the subscript emh stands for electromagnetic-hydrodynamic. Thus, the scattering may be regarded as arising from small facets, or "patches," of nominally five Bragg wavelengths across. The complex amplitude of the reflectivity from these patches is

assumed to vary slowly with time and be uncorrelated with neighboring or overlapping patches [23,79,80]. The use of K_{emh} as a parameter of interest is admittedly heuristic.

An enhanced surface roughness and, hence, radar cross-section, is associated with the long wave crests due to straining of the Bragg scale waves. This radar cross-section modulation mechanism is termed the hydrodynamic modulation mechanism, and is relevant for all radars operating with a Bragg wavelength of the order of 10 cm, being most important for range travelling waves [3].

The tilting of short gravity waves riding upon long gravity waves results in a spatially variable local angle of incidence, and hence, relevant Bragg subset. It has been proven that HH polarization is more sensitive to wave slopes than VV polarization, that range travelling waves are more readily imaged by this mechanism, and that the maximum radar cross-section is associated with the trailing face of a wave moving away from the radar, and with the leading face of a wave moving towards the radar, being 90° out of phase with the hydrodynamic modulation [3]. This radar cross-section modulation mechanism is termed the tilt modulation mechanism, and is relevant for steeper incidence angle radars.

5.1.4 Bragg Scattering Nature

A fundamental question is whether the nature of Bragg resonant scattering is specular or diffuse. Usually, it is dismissed as purely diffuse [23]. However, a single "patch" of Bragg resonant waves produces a coherent, hence, specular-like return [64]. Furthermore, a coherent geometry is required for this mechanism to produce any microwave reflection at all. Only when an ensemble of such "patches" are present in a given resolution cell can the return become diffuse in nature.

5.2 Ocean Wave Velocities

Attention is now focussed upon the surface motions induced by the long waves. This is the third effect of the long waves upon the Bragg scale waves. Some investigators favour models which coherently respond to the long wave phase velocity, while others favour orbital velocity models. This issue is addressed in the balance of this Section and in Chapter 6.

5.2.1 The Phase Velocity

The phase velocity cannot lead to coherent Doppler modulation of the SAR signal. This assertion is based upon an argument which is adapted from Raney and Lowry [66]. Assume that the radar return from an arbitrary point target on the ocean surface is coherently modulated by the long wave phase velocity C_p. The radial component of this velocity is

$$v = C_p \sin\phi \sin\gamma \,, \tag{83}$$

where the angles are defined in Fig. 8. It is a fact that any coherently sensed radial velocity component leads to Doppler suppression of the response in accordance with the first exponential term in equation (28). For matched filter processing, the Doppler suppression is given by $\exp\{-2\pi(v/\beta V)^2\}$. Thus, the response to a point target will be essentially obliterated if

$$\left|\frac{v}{V}\right| > \beta \,. \tag{84}$$

For the target to be imaged at all, the phase velocity must satisfy

$$\frac{C_p \sin\gamma\,|\sin\phi|}{V} < \beta \,. \tag{85}$$

For typical airborne SAR parameters ($V = 130$ m/s, $\beta = 1.9°$, $\gamma = 45°$) and a 150 m ocean wavelength ($C_p = 15.3$ m/s), the wave must satisfy $\phi < 23°$. That is, the wave must be essentially azimuthally travelling if it is to be imaged at all. Rangeward propagating surface gravity waves, in fact, are regularly (and predominantly) observed

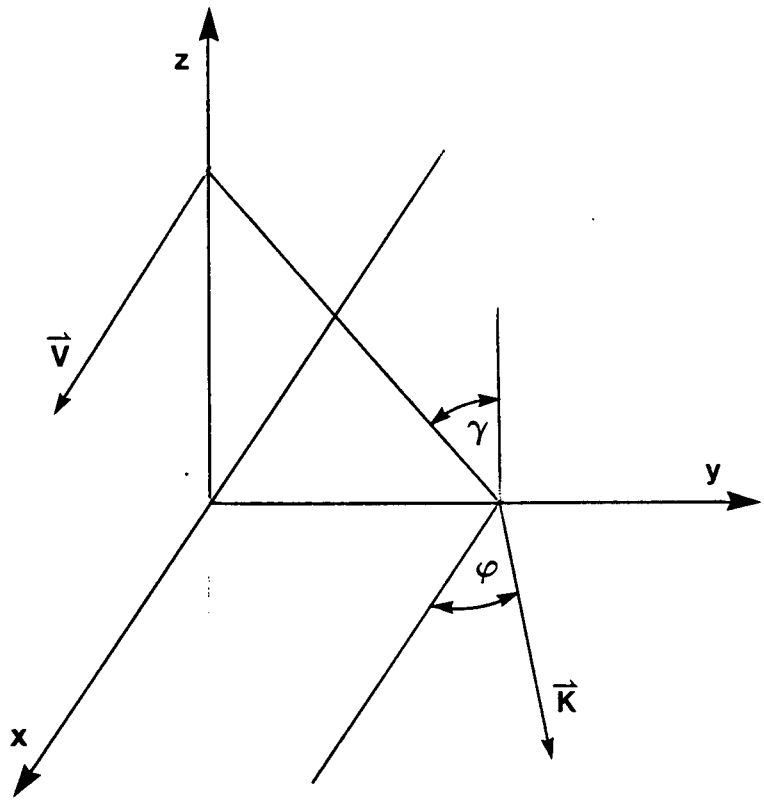

Figure 8: Definition of the angle of propagation.

in airborne SAR imagery. Thus, direct coherent sensing of the long wave phase velocity cannot be a relevant mechanism in the SAR imaging process.

The long wave phase velocity may enter the imaging process in a noncoherent fashion. That is, patterns of enhanced reflectivity associated with the wave crests may translate at the phase velocity. This does not necessarily imply coherent Doppler modulation at the projected phase velocity. The implications of the noncoherent role of the phase velocity are discussed in Chapter 6.

5.2.2 The Orbital Velocity

Vertical velocity components imparted upon the Bragg scattering patches by the orbital velocities associated with the passage of a long ocean wave lead to SAR imaging via the velocity bunching model [1,62,77]. Positive and negative velocity components along the SAR's radial line of sight lead to forward and rearward shifts in the apparent scatterer locations. This causes a redistribution of reflectivity density in the SAR image, appearing as a linear wave-like feature under some conditions.

The radial orbital velocity component is[11]

$$v(x,t) = \Omega A \sin(Kx - \Omega t) \cos\gamma \,. \tag{86}$$

If the wave period $T_w = 2\pi/\Omega$ is much longer than the available coherent integration time T, using equation (30), a target originally located at x is relocated to

$$x' = x + \Lambda\alpha \sin(Kx) \tag{87}$$

[11] In the event that the wave is not azimuthally travelling ($\phi \neq 0$) the radial velocity becomes [4]

$$v(\vec{x},t) = \Omega A\, g(\gamma,\phi) \sin\left(\vec{K}\cdot\vec{x} + \delta\right) \,,$$

where

$$g(\gamma,\phi) = \sqrt{\sin^2\gamma \sin^2\phi + \cos^2\gamma} \,,$$

and

$$\delta = \tan^{-1}(\tan\gamma \sin\phi) \,.$$

This formulation accounts for the contribution of the horizontal orbital velocity component to the net radial velocity.

in the resulting image, where $\Lambda = 2\pi/K$ is the wavelength, and

$$\alpha = \sqrt{2\pi g}\frac{hA}{V\Lambda^{3/2}} \,. \tag{88}$$

The parameter α is the maximum fractional amplitude of the azimuthal target shift. Fig. 9 conceptually shows the effect of the redistribution of target density. The vertical lines are displaced in azimuth in accordance with equation (87). The line density in the figure is proportional to the radar reflectivity which is taken to be uniform in azimuth before the motion effects are introduced[12]. The differential velocities tend to bunch the targets near the wave trough, regardless of the relative propagation direction (*i.e.* to the left or the right in the figure). This radar cross-section modulation mechanism is termed the velocity bunching mechanism, and is relevant for coherent radars such as SAR. The effect is strongest for azimuthally travelling waves.

Raney [62] showed that the azimuth mapping becomes critical when $\alpha = 1/2\pi$. If $\alpha \leq 1/2\pi$, the target redistribution is one-to-one and results in a single band of enhanced reflectivity near the wave trough in the resulting image. If $\alpha > 1/2\pi$, the mapping becomes many-to-one and results in a pair of bands of enhanced reflectivity for each wavelength in the resulting image.

The radial acceleration component of the wave is

$$a(x,t) = -\Omega^2 A \cos(Kx - \Omega t) \cos\gamma \,. \tag{89}$$

[12] Assuming the initial uniform target density

$$f_X(x) = \begin{cases} \frac{1}{2\pi}\,, & \text{if } -\pi \leq Kx < \pi \\ 0\,, & \text{otherwise} \end{cases}$$

is subject to the mapping

$$x' = x + \Lambda\alpha \sin(Kx) = g(x)\,,$$

the resulting target density is

$$\begin{aligned} f_{X'}(x') &= f_X(x)\left|\frac{dx}{dx'}\right|_{x'=g^{-1}(x)} \\ &= \frac{1}{2\pi}\left|\frac{1}{1+2\pi\alpha\cos(Kx)}\right| \,. \end{aligned}$$

This mapping is one-to-one if $2\pi\alpha < 1$ and is linear (in a linear systems theory sense) if $2\pi\alpha \ll 1$. A guideline for linear mapping is $2\pi\alpha \ll 0.3$. If $2\pi\alpha \geq 1$, the density function has one or more singularities. Such singularities are not of consequence since they are tempered by the system resolution.

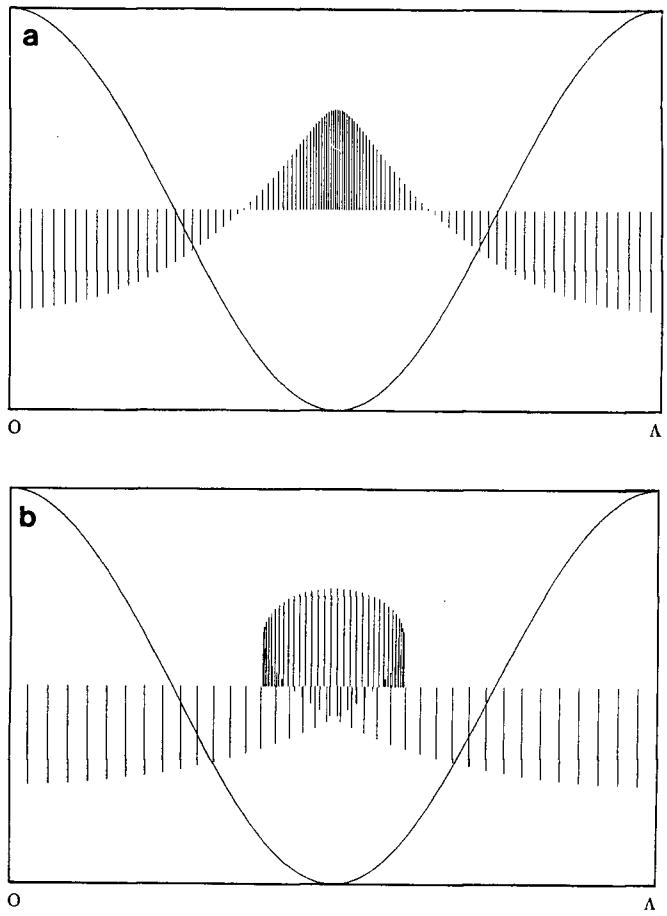

Figure 9: Conceptual velocity bunching diagram.
The abscissa is proportional to the azimuthal coordinate. The solid line represents the nominal ocean surface. The vertical lines are proportional to the radial acceleration component; their density is proportional to the mean reflectivity; and the lines have been relocated in azimuth by the radial velocity component. Cases shown are a) $\alpha = 1/3\pi$ (one-to-one mapping), and b) $\alpha = 1/\pi$ (many-to-one mapping). This representation including velocity and acceleration effects is new.

The vertical lines in Fig. 9 are proportional to this acceleration component. The defocussing effects of the acceleration component are significant if

$$\left|\frac{aR_0}{V^2}\right| \geq \frac{2N}{TB} \tag{90}$$

for a multi-look matched filter processor. Note that large radial accelerations occur near the regions of peak target density. Thus, the defocussing effect of the radial acceleration component opposes the effects of velocity bunching and may not be negligible. This is a new result and may be important in some applications.

The azimuthal orbital velocity component u is 180° out of phase with the radial acceleration component a. The relative importance of a and u may be judged by

$$E = \frac{|2u/V|}{|R_0 a/V^2|} = \sqrt{\frac{2\Lambda}{\pi g}}\frac{V}{R_0}\,, \tag{91}$$

the ratio of the along track velocity defocus term to the radial acceleration defocus term. For typical SAR parameters, and all practically observable ocean waves, $E \ll 1$, showing that acceleration defocus always dominates along track velocity components of the orbital motion.

Appendix D discusses a one-dimensional simulation of monochromatic, azimuthally travelling ocean waves which has been utilized to further illustrate velocity bunching. It is shown that acceleration defocus may be important and will oppose the effects of velocity bunching. It is also shown that Doppler suppression may be important for an airborne SAR.

5.3 Scene Coherence

We now turn to estimation of the relevant scene coherence time in the presence of ocean waves. In Chapter 2, it was shown that target motion may be modelled as a multiplicative phase given by

$$\beta(t) = \exp\left\{-j\left[\frac{B}{T}\left(t_D t + \hat{\eta}t^2\right) - \theta(t)\right]\right\}\,, \tag{92}$$

where the motion parameters $t_D = R_0 v/V^2$ and $\hat{\eta} = R_0 a/V^2$ are the results of averaging over the duration of a given look. (The along track orbital velocity component has been neglected as per Section 5.2.2.) The random variable $\theta(t)$ represents the coherence of individual patches of Bragg waves. Of relevance here is the intrinsic coherence time of such a patch, and the decorrelation time of such a patch from other such patches.

5.3.1 Intrinsic Scale

The intrinsic coherence time scale refers to the time over which a given patch of Bragg waves coherently retains it structure. There is no theory nor explicit estimates for such a time scale. However, a general assumption is that the complex reflectivity amplitude from such a patch varies slowly [23,79] so that the intrinsic coherence time scale is long compared with the available coherent integration time.

5.3.2 Decorrelation Scale

The decorrelation coherence time scale refers to the time over which a given patch of Bragg waves remains co-phase relative to itself, and relative to other such patches. This time scale is generally related to the rms surface velocity, $v_{\rm rms}$, as indicated in equation (39). Thus, estimation of τ_c requires estimation of $v_{\rm rms}$ over the ensemble of wave motions.

The magnitude of $v_{\rm rms}$ may be calculated from the integration [2,46,79,80]

$$v_{\rm rms}^2 = \int_{\Omega_1}^{\Omega_2} \Omega^2 S_\zeta(\Omega)\, d\Omega\,, \tag{93}$$

where $S_\zeta(\Omega)$ is the one-dimensional frequency spectrum of surface elevation. A closed form expression may be found for $v_{\rm rms}^2$ by using the Pierson-Moskowitz spectrum. Then, we find that

$$v_{\rm rms}^2 = \sqrt{\frac{\pi}{\beta}} \left(\frac{\alpha U^2}{4}\right) \cdot \mathrm{erf}\left\{\sqrt{\beta}\left(\frac{g}{U\Omega}\right)^2\right\} \cos^2\gamma \Big|_{\Omega_2}^{\Omega_1}. \tag{94}$$

It remains to specify the limits of integration.

The high frequency limit Ω_2 has not been controversial. This limit corresponds roughly to the frequency of the Bragg waves and one can use $\Omega_2 \longrightarrow \infty$ with little error. Then, we find that

$$v_{\rm rms}^2 = \sqrt{\frac{\pi}{\beta}}\left(\frac{\alpha U^2}{4}\right)\cdot \mathrm{erf}\left\{\sqrt{\beta}\left(\frac{g}{U\Omega_1}\right)^2\right\}\cos^2\gamma \tag{95}$$

$$= \sqrt{\frac{\pi}{\beta}}\left(\frac{\alpha U^2}{4}\right)\cdot \mathrm{erf}\left\{\sqrt{\beta}\frac{g\Lambda_1}{2\pi U^2}\right\}\cos^2\gamma \tag{96}$$

where the deep water dispersion relation is used to replace Ω_1 by Λ_1. If the argument of the error function is small compared with unity, we may write

$$v_{\rm rms}^2 = \frac{\alpha g}{4\pi}\Lambda_1\cos^2\gamma\,, \tag{97}$$

so that

$$\tau_c = \sqrt{\frac{\pi}{\alpha g\Lambda_1}}\frac{\lambda}{\cos\gamma}\,. \tag{98}$$

The wavelength Λ_1 represents a sharp cutoff between waves which are treated in a statistical manner ($\Lambda \leq \Lambda_1$) and waves which are treated in a deterministic manner ($\Lambda > \Lambda_1$). The interesting issue is reduced to consideration of the lower limit Λ_1. There are several choices. Some investigators [2,79,80] choose $\Lambda_1 = 2\rho$: twice the matched filter processor, one-look resolution. Then

$$\tau_c = 4.45\frac{\lambda}{\sqrt{\rho}\cos\gamma}\,. \tag{99}$$

Typical coherence time scales based upon this and other results derived in this section are summarized in Table V for the SEASAT SAR and the C-SAR.

Such a choice for the cutoff wavelength Λ_1 is questionable for several reasons. First, no account is given for the effect (if any) of multi-look processing. Second, the resolution scale is dependent upon the processor configuration (and for that matter, the resolution measurement norm) and hence, is arbitrary to within a factor of (say) two. Finally, the actual relevant one-look resolution may be substantially degraded through the presence of target radial accelerations, and may be orders of magnitude larger than the intended

Table V: The coherence time scale in msec for the various cutoff wavelengths considered.

Λ_1	SEASAT	C-SAR
2ρ	445	315
$\frac{g}{2\pi}T^2$	550	355
∞ ($H_s = 4$ m)	140	40

static theoretical one-look resolution ρ. Given the variability of the effective resolution, this approach to estimating the cutoff wavelength scale might best be done through iteration.

A second choice for the cutoff wavelength Λ_1 is based upon the available coherent integration time. Any wave with period less than or equal to T will pass through at least one complete cycle over the course of image formation. The corresponding cutoff scale is

$$\Lambda_1 = \frac{g}{2\pi}T^2 \ , \tag{100}$$

which results in

$$\tau_c = 5.04\frac{\lambda}{T\cos\gamma} \ . \tag{101}$$

A third choice for the cutoff wavelength Λ_1 is to assume that the velocities of all spatial scales contribute to $v_{\rm rms}$ (as a worst case estimate) [46]. Then $\Lambda_1 \longrightarrow \infty$ so that

$$v_{\rm rms}^2 = \sqrt{\frac{\pi}{\beta}}\left(\frac{\alpha U^2}{4}\right)\cos^2\gamma \ . \tag{102}$$

Thus, we find that

$$\tau_c = 1.12\frac{\lambda}{\sqrt{H_s}\cos\gamma} \tag{103}$$

is a lower bound estimate of the coherence time. Results for this formulation based upon a 4 m significant waveheight are included in Table V.

An order of magnitude range of coherence time scales is available from these approaches as is illustrated in Table V. The estimates based upon inherent SAR length

scales seem independent of both sea-state and ambient environmental conditions—a situation which seems unlikely. The estimate based upon the entire wave spectrum seems more sensible from this point of view in that there is significant waveheight and hence, windspeed dependence. However, as we will see in Chapter 8, even the shortest estimated coherence time scale based upon the latter estimate is rather longer than that which is observed. This indicates the inadequacy of the decorrelation time scale approach, and might suggest that the intrinsic scale is somewhat shorter than indicated.

5.4 Waves in Ice

The first observations of ocean waves propagating into an ice-covered region in SAR imagery were made about 10 years ago by Dawe and Parashar [14]. Recently the analytical opportunities presented by such observations have been suggested by Raney [62]. An important observation is that the intensity patterns of such waves appear cusped in SAR imagery when an azimuthal wavenumber component is present. This suggests that focus and coherence time limitations are not issues. Focus is shown to be negligible in Appendix D for multi-look SAR's in a one-to-one velocity bunching model. Furthermore, the ice-cover is a low-pass filter, effectively eliminating the high frequency surface waves which decrease the coherence time. Thus, the same gross dynamics are present in the ice-covered case as in the open ocean case, but there is no coherence time limitation.

Recent LEWEX observations [15] (see Appendix C) successfully obtained SAR imagery of ocean waves with an azimuthal wavenumber component propagating into an ice covered region. Representative imagery of waves in ice is shown, discussed, and compared with simulations in Chapter 8.

5.5 Narrow "V" Ship Wakes

The SAR image of a ship wake seldom appears to be dominated by the classic Kelvin wake pattern. More usual, if the ambient conditions are suitable, is a narrow

"V" appearance, which is generally associated with azimuthally travelling ships. It has recently been established [41,42] that this SAR image phenomenon is a result of scattering from Bragg scale waves excited by the passage of the ship. This result is based upon the observation that the narrow "V" wake opening half-angle is consistent with the angle

$$\mu = \tan^{-1}\left(\frac{C_g \cos\phi_l}{V_s}\right), \tag{104}$$

where C_g is the group velocity of the Bragg scale waves, ϕ_l is the ship heading with respect to azimuth, and V_s is the ship speed.

Such imagery provides an opportunity to directly observe and assess the nature of Bragg scattering since the linear target pattern is a direct result of Bragg scattering. The coherence time associated with the point targets which constitute the wake is long because such image phenomena persist over large spatial scales.

The imagery of a linear target (a line of point targets), a model for one arm of a narrow "V" wake, is discussed in Appendix B. It is shown that the width of the linear target modeled in such a fashion will respond to a focus error in the perpendicular image dimension—the range dimension for a narrow "V" ship wake. These points are discussed further in Chapter 8.

5.6 Summary

This Chapter has discussed aspects of the SAR imaging of ocean surface waves. For example, it is asserted that the Bragg scattering associated with the ocean surface is a coherent, specular-like process. This is not the traditional interpretation of Bragg scattering, although it is consistent under logical analysis.

Coherence time scales based upon the decorrelation of Bragg scattering cells were calculated for various cutoff wavelength scales and a Pierson-Moskowitz wave spectrum. The scales calculated are summarized in Table V and range from 40 msec to 500 msec.

It was shown that the wave phase velocity cannot lead to coherent Doppler modu-

lations. The wave phase velocity enters the imaging process as the translation velocity of the mean reflectivity envelope. This concept is discussed further in Chapter 6. Only the orbital dynamics may lead to coherent Doppler modulations. The radial component of the orbital velocity leads to velocity bunching while the radial component of the orbital acceleration may cause image defocus.

This Chapter concludes by introducing two SAR image cases which may help to solve some of the controversy which surrounds SAR ocean imaging. These are waves in ice, a case in which coherence time limitations are not an issue, and the narrow "V" ship wake, a case in which Bragg scale waves are directly observed.

6 Dynamic Reflectivity Patterns

Abstract

In this Chapter, the effects of the dynamics of the mean pattern envelope of the ocean's reflectivity are distinguished from the effects of the dynamics of the individual point targets which constitute the reflectivity pattern. It is argued that the effect of frequency offset look-extraction windows combined with envelope motion causes the envelope image to become misregistered when combining looks. It is shown that the resolution, and hence the image contrast, is minimized when the fractional processor focus error is adjusted by $\eta = v_E/2\cos\phi$. This result is typically interpreted as arising due to a coherent Doppler modulation at an azimuthal velocity of $v_E/2\cos\phi$. In fact it arises because one effect of a processor focus error is to adjust the registration of the individual looks. Thus, the processor focus adjustment is simply re-registering the individual looks which were misregistered by the noncoherent envelope motion. This re-registration is at the expense of actual misfocus of the processor. True optimal processing uses fixed correct focus and independent re-registration of the looks. These observations constitute the contributions of this Chapter.

The case of an airborne multi-look SAR imaging an azimuthally travelling reflectivity pattern is considered in this Chapter. The objective is to clarify issues surrounding the controversy over the effect of a processor focus adjustment upon the image contrast of such scenes. Observations indicate that a processor focus perturbation proportional to the projected pattern velocity will improve the image contrast. We will show that this does not imply a coherent Doppler modulation at this velocity. The consequences have an important bearing upon the scattering mechanisms being investigated.

6.1 Development

Assume that a SAR is being used to observe a moving reflectivity pattern. By way of example, consider the imaging of a wind gust pattern or "cat's paw" excited upon an otherwise calm water surface. The wind roughened region may be modelled as consisting of many small coherent regions or patches of roughness, each of which produces a coherent return to the radar such as that derived from a point target. The mechanism for producing such returns is irrelevant to the present discussion. The ensemble of all such patches, or point targets, constitutes the noncoherent reflectivity pattern that we associate with the radar image.

There are two sets of dynamics which are relevant to this example. The first is the dynamics of the individual point targets. The motions of the individual targets can coherently (phase) modulate the returned radar signal. These effects (discussed in Section 2.2 for point targets and in Section 3.1.2 for diffuse targets) are the ones most frequently found in the SAR ocean literature.

The second set of dynamics is the motion of the pattern itself, particularly the velocity of the envelope of the mean reflectivity pattern. The reflectivity envelope velocity cannot coherently modulate the returned radar signal. The reflectivity envelope velocity is not necessarily the same as the velocity of the individual point targets which constitute the pattern. Differences between these velocities are vital since the targets which constitute the pattern do not move at the wave phase speed (Chapter 5).

A recognized effect of the reflectivity envelope is the scanning distortion which arises when the envelope velocity becomes an appreciable fraction of the platform velocity [66]. This effect is regularly observed in airborne SAR imagery of ocean waves and wave imagery derived from other airborne scanning sensors such as the surface contour radar [87].

We will now consider another role of the azimuthal velocity component of the reflectivity envelope v_E, in the event of multi-look processing. Recall that in a multi-look processor, data windows are applied in the frequency domain to generate the individual looks. These data windows may be separated by a Doppler frequency of Δf_D. From equation (10), this corresponds to a time separation between the looks of $\Delta t = \Delta f_D / K_a$. This implies that the image of the reflectivity envelope will be misregistered in the azimuth between the two looks by a distance $\Delta x = v_E \Delta t$. Then, in the output image plane, the corresponding temporal offset is $\delta t = (v_E/V)\Delta t$. Thus, the effect of the envelope velocity is to differentially shift the relative location of each look in azimuth. This same effect has been demonstrated in two-scale radar wave probe data [56].

The analysis of Chapter 2 may be extended to include the effect of the reflectivity

envelope velocity. The net effect is to shift each look in azimuth by an amount

$$\delta t = \left(\frac{T}{T_l}\right)^2 \frac{t_i}{K}\frac{v_E}{V} , \tag{105}$$

where $(T/T_l)^2 t_i/K$ is the centre of the effective look extraction window. This effect may be introduced into the formulation after coherent processing is complete since it is a noncoherent effect.

The single look dynamic impulse response is modified by:

$$g_d(t,t_i) \longrightarrow g_d\left(t - \left(\frac{T}{T_l}\right)^2 \frac{t_i}{K}\frac{c}{V}, t_i\right) . \tag{106}$$

Then, after look-summation we find that

$$g_{dm}(t) = \frac{T^2}{\sqrt{KL + \epsilon^2 + \frac{1}{K}\left(\frac{T}{T_l}\right)^2 [\epsilon_0^2 - 2\epsilon\epsilon_0]}} \cdot \exp\left\{-2\pi \frac{t_D^2}{LT_p^2}\right\}$$

$$\cdot \exp\left\{-2\pi \frac{B^2 K}{K^2 + K\epsilon^2/L + \frac{1}{L}\left(\frac{T}{T_l}\right)^2 [\epsilon_0^2 - 2\epsilon\epsilon_0]} \left[t + \left(1 - \frac{\delta\eta}{L}\right) + \frac{1}{LK}\left(\frac{T}{T_l}\right)^2 \frac{c}{V} t_D\right]^2\right\} , \tag{107}$$

where $\epsilon_0 = TB(v_E/V)$. This result has resolution

$$\rho_m = \sqrt{\frac{K}{L}\left\{1 + \frac{\epsilon^2}{KL} + \frac{1}{K^2 L}\left(\frac{T}{T_l}\right)^2 [\epsilon_0^2 - 2\epsilon\epsilon_0]\right\}} . \tag{108}$$

It can be shown that the resolution ρ_m is minimum when

$$\eta = \frac{1}{K}\left(\frac{T}{T_l}\right)^2 \frac{v_E}{V} = \frac{N^2 - 1}{N^2}\frac{v_E}{V} , \tag{109}$$

where the second equality applies to both matched filter and infinite rectangular filter processing. For $N > 1$, we find that $\eta \sim v_E/V$ will minimize the resolution, and hence, maximize the image contrast[13]. This result arises because one effect of a focus adjustment is to change the azimuthal registration of the looks. Thus, a change in the coherent processor parameters decreases the impact of this noncoherent effect upon the output image.

[13]See footnote 6 on page 17.

A better technique to provide such a correction is to noncoherently combine the sequence of coherently generated looks, shifting each look in accordance with the offset produced by the envelope velocity given in equation (105). Using this approach, the image contrast will be further enhanced because no broadening of the individual impulse responses will result, as is the case when the focus parameter is adjusted to align the misregistered looks.

This degradation in contrast due to the envelope velocity also applies to the case of one-look processing. This is because a moving scene is being imaged over time by a moving sensor (analogous to a time-exposed photograph of a moving subject). The output is smeared in accordance with the velocity ratio v_E/V over the course of the observation time. This effect applies within each look of a multi-look set as well. However, as N becomes large, the observation time is reduced, as is the degree of smearing. Thus, as the number of looks becomes large, the above analysis becomes more exact.

An identical focus perturbation will cause the SAR to track the moving reflectivity envelope and similarly improve the contrast of a one-look image. This also applies to the individual looks of a multi-look image [67].

If the processor focus error required to register the looks is related to an equivalent azimuthal velocity component v, we find that $v = v_E/2$. It is tempting to interpret the effect of the envelope velocity as a coherent Doppler frequency modulation leading to a broadening of the response due to a focus error. However, to make such a leap is incorrect. It illustrates the danger of interpreting processor focus perturbations in terms of an equivalent coherently-sensed velocity component, which in turn implies oceanic targets moving with velocity $v_E/2$. Of course, such is not the case. This issue is one of intense controversy in this area due to the experimental focus paradox which this section addresses.

The effect of the velocity of an envelope of reflectivity applies to other notable

situations. One example is the imaging of ocean waves with an azimuthal wavenumber component. Through several mechanisms an imaged reflectivity pattern is produced which travels with the wave at the wave phase velocity C_p. However, the individual point targets which constitute the pattern are coherently modulated by the wave's orbital velocity. Thus, processor focus perturbations proportional to the projected azimuthal component of the phase velocity will tend to register the looks and improve the contrast in both the wave image and wave spectra derived from the image. If the ocean wavenumber vector makes an angle ϕ with the platform velocity vector, the projected azimuthal component of the pattern velocity is $C_p/\cos\phi$. The processor focus perturbation required to "optimally" focus SAR imagery of the waves is $\eta = C_p/2\cos\phi$. This result is consistent with observations [28,72,74] that ocean wave image contrast is maximized by a focus adjustment proportional to the projected azimuthal phase velocity. (This effect is not observed in satellite SAR imagery [73] simply because C_p/V is extremely small and the depth of focus is relatively large.)

It is stressed that this result does not imply a coherent Doppler frequency modulation proportional to the projected phase velocity, and that true optimal processing uses fixed correct focus, and independent re-registration of the looks.

6.2 Summary

This Chapter has addressed the apparent paradox that optimal SAR ocean wave image contrast is observed when the processor focus is perturbed in proportion to one-half the projected phase velocity, yet the phase velocity cannot produce coherently sensible Doppler modulations. The paradox is resolved by noting that the mean reflectivity envelope translation velocity is the wave phase velocity, and that this translating pattern is imaged over a non-zero period of time by the SAR. In the event of multi-look processing, the envelope translation leads to misregistration of looks which may be corrected by the previously mentioned focus perturbation. This is because one effect of a

processor focus perturbation is to change the relative registration of the looks. True optimal processing should retain the correct focus and independently re-register the looks.

7 Analysis Methodology

Abstract

This Chapter presents the analysis methodology used in the remainder of this work. A new two-dimensional simulation model is motivated, with development contained in Appendix A. Outputs of the simulation may be compared directly with actual SAR image phenomena. This Chapter also contributes a methodology to extract three statistical parameters from multi-look SAR data which may be used to address the question of target density in an arbitrary SAR image. The parameters include the inter-look cross-correlation, the peak-height scaling in response to look summation, and the azimuthal image bandwidth. These parameters may be extracted from simulated or actual SAR imagery in the same manner.

The analysis tools used in this work fall into two categories: first, a two-dimensional SAR image simulation model is developed to produce controlled images that may be compared qualitatively with actual SAR imagery; and second, a series of statistical tests is developed specifically to address the nature of scattering in a SAR image. These tests may be applied to simulated imagery to quantify scene behaviour for known parameters. These tests also may be applied to actual SAR imagery, and the results compared with those from simulations to better relate SAR imagery to known parameter variations.

7.1 Simulation

As an aid in understanding the processes involved in SAR ocean surface imaging, a two-dimensional simulation package has been developed. The simulation procedure takes careful account of the scattering nature; there are minimal *a priori* assumptions as to the statistical behaviour of each resolution element, and each point target in the scene is explicitly considered. Thus, the behaviour of the targets in each resolution element is explicitly known. This degree of control and flexibility is not available when studying real SAR imagery. Such a method presents the opportunity to produce a database for comparison to actual SAR imagery, and represents a distinct departure from other simulation based studies.

SAR image simulation has a strong precedent in the design and performance evaluation of various aspects of SAR response and sensitivity. One thrust of such research

has been end-to-end SAR product simulation [21,24], intended primarily to assess geoscience applications, and to aid in SAR system design trade-offs. Such simulations generally require as input some sort of "radar reflectivity map," and in some manner generate a speckle pattern under the assumption of many independent targets, thus implying Rayleigh statistics and derivative forms for the multi-look case [68].

Although simulation should play a role in understanding SAR ocean surface imaging [72], the scene dynamics need to be appropriately represented, as they provide both the interest and difficulty essential to the problem. A one-dimensional (azimuthal) model has been presented by Alpers [1] in which velocity bunching allows image intensity modulations to arise from a randomly generated wave field. More recently, this type of work has been extended to two-dimensions [2,43,86]. These works generally contain one or several inherent assumptions which could prove to be restrictive: diffuse scattering, a large number of looks, or a long scene coherence time. Obviously, implementation of these assumptions into a simulation limits the utility of the simulation for testing the assumptions themselves.

The details of the simulation methodology developed for this work are contained in Appendix A. The simulation is specifically designed to properly represent dynamic distributed targets. It has provisions to simulate varying number of targets per resolution cell, azimuthal wave imaging through the velocity bunching mechanism, linear or distributed targets, target acceleration and processor-induced focus errors, and finite scene coherence time. The simulation is based upon fundamental SAR imaging theory and gravity wave behaviour as developed in previous chapters.

7.2 Statistical Testing Methodology

Table IV on page 33 outlines salient image features which may be used to differentiate between examples of SAR imagery derived from point and diffuse targets. In this section, these features are developed into a statistical testing methodology which may

be invoked to test for the presence of point targets in an arbitrary SAR image.

7.2.1 Inter-Look Cross-Correlation

Observation of the correlation between looks should technically occur on a resolution cell-by-resolution cell basis. However, such a procedure is impractical for two reasons: first, a focus error shifts the relative azimuthal positions of the resolution cells from look to look, making it impossible to track the appropriate resolution cells for a correlation measure in the event of a dynamic ocean surface; and second, a low level of statistical significance is associated with resulting correlation estimates due to the small number of statistically independent samples (essentially equal to the number of looks N). These factors suggest that a spatial correlation measure would be more profitably employed.

The adopted procedure is a straightforward calculation of the correlation coefficient between pairs of looks, applied at nominally perfect focus only. Such a measure is statistically rather reliable because the number of degrees of freedom in the estimate is twice the number of statistically independent resolution cells in each look. About 1000 degrees of freedom are expected for a four-look 128-by-128 pixel subscene from the SEASAT SAR. In the event of target motion or look extraction filter overlap, the number of independent resolution cells is decreased. In this work, the derived statistic is the mean of the correlation from all possible pairs of looks.

In the event of an isolated point target, this statistic is rather dependent upon the processor focus due to possible misregistration of looks in azimuth. Observation of the peak of a cross-correlation function may be more useful in such cases. However, in this work the correlation is measured only at nominally perfect focus.

7.2.2 Peak-Height Scaling

To observe the peak-height scaling as a function of the number of looks to which the SAR data is processed requires that the data be reprocessed with a variety of choices of

N. However, it is impractical and unnecessary that this level of processing be carried out when the individual looks of an N look set are available. In this case, an M look set may be simulated by summing M of the N available looks (where $M \leq N$) followed by a peak-height measurement. Using such a method, the results differ slightly from those indicated in Table IV, but there is no change in interpretation, as discussed presently.

As a measure of peak height, we choose the standard deviation normalized by the mean for the M chosen looks. For either a point or diffuse target, the mean value is proportional to M. In the case of a diffuse target, the standard deviation is proportional to $M^{1/2}$, and the peak-height measure will scale as $M^{-1/2}$. However, for a point target, the peak value will be proportional M so that the peak-height measure will scale as M^0, in contrast to N^{-1} as expected for N-look processing.

This measurement is completed by calculating the mean and standard deviation of all possible combinations of M looks of the available N looks, averaging the results for the peak-height scaling, and performing a first-order least-squares fit to the logarithm of the peak-height scaling data. The coefficient of the linear term is the relevant measure.

Again, this measure is dubious in the event of an isolated point target and a focus error. Point targets may become misregistered, and their sums will not scale as indicated if the misregistration is rather large. This is because the looks considered in this work are derived from a discrete frequency-plane mixed-integrator. Thus, in practice, this measure was performed only upon nominally perfectly focussed imagery.

7.2.3 Azimuthal Image Bandwidth

For a point target, a processor focus error will broaden the image response, thus leading to a decreased image bandwidth. However, for a diffuse target, a processor focus error will cause no change in the second order statistical behaviour of the speckle pattern, and the image bandwidth will be unaffected.

The azimuthal image bandwidth is considered to be the most important measured

parameter because it is explicitly dependent upon processor focus in a well defined fashion for the point and diffuse target cases. The inter-look cross-correlation and the peak-height scaling measures may be regarded as supporting the conclusions derived from this measure. The azimuthal image spectrum is calculated for each look by removing the mean, applying a data window and an FFT to each azimuthal line, and averaging in range to produce an azimuthal spectrum with a number of degrees of freedom equal to twice the number of statistically independent resolution cells in range. The bandwidth is measured on the basis of an equivalent rectangular width for a Gaussian shaped spectrum.

This procedure is applied on a look-by-look basis rather than upon the multi-look image for several reasons: first, the variation in azimuthal bandwidth for a point target is adequate on a look-by-look basis for moderate focus errors in a SEASAT SAR scene to indicate the presence of a point target; second, if the looks are sufficiently misregistered due to the processor focus error, the peaks in the individual looks will appear in the multi-look image, thus corrupting the spectral shape and corresponding bandwidth measure; and third, the bandwidth derived from each of the N looks may be averaged to provide a more statistically reliable measure of the azimuthal image bandwidth.

7.3 Summary

This Chapter has presented the analysis tools which will be used in the remainder of this work. The two-dimensional simulation is unique in that it explicitly considers each of the point targets which are present in a given scene. Details of the simulation are found in Appendix A. The three image statistics which may be derived from multi-look SAR imagery are the inter-look cross-correlation, the peak-height scaling as looks are summed, and the azimuthal image bandwidth as a function of the azimuthal processor focus error. These measures are relatively easy to extract and subject to good statistical reliability. As well, they help to differentiate between SAR imagery of point and diffuse

targets.

8 Simulated vs. Actual SAR Imagery

Abstract

In this Chapter, we perform comparisons between simulated and actual SAR imagery. The comparisons are either quantitative on the basis of extracted observable statistics, or qualitative on the basis of one-to-one comparisons of actual SAR imagery with simulation products. Four sets of comparisons are performed to investigate various SAR ocean imaging characteristics.

The first set of comparisons examines the specular versus diffuse nature of ocean surface scattering. It is shown that test statistics of the simulation and a SEASAT SAR test scene demonstrate the appropriate statistical behaviour for point or diffuse scattering. When applied to an ocean scene the statistics suggest diffuse scattering only. This result is explained on the basis of random target motions and finite scene coherence times leading to large resolution cell sizes.

The second set compares simulations of linear targets with SEASAT SAR imagery of narrow "V" ship wakes. The linear targets and narrow "V" wakes should behave in a specular manner. The "V" wake represents direct observation of ship generated Bragg waves, suggesting that Bragg scattering is a coherent process.

The third set compares simulations of azimuthally travelling ocean waves having various mean scene coherence times with C-SAR imagery of waves in the open ocean propagating into an ice-covered region. The role and degree of coherence time limitation in airborne SAR imagery is demonstrated. A scene coherence time of 1/4 msec seems appropriate for the ocean case.

The fourth set considers near and far range C-SAR imagery of waves propagating through an ice-covered region. It is shown that the range dependent azimuthal look misregistration due to the translating reflectivity envelope is consistent with theory. This reinforces the noncoherent motion effects discussed in Chapter 6.

This Chapter draws quantitative and qualitative comparisons between simulated and actual SAR imagery. Comparisons are drawn in four areas: first, to assess the ocean surface target density in SEASAT SAR imagery; second, to assess the nature of the scattering associated with narrow "V" ship wakes in SEASAT SAR imagery; third, to assess the size of the coherence time in C-SAR wave imagery and wave in ice imagery; and fourth, to directly observe the effects of a moving envelope of reflectivity.

8.1 Specular vs. Diffuse Scattering

Recall that microwave reflectivity from the ocean surface is largely a Bragg scattering process. Also, recall the assertion that Bragg scattering is a coherent scattering process for each Bragg scattering region. We will now examine this assertion by applying the statistical tests developed in Chapter 7 to three data sets: first, to simulated

SEASAT SAR imagery of variable target density and processor focus errors; second, to actual SAR data of a scene containing known examples of point and diffuse targets obtained by SEASAT [33]; and third, to an actual SEASAT SAR scene of the ocean surface.

8.1.1 SEASAT SAR Simulation

SEASAT SAR scenes of variable target densities with various processor focus errors were simulated. The test statistics were extracted from the results. Details of this analysis are contained in Appendix B. In that Appendix, it is demonstrated that the simulations exhibit appropriate asymptotic behaviour for approach to the diffuse and specular scattering limits on the basis of the extracted test statistics. However, these asymptotes are approached rather slowly. It is also apparent that even cases which behave in a rather specular-like manner are not accompanied by noticeably different image appearance, perhaps suggesting why ocean reflectivity is traditionally dismissed as being diffuse in nature.

Based upon these observations, subsequent simulations of ocean surface phenomena were performed with a rather small target density—generally 3 targets per resolution cell. This choice is less than the traditional guideline of 5 [34], yet does not noticeably impact qualitative comparison of actual SAR imagery with the simulation product, as shown presently.

8.1.2 SEASAT SAR Control Scene

The control scene chosen is Goldstone California, taken from SEASAT orbit 882. This scene contains an array of immobile corner reflectors which are used as examples of discrete point targets, and regions of desert which are used as examples of diffuse targets. The scene is shown in Fig. 10, and the extracted 128-by-128 pixel subscenes used in the testing are indicated. Subscene 1 contains the corner reflector array which

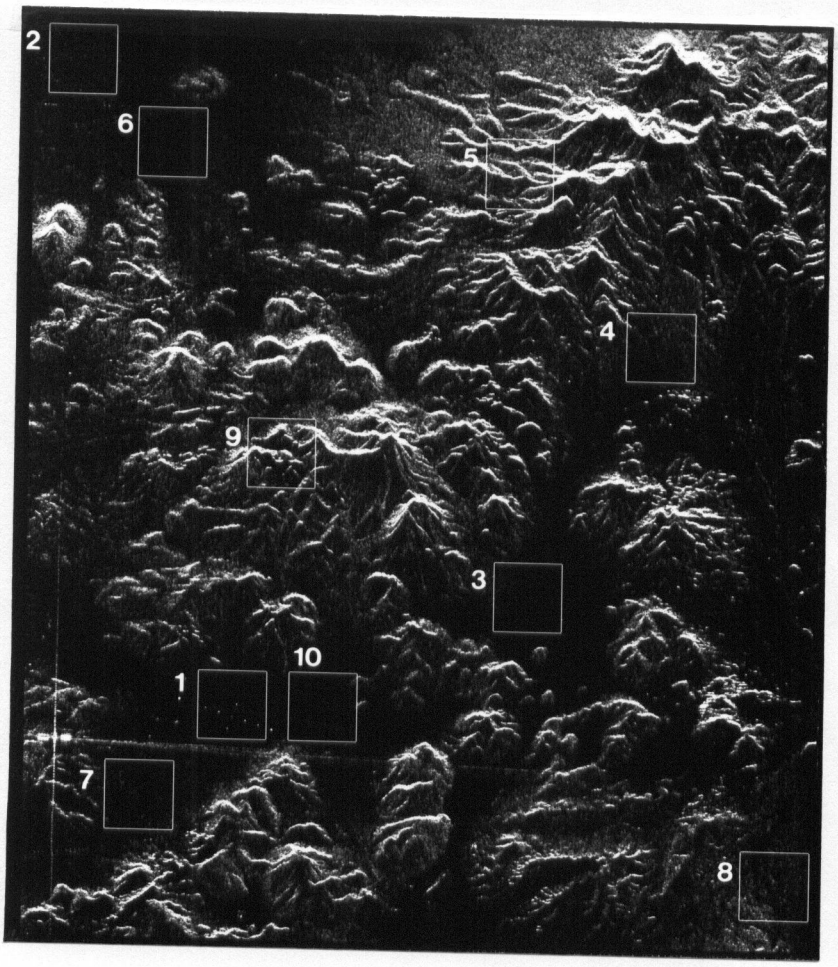

Figure 10: SEASAT SAR Goldstone California scene showing extracted subscenes. The azimuthal coordinate is horizontal while the (slant) range is vertical.

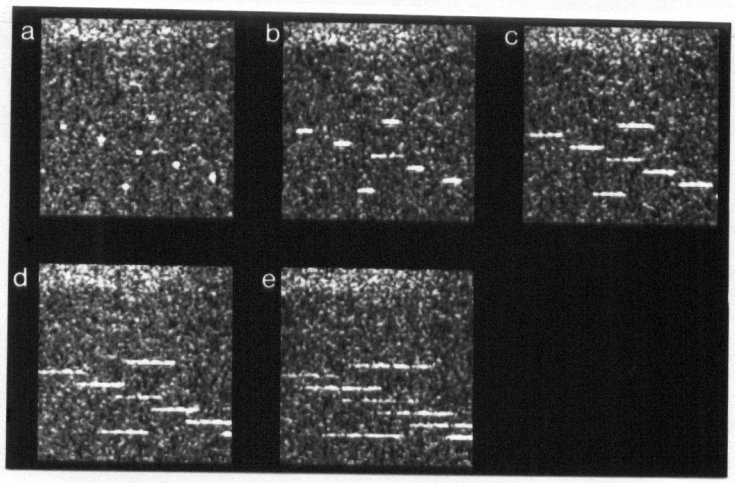

Figure 11: Goldstone subscene 1 with the five processor focus errors.
a) 0%, b) 1%, c) 2%, d) 3%, and e) 5% corresponding to about 0, 1, 2, 3, and 5 depth of foci error in each look of this four look set. The azimuthal coordinate is horizontal.

correspond to isolated point targets. Subscenes 2, 3, 6, and 7 contain expanses of desert which correspond to diffuse targets. Subscenes 5 and 9 contain imagery of mountains which are regions of high contrast. Subscenes 4, 8, and 10 contain regions with lower contrast.

Fig. 11 shows subscene 1, the case of discrete point targets, with the five processor focus errors. As the focus error increases, the peaks associated with each corner reflector broaden in azimuth. Eventually, the individual peaks associated with the response of each look become apparent in the multi-look image. This illustrates why the peak-height scaling and cross-correlation measures do not apply to isolated point targets with a large processor focus error. (The look misregistration also illustrates the autofocus algorithm.)

Fig. 12 corresponds to subscene 2, a diffuse case. As the processor focus error changes, there is very little change apparent in the speckle or the scene contrast. Note that the range of focus change is the same as that used in Fig. 11.

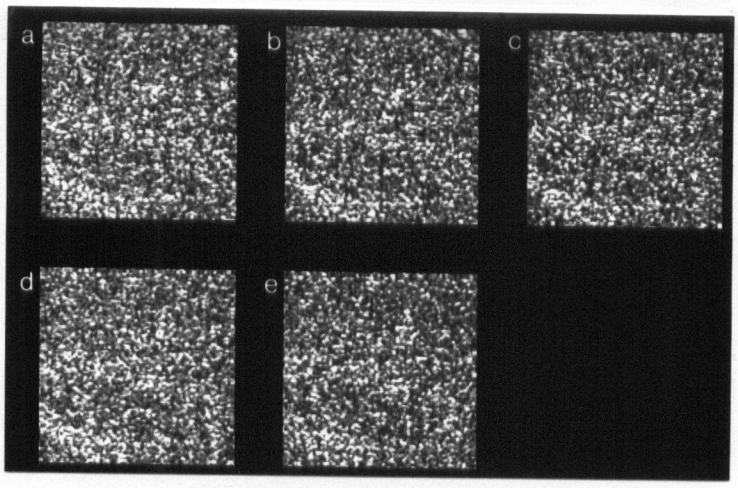

Figure 12: Goldstone subscene 2 with the five processor focus errors.
a) 0%. b) 1%, c) 2%, d) 3%, and e) 5%. The azimuthal coordinate is horizontal.

Fig. 13 corresponds to subscene 5, a high contrast mountain region. The image contrast is smoothed in this high contrast region as the processor focus error increases.

The result of the statistical testing methodology are shown in Fig. 14 and in Table VI. The case of a point target (represented by subscene 1) exhibits a high inter-look correlation of 0.714 with a peak height scaling of $M^{-0.081}$, and the image bandwidth is responding strongly, and as predicted, to the processor focus perturbations. The case of diffuse targets (represented by subscenes 2, 3, 6, and 7) exhibits an average inter-look correlation of 0.060 with a peak height scaling of $M^{-0.436}$, and the image bandwidth is insensitive to the processor focus perturbations. The remaining cases of high and low contrast imagery exhibit intermediate results for each of the extracted statistics.

The image bandwidth measure for the high contrast mountain scenes represented by subscenes 5 and 9 have a relatively low and constant image bandwidth for all processor focus settings. This is because the structure along the linear image features is being measured, rather than the bandwidth of the image speckle. Such effects are illustrated

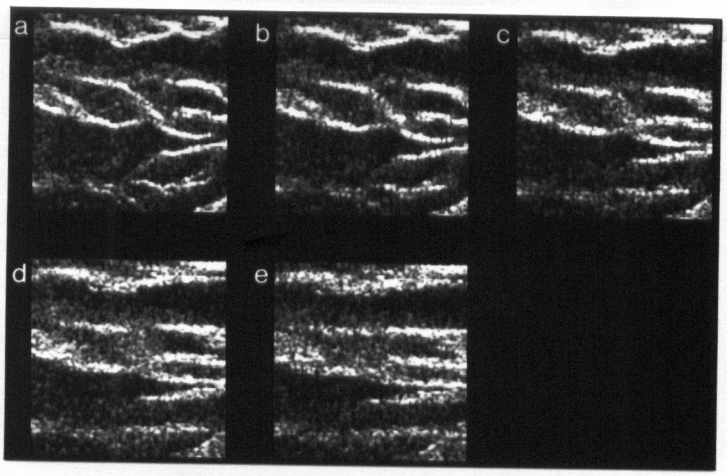

Figure 13: Goldstone subscene 5 with the five processor focus errors.
a) 0%. b) 1%, c) 2%, d) 3%, and e) 5%. The azimuthal coordinate is horizontal.

Table VI: Peak-height scaling and inter-look cross-correlation for the Goldstone subscenes.

subscene	target type	peak-height scaling	cross-correlation
1	point	-0.081	0.714
2	diffuse	-0.464	0.028
3	diffuse	-0.406	0.086
4	low contrast	-0.366	0.146
5	high contrast	-0.139	0.567
6	diffuse	-0.467	0.027
7	diffuse	-0.405	0.099
8	low contrast	-0.349	0.166
9	high contrast	-0.134	0.588
10	low contrast	-0.382	0.122

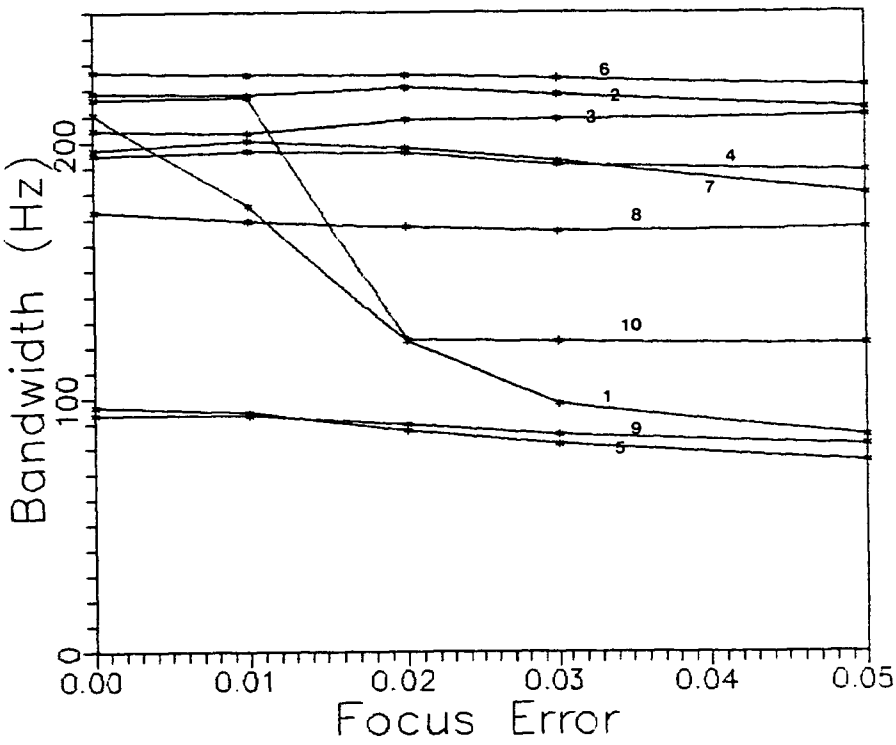

Figure 14: Image bandwidth measure for the Goldstone subscenes.

and discussed further in Appendix D in connection with imagery of linear targets and narrow "V" ship wakes.

We see that nominally point target and diffuse target cases approach their predicted behaviour for each of the extracted statistics. Note, however, that even those cases chosen as being ideal are not behaving exactly in an ideal fashion.

Having established the behaviour of SEASAT SAR/GSAR imagery to the test statistics, we will now extract these same statistics from an ocean test scene.

8.1.3 SEASAT SAR Test Scene

The test scene chosen is a region of ocean in the vicinity of Duck Island, North Carolina, taken from SEASAT orbit 1339. This data set, referred to as Duck-X, has been the subject of intense study [6,7]. Duck-X is known to contain a 200 m wave system propagating at about 45° to azimuth. The scene and extracted 128-by-128 pixel subscenes are shown in Fig. 15. The ten areas chosen for testing were extracted at random. The dominant wave system is apparent in the image.

Fig. 16 shows subscene 1 with the five processor focus errors. As the processor focus error increases, the image contrast due to the wave system is lost, as discussed further in Appendix E.

Results of the statistical testing methodology are shown in Fig. 17 and in Table VII. It is apparent that each of these regions is exhibiting the behaviour expected for nearly purely diffuse targets. This result is disappointing, but not surprising for several reasons.

First, since the spatial resolution of SEASAT is rather large, there is an ensemble of many point targets present in each subscene, and each target is subjected to the orbital dynamics of the underlying wave train. Thus, each target has different motion parameters and the observed result is an average over the ensemble of targets. In the case of the simulation and the control scene, no dynamics were involved and the focal

Figure 15: SEASAT SAR Duck-X scene showing extracted subscenes. The azimuthal coordinate is horizontal while the (slant) range is vertical.

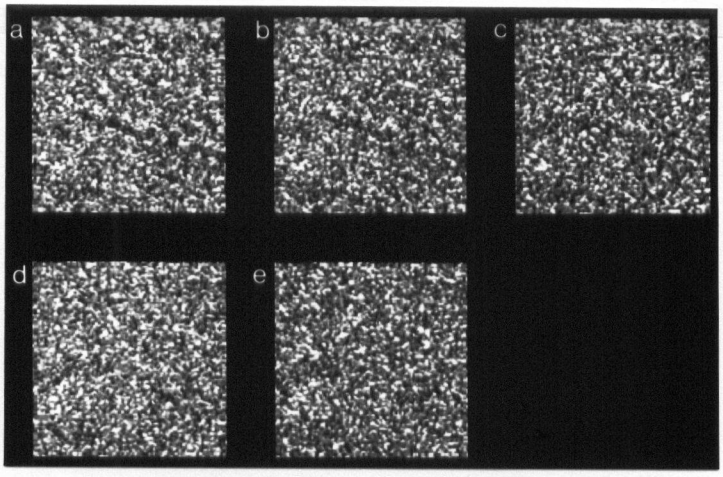

Figure 16: Duck-X subscene 1 with the five processor focus errors.
a) 0%, b) 1%, c) 2%, d) 3%, and e) 5%. The azimuthal coordinate is horizontal.

Table VII: Peak-height scaling and inter-look cross-correlation for the Duck-X subscenes.

subscene	peak-height scaling	cross-correlation
1	-0.451	0.034
2	-0.436	0.051
3	-0.445	0.045
4	-0.444	0.044
5	-0.430	0.057
6	-0.439	0.048
7	-0.435	0.053
8	-0.433	0.059
9	-0.434	0.053
10	-0.392	0.108

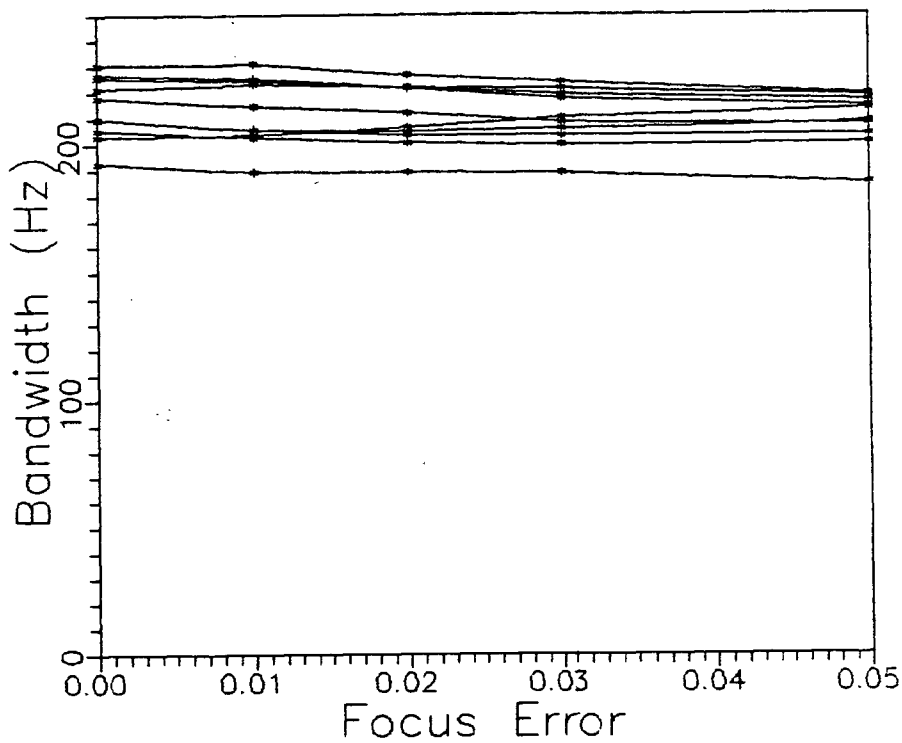

Figure 17: Image bandwidth measure for the Duck-X subscenes.

properties of the targets were systematic and identical.

Second, but perhaps of less importance, the targets in the ocean scene could be subject to coherence time limitations, and hence be rather broad. This would soften any predominant peaks due to underlying specular processes. This makes the scene appear to be more diffuse in nature, even if the target density were rather low.

The principle difficulty with this experiment has been the rather poor signal-to-noise ratio. An individual target cannot be tracked as the focus is perturbed for the test scene, in contrast to the control Goldstone corner reflector array. In order to fully test the coherent Bragg cell hypothesis, we would like an ensemble of Bragg targets with a relatively long coherence time and a high signal-to-noise ratio. The image of a narrow "V" ship wake provides such an opportunity.

8.2 Linear Targets and Narrow "V" Ship Wakes

As discussed previously, the narrow "V" ship wake presents an opportunity to explicitly observe an ensemble of Bragg scatterers. In this section, we discuss simulations of linear arrays of point targets, the resulting statistical measures, and draw qualitative comparisons with actual SAR imagery of narrow "V" ship wakes.

8.2.1 SEASAT SAR Simulations

SEASAT SAR scenes were simulated with various types of linear target features and with various processor focus errors. The test statistics were extracted from the results. Details of the analysis are contained in Appendix B. It is demonstrated that a large relative cross-section is required to differentiate the linear target from a nominally diffuse background, and that the best sensitivity to the processor focus test is achieved by a linear target oriented perpendicular to the SAR channel in which the processor focus is perturbed. This is the range channel for narrow "V" ship wakes—a SAR image phenomena which seems exclusively associated with near azimuthally travelling ships.

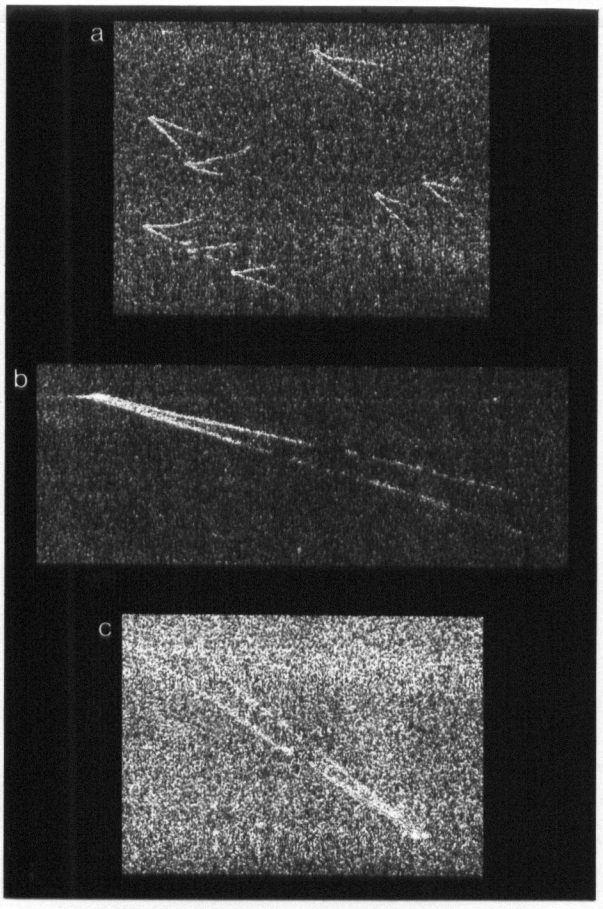

Figure 18: Examples of ship wakes in SEASAT SAR imagery.

8.2.2 SEASAT SAR Ship Wake Imagery

Fig. 18 shows SEASAT SAR imagery of several examples of ship wakes taken from a scene in the Irish Sea. Two types of wakes are apparent in this figure: first, the fishing fleet in the top image produces wakes with relatively large opening angles; and second, the ships in the middle and lower images produce narrow "V" wakes. The lines associated with these wakes are very similar to the linear targets simulated in Appendix B. Unfortunately, this imagery was not available in a form suitable for the

prescribed statistical testing. We may only assert that in the event of a change in the range channel processor focus error, the range impulse response will be broadened and the wake image will be smeared as was shown to be the case with the simulated linear target features. This, in itself, would suggest that the scattering from these Bragg scale waves is coherent in nature and that the proposed model for Bragg scattering is suitable.

The fact that ship-generated Bragg scale waves scatter microwaves in a coherent manner suggests that Bragg scattering, in general, is a coherent process. This may be a difficult assertion to defend because typical ocean surface Bragg scale structure is not as well organized as the waves produced by the passage of a ship. However, all ocean surface roughness or waves of the Bragg scale must obey the same dispersion relation, and so, must be of the same inherent nature within the narrow band observed by the radar. Differences between the general ocean roughness case and the ship wake case lie with the associated coherence time scale rather than in a different scattering process with a different inherent nature. This was demonstrated with the Duck-X ocean test scene.

8.3 Scene Coherence Time

We now turn to a very different dynamic phenomenon: scenes of ocean waves propagating from the open ocean into a region covered by floating ice floes as observed by an airborne SAR. The actual SAR data was obtained during the LEWEX experiment [15] by the CCRS C-SAR digital SAR [40]. The waves in ice imagery presents the same dynamics as in the open water case, but the coherence time has been effectively increased through the suppression of the high frequency wave components. This subtle but important point deserves emphasis: with floating ice, the targets are, in effect, permanently present—the issues of Bragg scattering and coherence time are removed. We are left with a pure experimental representation of a velocity bunching model.

Two actual SAR images were chosen for this comparison: first, a scene showing ocean waves propagating near and towards an ice edge; and second, a scene showing the waves propagating through the ice. These two scenes were obtained within 30 seconds of each other. The ice and ocean images are shown on the upper-left and lower-left of Fig. 19 respectively. The corresponding two-dimensional Fourier transforms are shown in similar positions in Fig. 20. The image transforms have been smoothed using a Gaussian kernel, and circles of constant wavelength are indicated.

The image transforms of Fig. 20 indicate a rather interesting situation. We see that the same dominant wave component is present (labeled A1) in both the ice and ocean cases (*i.e.* $\Lambda \approx 150$ m, $\phi \approx 45°$). In the ice case, the second harmonic is also apparent (A2), indicating that the wave image is rather cusped in this case. In the ocean case, the cusped nature of the response is smoothed by the effects of the finite scene coherence time, and the second harmonic is not readily apparent. Furthermore, it is apparent that in the ice case there is an additional wave component present which corresponds to a shorter, more azimuthally travelling wave (B1). There is no evidence for the corresponding wave in the ocean case. Thus, based upon the ice image, the ocean has a bimodal wave system present and the corresponding images are cusped in nature due to velocity bunching. However, due to the smoothing effect of the finite scene coherence time, the ocean image appears relatively smooth and unimodal.

Simulations were performed in order to observe the effect of the coherence time upon the principal wave component and to draw comparisons with the actual SAR imagery. The simulation parameters chosen correspond to a monochromatic azimuthally travelling wave ($\phi = 0°$) with a 150 m wavelength, $\alpha = 1/2.5\pi$ (sharply cusped, but not double peaked), and coherence times of $\tau \gg T$, $\tau = 47$ msec, and $\tau = 14$ msec. The simulation results are presented on the right of Fig. 19 arranged from top-to-bottom with decreasing coherence time. The corresponding Fourier transforms are shown in Fig. 20. As the coherence time decreases, we move from a very cusped image with three

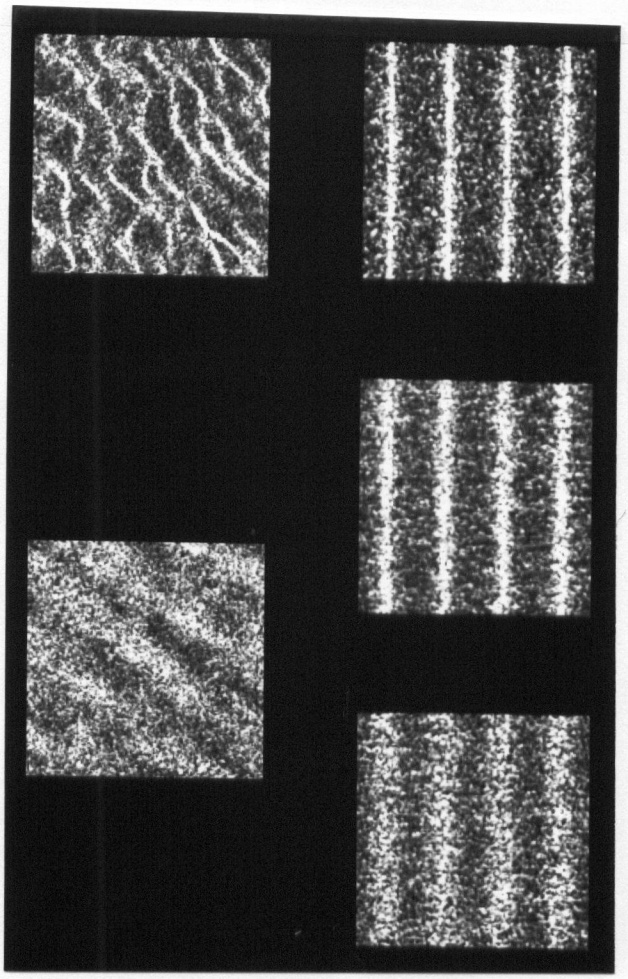

Figure 19: Comparison of C-SAR with simulation (coherence time).
The C-SAR imagery is of waves in ice (upper-left) and of waves in the open ocean (lower-left). The simulated imagery corresponds to a 150 m wave with $\alpha = 1/2.5\pi$ having coherence times of $\tau \gg T$ (upper-right), $\tau = 47$ msec (middle-right), and $\tau = 14$ msec (lower-right).

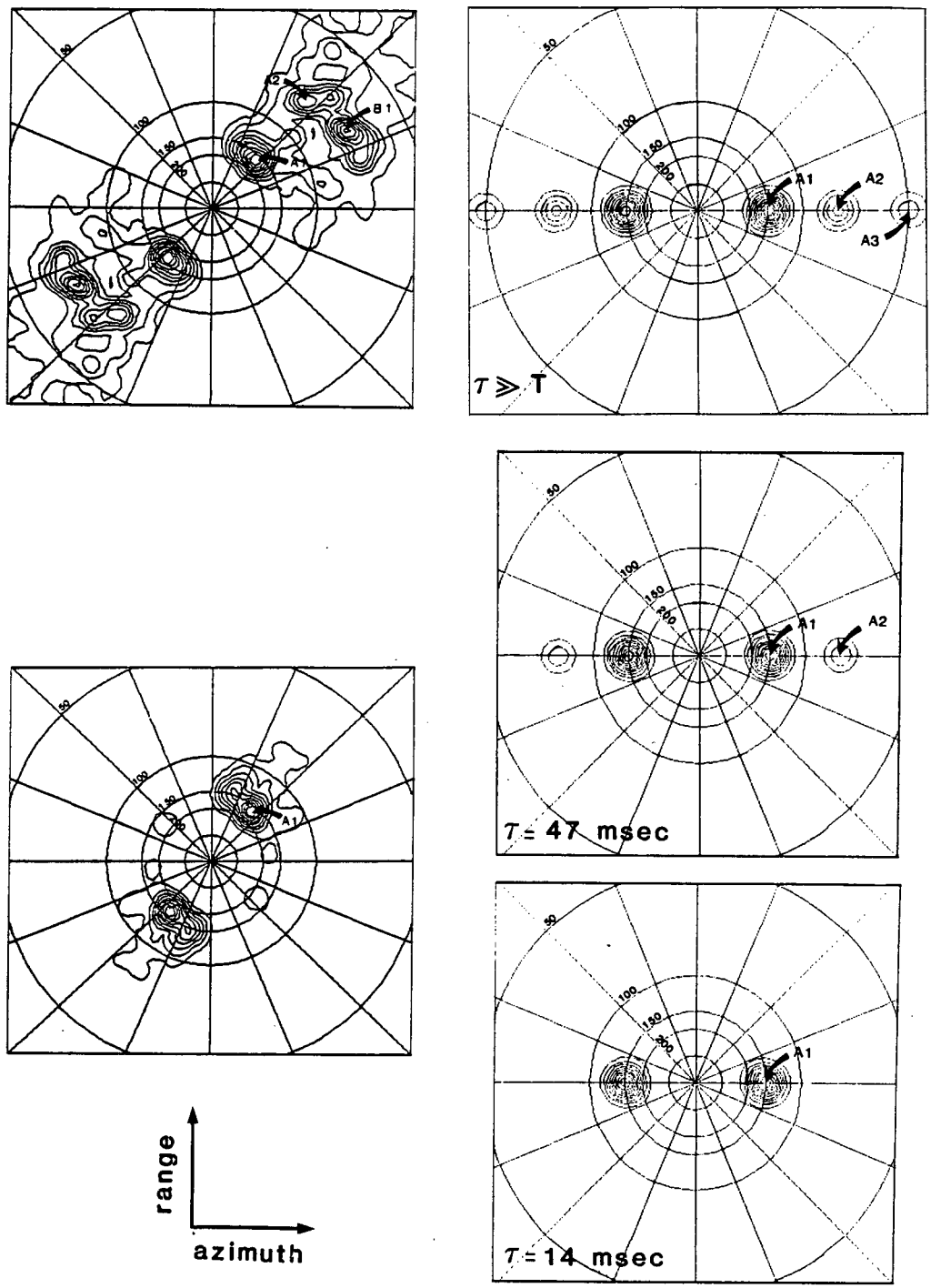

Figure 20: C-SAR and simulation image Fourier transforms. The transforms correspond to the images shown in Fig. 19.

Table VIII: Contrast measures for one- and two-dimensional C-SAR simulations.

$T/N\tau$	τ (msec)	C_{1-d}	C_{2-d}
~ 0	$\gg T$	3.199	2.786
3	47	1.887	1.521
10	14	0.673	0.652

harmonics visible (upper-right A1, A2, A3) to a smooth image with only one harmonic visible (lower-right A1).

It is apparent that the cases of $\tau \gg T$ (no coherence time limitation) and $\tau =$ 14 msec (coherence time limited) are similar in both appearance and in Fourier transform nature to the C-SAR images of waves in ice and waves in the ocean respectively. This suggests that a coherence time on the order of 14 msec is appropriate for C-band airborne SAR imagery of the ocean surface. This estimate is more than an order of magnitude smaller than some of the coherence times calculated based upon decorrelation time scales in Chapter 5. Simulation verifies that coherence time is not a limiting parameter for the images of the same waves moving through ice.

The smoothing of the cusped image nature in the ocean case is enhanced by the looks becoming misregistered due to noncoherent reflectivity envelope translation. However, the scenes chosen were at near range so that the R/V parameter is as small as possible and the misregistration is minimized. This effect is discussed further in the following Section.

Table VIII lists contrast measures for the simulations in Fig. 19 and the one-dimensional simulations of Appendix D. The two-dimensional simulation contrast measures were obtained by integrating the simulation in range to produce the results shown in Fig. 21. The contrast is measured as in Appendix D. In each case, the contrast is comparable between the one- and two-dimensional simulations for each simulated coherence time. Recalling that the target density used in performing the two-dimensional

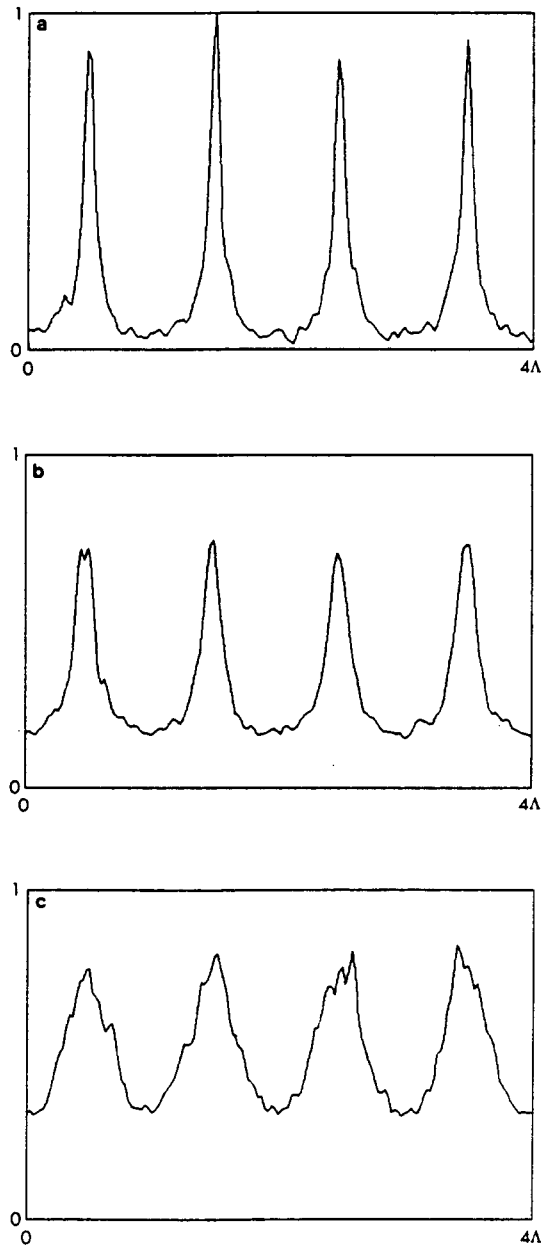

Figure 21: Range integrated two-dimensional simulations for the three coherence times considered.

simulation is rather small, the approach to obtaining this comparison and relating the two-dimensional simulation to the one-dimensional simulation (and to most other SAR ocean simulations) shows how the assumption of diffuse scattering and a large degree of spatial averaging can be misleading.

8.4 Translating Reflectivity Patterns

As discussed in earlier chapters, the SAR image of an ocean wave field constitutes the imaging of a translating pattern of microwave reflectivity which is made up of many independent point targets, each with its own dynamic properties. SAR imagery of waves in ice presents an ideal opportunity to observe the effect of the translating reflectivity pattern because coherence time limitations are not an issue for ice imagery.

Each look is imaged at a different azimuth time. Also, the available coherent integration time is range dependent. Thus, we expect the relative misregistration between looks to increase for an ocean wave with an azimuthal wavenumber component. We expect to see a general loss in wave contrast at the far range compared with the near range. This effect should be particularly pronounced for the ice-covered case versus the open ocean case due to the absence of a coherence time limitation, and the resultant sharply peaked response functions for certain wave conditions [3,64,77].

C-SAR imagery of waves in ice with an azimuthal wavenumber component was compared with two-dimensional simulated imagery of waves with a large coherence time. The results are presented in Fig. 22. The figure shows the cases of near, mid-, and far range. Note that as the range increases, so does the degree of smear associated with the wave crests. The same effect is present in the ocean scene, but it is masked to a large degree by the finite scene coherence time. The upper-right hand image represents the multi-look image in the absence of noncoherent target motions. In principle, the images corresponding to the near, mid-, and far range cases presented in the figure can have their individual looks re-registered to produce the pattern with the sharpest

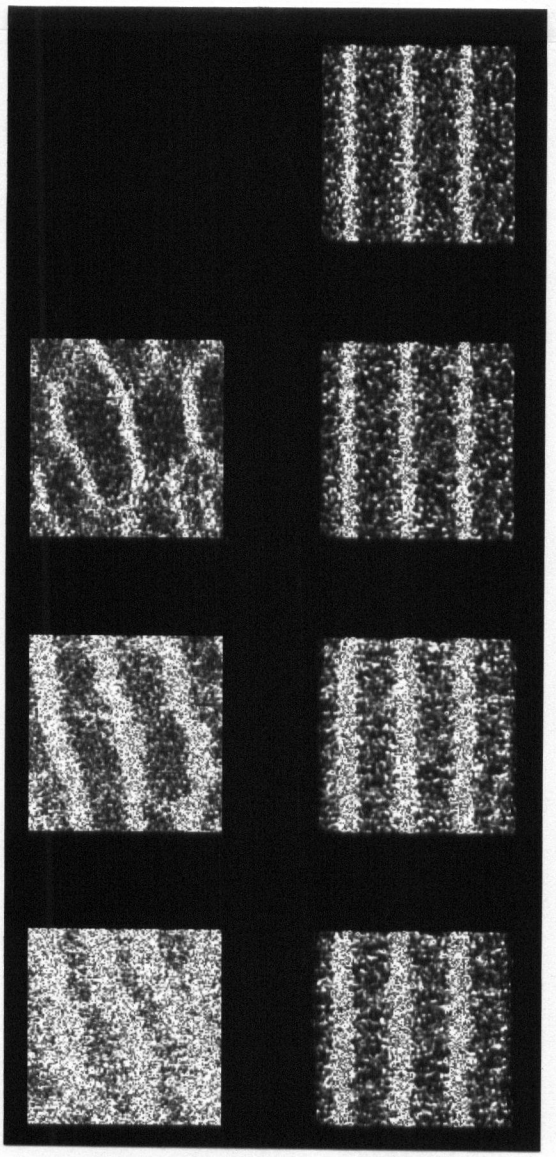

Figure 22: Comparison of C-SAR with simulation (envelope translation).
The comparisons are at near range (top), mid-range, and far range (bottom). The wave parameters are $\Lambda = 150$ m and $\alpha = 1/2.5\pi$.

contrast shown in the upper-right. If the re-registration is made by adjusting the processor focus setting, the contrast, although improved, will be degraded from that which appears in the upper-right image.

8.5 Summary

This Chapter has presented qualitative and quantitative comparisons between simulated and actual SAR imagery. Comparisons were made to address the Bragg scattering nature, the narrow "V" ship wake, the scene coherence time, and the role of the translating reflectivity pattern.

The extraction of key statistics from simulated imagery of varying target density has demonstrated that convergence to diffuse scattering statistics is rather slow. The extraction of the same statistics from SEASAT SAR imagery demonstrates the appropriate behaviour for point and diffuse targets in the test scene, but indicates that the ocean scene is diffuse in nature. This result probably arises due to the diversity of targets over the SEASAT resolution cell in the ocean scene. On the basis of image appearance alone, relatively small target densities will produce simulated ocean scenes which compare favorably with actual SAR ocean surface imagery, as has been verified with high resolution airborne SAR imagery.

One arm of a narrow "V" ship wake was simulated as a linear target consisting of a line of discrete point targets in Appendix B. This model results in imagery which compares favorably with actual SAR ship wake imagery. The required testing procedure has been specified. The results indicate a specular-like scattering for this linear feature. As the processor focus is varied, the impulse response is broadened. Thus, it is expected that the linear features associated with the narrow "V" ship wake will be correspondingly broadened. This is the focus dependence expected for an isolated specular-like target.

Scenes containing ocean waves with various mean target coherence times were simu-

lated and compared with actual SAR imagery of surface gravity waves in an ice-covered region and in the open ocean. Comparison between the ice imagery and simulations with long coherence times is favorable, as is comparison between the open ocean imagery and simulations with a coherence time of about 14 msec. This time is considerably shorter than the decorrelation time scales estimated in Chapter 5 and those conventionally assumed in the relevant literature.

The translation of the reflectivity envelope at the wave phase velocity was demonstrated by comparing ice imagery at near, mid-, and far range with simulated imagery having appropriately misregistered looks. The misregistration is range dependent because the available coherent integration time is range dependent, as is the degree of look misregistration. Look re-registration confirms the results predicted in this work. These comparisons confirm the role of the translating reflectivity envelope.

9 Conclusions

In this thesis, current SAR theory for imaging of the ocean surface has been re-derived and extended. As well, simulated and actual SAR imagery has been compared to address three key issues in SAR ocean surface imaging.

The first issue examines the coherent versus noncoherent nature of Bragg scattering. While the Bragg scattering phenomenon is traditionally dismissed as being a diffuse scattering process, this work defends the assertion that Bragg scattering is a coherent, specular-like process, although experimental statistical tests designed to address this point were inconclusive for the available SEASAT SAR test scene. A case with a more advantageous signal-to-noise ratio is required by the analysis methodology. The narrow "V" ship wake often seen in SAR imagery of azimuthally travelling ships presents such a case. The required analysis has been described.

The second issue is the magnitude, role, and calculation of the scene coherence time. Comparisons between simulated and actual SAR imagery has suggested a coherence time on the order of 14 msec is appropriate for the LEWEX ocean scene observed by an airborne C-band SAR. This result is more than an order of magnitude smaller than some estimates based upon conventional decorrelation time models and an idealized ocean surface wave spectrum. Furthermore, some of the theoretical estimates seem independent of both seastate and ambient environmental conditions—a situation which seems unlikely. It was shown that considerably longer coherence times are required for imaging by a satellite SAR. Only very highly organized ocean surface structure, such as a swell system, should be imaged at all by a satellite SAR.

The third issue is the role of the wave phase velocity and orbital velocity. It has been shown that coherent Doppler modulations by the long wave orbital velocity leads to velocity bunching, which is a well known phenomenon. Velocity bunching simulations in this work compare favorably with actual SAR imagery of waves in an ice-covered region—a situation in which coherence time limitations are not an issue. It was also

demonstrated that the phase velocity can only manifest itself as the translation velocity of the mean reflectivity envelope. This envelope will cause noncoherent effects in the SAR image, such as look misregistrations and scanning distortions, if the ratio C_p/V is sufficiently large.

The conclusions of this work rely heavily upon semi-quantitative comparisons drawn between actual and simulated SAR imagery. The simulation is based upon a SAR ocean scattering model which includes velocity bunching (coherent orbital velocity Doppler modulations) and a reflectivity envelope which translates at the wave phase velocity. The simulation is also unique in that explicit account is taken of each target which constitutes the scene. Simulation of ocean surface phenomena with relatively small target densities compare favorably with actual SAR ocean imagery. This fact strengthens the claim that Bragg scattering is a coherent phenomenon for each Bragg scattering region.

The work presented in this thesis makes progress in understanding the underlying physical phenomena, and in defusing controversies surrounding three dominant issues in SAR ocean surface imagery. The work on these issues is by no means complete. However, the importance of target density, scene coherence time, and coherent/noncoherent scene velocities have been demonstrated in this work. The results provide new insights into the very complex issues involved, and should aid in improving the design and performance of imaging radar systems intended to faithfully observe global ocean resources.

Glossary

along-track velocity The target velocity component parallel to the direction of platform motion.

azimuth The SAR (image) dimension which is parallel to the platform velocity vector.

Bragg scattering Diffracted beams of electromagnetic radiation resulting from constructive interference of coherent radiation homogeneously scattered from a regular lattice of targets. In the radar/ocean case, the radar wavelength and angle of incidence select the lattice, or ocean wavelength scale, which dominates the scattering. For the SEASAT SAR, the Bragg wavelength is of order 30 cm, while for the C-SAR, the Bragg wavelength is of order 5 cm.

C-Band Microwave frequency band with wavelength of order 5 cm.

CCRS Canada Centre for Remote Sensing.

C-SAR The CCRS C-band digital SAR and real-time processor on the CCRS Convair 580 aircraft.

Capillary wave A wave whose restoring force is dominated by surface tension. Capillary waves generally satisfy $\Lambda \ll 1.73$ cm.

coherence time-bandwidth product A measure of the degree of coherent processing which a partially coherent signal will support.

coherent A property implying that the phase is of relevance. A coherent signal has a deterministic phase function.

coherent integration time The time over which a target is coherently observed by the radar. This is equal to the time spent within the antenna pattern.

coherent modulation Modulation in which the signal phase is preserved or modified.

depth of focus The error in target range which still allows reasonable focussing properties. Generally, one depth of focus corresponds to the focus error $\eta = 2N/TB$.

dispersion relation The relationship between wave frequency and wavenumber.

Doppler bandwidth The Doppler frequency range due to the target moving through the antenna pattern.

Doppler frequency The frequency shift $2v/\lambda$ resulting from reflection from a target moving with radial velocity v.

Doppler suppression The loss of target signal due to shifts outside of the system bandwidth resulting from Doppler frequency shifts.

FFT Fast Fourier transform.

focus error The perturbation of the processor focus setting from nominally perfect focus.

HH Horizontal transmit, horizontal receive polarization.

JPL Jet Propulsion Laboratory, Pasadena, California, USA.

GSAR Generalized SAR processor. The digital SAR processor developed by MDA.

L-Band Microwave frequency band with wavelength of order 30 cm.

LEWEX Labrador Extreme Waves Experiment. Took place in conjunction with LIMEX in March 1987 off the coast of Newfoundland in the Labrador Sea.

LIMEX Labrador Ice Margin Experiment. See Lewex.

look May be defined in two senses: first, a physical look is the SAR image resulting from applying a data window to extract a portion of the Doppler spectrum; and second, a statistical look is a statistical measure, usually the MSVR, which is equivalent to the number of effective statistically independent physical looks.

MDA MacDonald Dettwiler and Associates, Richmond, B.C., Canada.

MSVR Mean-squared-to-variance ratio, a measure of radiometric resolution. For Gaussian signals, MSVR is a measure of the statistical independence of the data sources.

multi-look An image formed from more than one statistically independent look.

noncoherent A property implying that the phase is irrelevant. A noncoherent signal has random or undefined phase.

orbital velocity The speed and direction of travel of a particle or packet of water on the ocean surface as a result of the passage of a wave.

partially coherent A property implying the presence of both a coherent and noncoherent component.

phase velocity The speed and direction of travel of a point of constant phase on the surface of a wave.

RAE Royal Aircraft Establishment, Farnborough, Hampshire, UK.

RMS Root-mean-square averaging operation.

radial acceleration The target acceleration component away from the radar.

radial velocity The target velocity component away from the radar.

radiometric resolution The expected variation of the radar cross-section for each pixel. This is often expressed as the MSVR.

range The SAR (image) dimension which is perpendicular to the platform velocity vector. This coordinate is naturally the slant-range, along the radar line-of-sight, but may be converted to ground-range via interpolation.

SEASAT A US ocean remote sensing satellite which orbited the earth for approximately 100 days from July to October in 1978.

STF The system transfer function which is proportional to the Fourier transform of the static target, perfect focus impulse response.

significant waveheight May be defined in many ways, but here, we choose four time the rms waveheight.

single-look of a multi-look set The result of compressing and detecting only a portion of the available Doppler spectrum.

speckle The grainy multiplicative noise phenomenon found in all coherently produced imagery of diffuse targets.

surface gravity wave A wave whose restoring force is dominated by gravity. Surface gravity waves generally satisfy $\Lambda \gg 1.73$ cm.

swell A highly organized (generally long) surface gravity wave which has propagated away from its point of generation.

time-bandwidth product A measure of signal complexity which indicates the degree of coherent processing which a fully coherent signal will support, and the degree of improvement in resolution as a result of such processing.

VV Vertical transmit, vertical receive polarization.

velocity bunching The concentration of dispersed targets in a SAR image due to spatially variable radial velocity components.

wave frequency $\Omega = 2\pi/T_w$.

wavenumber $K = 2\pi/\Lambda$.

wind-waves A system of ocean waves resulting from local wind generation.

References

[1] Alpers, W.R., 1983; "Monte Carlo Simulations for Studying the Relationship Between Ocean Wave and Synthetic Aperture Radar Image Spectra," *J. Geophys. Res., 88 (C9)*, pp 1745–1759.

[2] Alpers, W.R., and C. Bruening, 1986; "On the Relative Importance of Motion-Related Contributions to the SAR Imaging Mechanism of Ocean Surface Waves," *IEEE Trans. Geoscience Rem. Sens., GE-24 (6)*, pp 873–885.

[3] Alpers, W.R., D.B. Ross, and C.L. Rufenach, 1981; "On the Detectibility of Ocean Surface Waves by Real and Synthetic Aperture Radars," *J. Geophys. Res., 86 (C7)*, pp 6481–6498.

[4] Alpers, W.R., and C.L. Rufenach, 1979; "The Effect of Orbital Motions on Synthetic Aperture Radar Imagery of Ocean Waves," *IEEE Trans. Antennas Propagat., AP-27 (5)*, pp 685–690.

[5] Beal, R.C., P.S. DeLeonibus, and I. Katz Ed., 1981; *Spaceborne Synthetic Aperture Radar for Oceanography*, The Johns Hopkins University Press, Baltimore, 215p.

[6] Beal, R.C., D.G. Tilley, and F.M. Monaldo, 1983; "Large- and Small-Scale Spatial Evolution of Digitally Processed Ocean Wave Spectra From SEASAT Synthetic Aperture Radar," *J. Geophys. Res., 88 (C9)*, pp 1761–1778.

[7] Beal, R.C., T.W. Gerling, D.E. Irvine, F.M. Monaldo, and D.G. Tilley, 1986; "Spatial Variations of Ocean Wave Directional Spectra From the Seasat Synthetic Aperture Radar," *J. Geophys. Res., 91 (C2)*, pp 2433–2449.

[8] Beal, R.C., F.M. Monaldo, D.G. Tilley, D.E. Irvine, E.J. Walsh, F.C. Jackson, D.W. Hancock III, D.E. Hines, R.N. Swift, F.I. Gonzalez, D.R. Lyzenga, and L.F. Zambresky, 1986; "A Comparison of SIR-B Directional Ocean Wave Spectra with Aircraft Scanning Radar Spectra," *Science, 232*, pp 1531–1535.

[9] Bennett, J.R., and I.G. Cumming, 1978; "Digital Techniques for the Multi-Look Processing of SAR Data with Application to SEASAT-A," 5^{th} *Canadian Symposium on Remote Sensing*, Victoria, pp 506–516.

[10] Bennett, J.R., and P.R. McConnell, 1980; "Considerations in the Design of Multilook Processors for Image Quality," *Proc.* 3^{rd} *SEASAT-SAR Workshop on 'SAR Image Quality,'* Held at Frascati, Italy, 11–12 Dec., 1980, pp 5–12.

[11] Brown, W.M., 1967; "Synthetic Aperture Radar," *IEEE Trans. Aerospace Electron. Syst., AES-3 (2)*, pp 217–229.

[12] Brown, W.M., and C.J. Palermo, 1962; "Theory of Coherent Systems," *IRE Trans. Military Electronics*, pp 187–196.

[13] Brown, W.M., and C.J. Palermo, 1962; "System Performance in the Presence of Stochastic Delays," *IRE Trans. Inform. Theory, IT-8 (5)*, pp s206–s214.

[14] Dawe, B.R., and S.K. Parashar, 1978; "SAR Imaging of Waves in Ice," *Oceans '78* 4^{th} *Ann. Combined Conf.*, Washington DC, Sept 6–8, 1978, pp 379–384.

[15] Freeman, N.G., P.W. Vachon, and C.E. Livingstone, 1986; "Airborne SAR imaging of Azimuthally Travelling Ocean Surface Waves: The LEWEX Experimental Plan," *Proc. IGARSS '87 Symposium*, Ann Arbor, May 19–21, 1987, pp 1393–1398.

[16] Garrett, C., and J. Smith, 1976; "On the Interaction between Long and Short Surface Waves," *J. Physical Oceanography, 6*, pp 925–980.

[17] Goldfinger, A.D.; "Estimation of Spectra from Speckled Images," *IEEE Trans. Aerospace Electron. Syst., AES-18 (5)*, pp 675–681.

[18] Goodman, J.W., 1968; *Introduction to Fourier Optics*, McGraw-Hill, New York, 287p.

[19] Harger, R.O., 1970; *Synthetic Aperture Radar Systems; Theory and Design*, Academic Press, New York, 240p.

[20] Harger, R.O., 1981; "SAR Ocean Imaging Mechanisms," in Beal *et al*, pp 41–52.

[21] Hartl, Ph., A. Popella, and A.J. Sieber, 1985; "SAR Product Simulation," *Proc. Workshop on Thematic Applications of SAR Data*, Frascati, Italy, Sept. 1985 (ESA SP–257), pp 65-72.

[22] Hasselmann, K, T.P. Barnett, E. Bouws, H. Carlson, D.E. Cartwright, K. Enke, J.A. Ewing, H. Glennop, D.E. Hasselmann, P. Kruseman, A. Meerburg, P. Müller, D.J. Olbers, K. Richter, W. Sell, and H. Walden, 1973; "Measurements of Wind-Wave Growth and Swell Decay During the Joint North Sea Wave Project (JONSWAP)," *Deut. Hydrogr. Z., Suppl. A. Nr. 12.*.

[23] Hasselmann, K., R.K. Raney, W.J. Plant, W. Alpers, R.A. Shuchman, D.R. Lyzenga, C.L. Rufenach, and M.J. Tucker, 1985; "Theory of SAR Ocean Wave Imaging: A MARSEN View," *J. Geophys. Res., 90 (C3)*, pp 4659–4686.

[24] Holtzman, J.C., V.S. Frost, J.L. Abott, and V.H. Kaupp, 1978; "Radar Image Simulation," *IEEE Trans. Geoscience Elect., GE-16 (4)*, pp 296–303.

[25] Ivanov, A.V., 1982; "On the Synthetic Aperture Radar Imagery of Ocean Surface Waves," *IEEE J. Oceanic Eng., OE-7 (2)*, pp 96–103.

[26] Jain, A., 1978; "Focussing Effects in Synthetic Aperture Radar Imagery of Ocean Waves," *Appl. Phys., 15*, pp 323–333.

[27] Jain, A., 1981; "SAR Imaging of Ocean Waves: Theory," *IEEE J. Oceanic Eng., OE-6 (4)*, pp 130–139.

[28] Jain, A. and O.H. Shemdin, 1983; "L Band SAR Ocean Wave Observations During Marsen," *J. Geophys. Res., 88 (C14)*, pp 9792–9808.

[29] Jakeman, E., 1980; "Speckle Statistics with a Small Number of Scatterers," *SPIE Vol. 243 Applications of Speckle Phenomena*, pp 9–19.

[30] Jakeman, E., and P.N. Pusey, 1976; "A Model for Non-Rayleigh Sea Echo," *IEEE Trans. Antennas Propagat., AP-24 (6)*, pp 806–814.

[31] Jakeman, E., and P.N. Pusey, 1977; "Statistics of Non-Rayleigh Microwave Sea Echo," *Proc. RADAR '77 Int. Conf.*, pp 105–109.

[32] Jakeman, E., and P.N. Pusey, 1978; "Significance of K Distributions in Scattering Experiments," *Phys. Rev. Let., 40 (9)*, pp 546–550.

[33] Jordan, R.L., 1980; "The Seasat-A Synthetic Aperture Radar System," *IEEE J. Oceanic Eng., OE-5 (2)*, pp 154–164.

[34] Kerr, D.E., 1951; *Propagation of Short Radio Waves*, McGraw Hill, New York.

[35] Klauder, J.R., A.C. Price, S. Darlington, and W.J. Albersheim, 1960; "The Theory and Design of Chirp Radars," *Bell Syst. Tech. J., 39*, pp 745-808.

[36] Lamb, H., 1932; *Hydrodynamics* 6^{th} ed., Dover Publications, New York, 738 pp.

[37] Larson, T.R., L.I. Moskowitz, and J.W. Wright, 1976; "A Note on SAR Imagery of the Ocean," *IEEE Trans. Antennas Propagat., AP-24*, pp 393–394.

[38] LeBlond, P.H.,and L.A. Mysak, 1978; *Waves in the Ocean*, Elsevier, Amsterdam, 602p.

[39] Li, F.-K., D.N. Held, J.C. Curlander, and C. Wu, 1985; "Doppler Parameter Estimation for Spaceborne Synthetic-Aperture Radars," *IEEE Trans. Geoscience Rem. Sens., GE-23 (1)*, pp 47–56.

[40] Livingstone, C.E., A.L. Gray, R.K. Hawkins, J.G. Halbertsma, R.A. Deane, and R.B. Olsen, 1987; "CCRS C-band Airborne Radar—System Description and Test Results", submitted to 11^{th} *Canadian Symposium on Remote Sensing*, Waterloo, Ontario, June 22–25.

[41] Lyden, J.D., 1985; *Analysis of SEASAT Revolution 407 Ship Wake Data*, ERIM Topic Report 155900–32–T, 17p.

[42] Lyden, J.D., R.R. Hammond, and D.R. Lyzenga, 1987; "Synthetic Aperture Radar Detection of Surface Ship Wakes," submitted to *J. Geophys. Res.*.

[43] Lyzenga, D.R., 1986; "Numerical Simulation of Synthetic Aperture Radar Image Spectra for Ocean Waves," *IEEE Trans. Geoscience Rem. Sens., GE-24 (6)*, pp 863–872.

[44] Lyzenga, D.R., A.L. Maffett, and R.A. Shuchman, 1983; "The Contribution of Wedge Scattering to the Radar Cross Section of the Ocean Surface," *IEEE Trans. Geoscience Rem. Sens., GE-21 (4)*, pp 502–505.

[45] Monaldo, F.M., 1984; "Improvement in the Estimation of Dominate Wavenumber and Direction from Spaceborne SAR Image Spectra when Corrected for Ocean Surface Movement," *IEEE Trans. Geoscience Rem. Sens., GE-22 (6)*, pp 603–608.

[46] Monaldo, F.M. and D.R. Lyzenga, 1986; "On the Estimation of Wave Slope- and Height-Variance Spectra from SAR Imagery," *IEEE Trans. Geoscience Rem. Sens., GE-24 (4)*, pp 543–551.

[47] Moore, R.K., 1985; "Radar Sensing of the Ocean," *IEEE J. Oceanic Eng., OE-10 (2)*, pp 84–112.

[48] Neuman, G. and W.J. Pierson Jr., 1966; *Principles of Physical Oceanography*, Prentice-Hall, London, 545 p.

[49] North, D.O., 1943; "Analysis of the Factors Which Determine Signal/Noise Discrimination in Pulsed-Carrier Systems," *RCA Lab. Rept. PTR-6C*; reprinted in *Proc. IEEE, 51 (7)*, pp 1015–1027.

[50] Ouchi, K., 1986; "Multi-look Processing of Synthetic Aperture Radar Data from Dynamic Ocean Surfaces," *Pattern Recognition Letters, 4*, pp 305–314.

[51] Palermo, C.J., 1963; *Theory of Stochastic Delays*, Rep. 2900-383-T Institute of Science and Technology, University of Michigan, Ann Arbor (Also available from University Microfilm Inc., Ann Arbor, Michigan, Document 64–868) 83p.

[52] Papoulis, A., 1965; *Probability, Random Variables, and Stochastic Processes*, McGraw–Hill Book Co., New York, 583p.

[53] Phillips, O.M., 1980; *The Dynamics of the Upper Ocean* 2^{nd} ed., Cambridge University Press, 326p.

[54] Phillips, O.M., 1981; "The Structure of Short Gravity Waves on the Ocean Surface," in Beal *et al*, pp 24–31.

[55] Pierson, W.J., and L.I. Moskowitz, 1964; "A Proposed Spectral Form for Fully Developed Wind Seas Based on the Similarity Theory of S.A. Kitaigorodskii," *J. Geophys. Res., 69 (24)*, pp 5181-5190.

[56] Plant, W.J. and W.C. Keller, 1983; "The Two-Scale Radar Wave Probe and SAR Imagery of the Ocean," *J. Geophys. Res., 88 (C14)*, pp 9776–9784.

[57] Pond, S. and G.L. Pickard, 1983; *Introductory Dynamical Oceanography*, 2^{nd} ed., Pergamon Press, Oxford, 329 p.

[58] Porcello, L.J., N.G. Masey, R.B. Innes, and J.M. Marks, 1976; "Speckle Reduction in Synthetic Aperture Radars," *J. Opt. Soc. Amer., 66 (11)*, pp 1305–1311.

[59] Pravdo, S.H., B. Huneycutt, B.M. Holt, and D.N. Held, 1983; *Seasat Synthetic-Aperture Radar Data User's Manual*, JPL Publication 82–90.

[60] Raney, R.K., 1971; "Synthetic Aperture Radar Imaging and Moving Targets," *IEEE Trans. Aerospace Electron. Syst., AES-7 (3)*, pp 499–505.

[61] Raney, R.K., 1980; "SAR Response to Partially Coherent Phenomena," *IEEE Trans. Antennas Propagat., AP-28 (6)*, pp 777–787.

[62] Raney, R.K., 1981; "Wave Orbital Velocity, Fade, and SAR Response to Azimuth Waves," *IEEE J. Oceanic Eng., OE-6 (4)*, pp 140–146.

[63] Raney, R.K., 1983; "Transfer Functions for Partially Coherent SAR Systems," *IEEE Trans. Aerospace Electron. Syst., AES-19 (5)*, pp 740–750.

[64] Raney, R.K., 1985; "Theory and Measure of Certain Image Norms in SAR," *IEEE Trans. Geoscience Rem. Sens., GE-23 (3)*, pp 343–348.

[65] Raney, R.K., 1986; "Doppler Properties of Radars in Circular Orbits," *Int. J. Rem. Sens., 7 (9)*, pp 1153–1162.

[66] Raney, R.K., and R.T. Lowry, 1978; "Oceanic Wave Imagery and Wave Spectra Distortions by Synthetic Aperture Radar Imagery," 12^{th} *International Symposium on Remote Sensing of Environment*, Manila, Phillipines, 20–29 April, 1978, pp 683–702.

[67] Raney, R.K., and P.W. Vachon, 1987; "SAR Imaging of Ocean Waves from an Airborne Platform: Focus and Tracking Issues (Part I)," submitted to *IEEE Trans. Geoscience Rem. Sens.*.

[68] Raney, R.K., and G.J. Wessels, 1987; "Spatial Considerations in Speckle Simulation," *Proc. IGARSS '87 Symposium*, Ann Arbor, 18–21 May, 1987, pp 1341–1348.

[69] Rayleigh, J.W.S., 1896; *The Theory of Sound* 3rd ed., MacMillan, London.

[70] Rihaczek, A.W., 1969; *Principles of High-Resolution Radar* , McGraw-Hill Book Co., New York, 498p.

[71] Rice, S.O., 1944; 1945; "Mathematical Analysis of Random Noise," *Bell Syst. Tech. J., 23*, pp 282–352; *24*, pp 46–156.

[72] Shemdin, O.H. *et al*, 1986; *TOWARD Field Experiment Interim Report, Vol. I: Data Summary and Early Results, Vol. II: Contributions of Individual Investigators*, JPL.

[73] Shuchman, R.A., 1981; "Processing Synthetic Aperture Radar Data of Ocean Waves," in *Oceanography from Space*, J.F.R. Gower Ed., Plenum, New York, pp 477–496.

[74] Shuchman. R.A., and J.S. Zelenka, 1978; "Processing of Ocean Wave Data from a Synthetic Aperture Radar," *Boundary Layer Met., 13*, pp 181–191.

[75] Swerling, P., 1950; "Probability of Detection for Fluctuating Targets," *Rand Report, RM-1217*; reprinted in *IRE Trans., IT-6 (2)*, pp 269–308.

[76] Swerling, P., 1957; "Detection of Fluctuating Pulsed Signals in the Presence of Noise," *IRE Trans. Information Theory, IT-3 (3)*, pp 175–178.

[77] Swift, C.T. and L.R. Wilson, 1979; "Synthetic Aperture Radar Imaging of Moving Ocean Waves," *IEEE Trans. Antennas Propagat., AP-27 (6)*, pp 725–729.

[78] Tomiyasu, K., 1978; "Tutorial Review of Synthetic Aperture Radar (SAR) With Applications to Imaging of the Ocean Surface," *Proc. IEEE, 66 (5)*, pp 563–583.

[79] Tucker, M.J., 1985a; "The Imaging of Waves by Satelliteborne Synthetic Aperture Radar: The Effects of Sea-Surface Motion," *Int. J. Rem. Sens., 6 (7)*, pp 1059–1074.

[80] Tucker, M.J., 1985b; "The Decorrelation Time of Microwave Radar Echoes from the Sea Surface," *Int. J. Rem. Sens., 6 (7)*, pp 1075–1089.

[81] Ulaby, F.T., R.K. Moore, and A.K. Fung, 1982; *Microwave Remote Sensing Vols. I, II, and III*, Addison Wesley Publishing Co., Reading Mass., 2162p.

[82] Valenzuela, G.R., 1978; "Theories for the Interaction of Electromagnetic and Oceanic Waves—A Review," *Boundary Layer Met., 13*, pp 61–85.

[83] Vant, M.R., 1982; "A Spatially Variant Autofocus Technique for Synthetic Aperture Radar," *Proc. Radar '82, IEE Conf. Pub. No. 216*, pp 159–163.

[84] Vesecky, J.F., S.L. Durden, M.P. Smith, and D.A. Napolitano, 1984; "Synthetic Aperture Radar Images of Ocean Waves, Theories of Imaging Physics and Experimental Tests," *Proceedings of the URSI Commission F Symposium and Workshop*, Shoresh, Israel, May 14–23, 1984, pp 137–148.

[85] Vesecky, J.F., and R.H. Stewart, 1982; "The Observation of Ocean Phenomena Using Imagery from the SEASAT Synthetic Aperture Radar: An Assessment," *J. Geophys. Res., 87 (C5)*, pp 3397–3430.

[86] Wakasugi, K., N.-F. Kishi, and M. Matsuo, 1986; "A Three-Dimensional Formulation for Synthetic Aperture Radar Images of Ocean Waves in Orbital Motions," *IEEE Trans. Geoscience Rem. Sens., GE-24 (5)*, pp 732–737.

[87] Walsh, E.J., D.W. Hancock III, D.E. Hines, R.N. Swift, and J.F. Scott, 1985; "Directional Wave Spectra Measured with the Surface Contour Radar," *J. Physical Oceanography, 15 (5)*, pp 566–592.

[88] Woodward, P.M., 1953; *Probability and Information Theory, With Applications to Radar*, The MacMillan Company, New York, 128p.

[89] Wright, J.W., 1966; "Backscattering from Capillary Waves with Application to Sea Clutter," *IEEE Trans. Antennas Propagat., AP-14 (6)*, pp 749–754.

[90] Wright, J.W., 1968; "A New Model for Sea Clutter," *IEEE Trans. Antennas Propagat., AP-16 (2)*, pp 217–223.

[91] Zelenka, J.S., 1976; "A Comparison of Continuous and Discrete Mixed Integrator Processors," *J. Opt. Soc. Amer., 66 (11)*, pp 1295–1304.

A Simulation Methodology

Abstract

A two-dimensional SAR image simulation model developed for this research is discussed in this Appendix. The model is unique in that it explicitly considers the contribution of each target to the final image. System linearity is used to produce the complex image in a reasonably efficient manner. The simulation can vary the target density, models velocity bunching for an azimuthally travelling monochromatic wave, includes a processor focus error, and includes either point target accelerations or scene partial coherence.

A.1 Introduction

There are four main objectives for the SAR simulation model developed for this research. The first objective is to study the role of a variable target density upon SAR image statistics. Second is to study the detectability of a linear image feature in a nominally speckled background. Third is to study the velocity bunching mechanism for the imaging of azimuthally travelling surface gravity waves. The fourth main objective is to study the role of a finite scene coherence time in a velocity bunching model. The SAR simulation considered in this work is seen to be unique because the effect of each point target which constitutes the scene is explicitly considered. Such a simulation philosophy is in contrast with all other SAR simulation models [1,21,24,68,86]. Most simulations contain inherent assumptions of diffuse scattering (dense targets) and heavy post-detection image smoothing (no speckle-like processes).

The simulation is two-dimensional, although a one-dimensional simulation could be adequate to address many aspects of the stated objectives. However, a two-dimensional simulation yields imagery for explicit comparison with actual SAR imagery, allows evaluation on an image analysis system, and allows direct application of the statistical testing procedures developed elsewhere in this work.

A.2 Method

The simulation is designed to be as efficient as possible by taking advantage of the SAR system's linearity up to the point of detection. Thus, the complex "image" or complex look is the superposition of the appropriate complex impulse responses each weighted by the target's reflectivity[14] and intrinsic phase. Subsequently, the complex looks may be detected and summed to produce the real SAR image product. This impulse response superposition procedure nicely circumvents the need to generate new range-Doppler responses for each and every target and then perform the azimuthal compression. (The latter approach, if implemented, would be a very computationally expensive procedure.)

All targets subject to the same motion parameters will have the same complex impulse response for each look. Thus, a set of responses which adequately spans the range of motion parameters presented by the scene is pre-calculated and treated as a set of complex look-up tables. A field of static, fully coherent point targets requires only one such impulse response. A dynamic scene may require many.

Fig. 23 is a flow chart showing the major steps and components in the simulation sequence. These steps are now each briefly discussed.

A.2.1 The Simulation Parameter File

The simulation parameters are initially read from a disk file in three groups:

1. Scene Parameters

    - output grid size (generally 128-by-128 pixels)
    - target density (or set of densities)
    - target grid type
    - wavelength of a monochromatic azimuthally travelling wave Λ

[14] The reflectivity amplitude is proportional to the square-root of the radar cross-section.

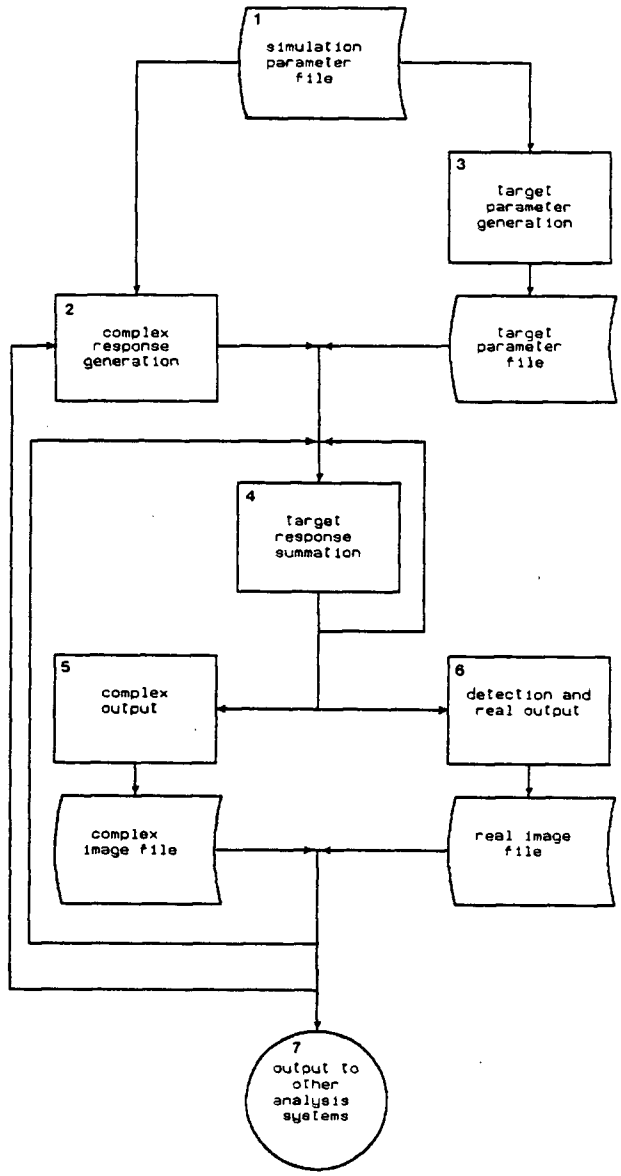

Figure 23: Simulation sequence flow chart.

- velocity bunching parameter α which implies the wave amplitude A
- mean scene coherence time τ_c

2. SAR Parameters

- platform velocity V
- platform height h
- radar wavelength λ
- angle of incidence γ
- available coherent integration time T
- Doppler bandwidth B
- pulse repetition frequency PRF

3. Processor Parameters

- azimuthal processor focus error η
- range processor focus error η_r
- number of looks processed N
- look overlap ξ
- interpolation factor ϵ_u
- decimation factor ϵ_d

Two SAR systems were simulated in this work: the satellite SEASAT L-band SAR processed on the GSAR; and the CCRS C-Band SAR processed on the C-SAR real-time processor. Nominal parameters used in the simulations for these SAR/processor combinations are listed in Table IX.

Table IX: Radar parameters relevant to the simulations.
SEASAT refers to the L-band SAR on the SEASAT satellite and the GSAR processor while, C-SAR refers to the C-band SAR on the CCRS Convair 580 aircraft and the real-time processor.

	SEASAT	C-SAR
V (m/s)	7200.	130.
h (m)	800,000.	3600.
γ	20°	$\sim 45°$
R_0 (m)	850,000.	5090.
λ (m)	0.235	0.050
T (s)	2.3	1.0
$T \cdot B$	2760.	130.
PRF (Hz)	1600.	$2.57V = 334.1$
N	4	7
ξ	0.42	0.12
ϵ_u	$\sqrt{2}$	1.
ϵ_d	4.	10.
f_s (Hz)	566.	33.4
Δx (m)	12.7	3.89
ρ_m (m)	24.	7.

A.2.2 Complex Impulse Response Generation

A series of complex impulse responses are pre-calculated and stored for each look generated. The number of responses generated depends upon the range of target accelerations and target coherence times presented by the scene. If scene coherence time is incorporated in a simulation run, the situation is assumed to be coherence time-limited so that processor and acceleration defocus are ignored. Up to eleven responses may be generated as required.

The complex azimuthal response used in this work is

$$g_c(t,t_i) = \frac{T}{\sqrt{2N^2 - j\epsilon}} \cdot \exp\left\{-2\pi(N^2-1)\frac{t_i^2}{T^2}\right\}$$
$$\cdot \exp\left\{-\pi\frac{B^2}{2N^2 - j\epsilon}\left[t - j\frac{2(N^2-1)}{TB}t_i\right]^2\right\}, \tag{110}$$

where the subscript c denotes the complex impulse response and $\epsilon = TB\delta\eta$. The focus perturbation in the case of a long coherence time is

$$\delta\eta = \eta - \hat{\eta} = \eta - \frac{aR_0}{V^2} \tag{111}$$

or, in the case of coherence time limited imaging, is

$$\delta\eta = \frac{2}{TB}\left(\frac{T}{\tau_c}\right). \tag{112}$$

That is, the mean first-order effects of a finite scene coherence time are modelled as a (possibly large) focus error. Such a focus error will likely violate $\delta\eta \ll 1$—an assumption used in the derivation of the impulse response. However, the expected behaviour of an individual response is consistent with the expected broadening in the face of a finite scene coherence time. Furthermore, the phase structure of this response preserves the system bandwidth and hence, the scene behaviour in the event of a large target density[15].

[15]Various other computationally efficient methods of modelling the finite scene coherence time were investigated including variation of the decimation rate. However, the bandwidth is generally not preserved as required. Short of explicit compression of each target's Doppler response, incorporation of a finite scene coherence time as a large focus error is a reasonable approach. The multi-look image represents the approximation of the finite scene coherence time. The individual looks of the multi-look set behave in a different manner for a coherence time error than for a focus error.

Several nonrestrictive assumptions are used in deriving the above form of the complex impulse response. These assumptions are matched filter processing, a large platform velocity implying no Doppler suppression, perpendicular antenna pointing, and a flat earth.

The look-centre-times are calculated by specifying the overlap of the equivalent rectangular width of the look-extraction windows. Then, we find

$$t_i = \left(\frac{1-\xi}{2}\right)(2i - N - 1)T_l \quad 1 \leq i \leq N \tag{113}$$

where ξ is the fractional window overlap and $T_l = T/\sqrt{2(N^2-1)}$ is the look-extraction window width.

The impulse response is generated at the sampling frequency

$$f_s = \mathrm{PRF}\frac{\epsilon_u}{\epsilon_d}\,, \tag{114}$$

where PRF is the radar pulse repetition frequency, ϵ_u is the processor interpolation factor, and ϵ_d is the processor decimation factor. The interpolation factor is occasionally applied prior to detection to avoid aliasing during the spectrum spreading detection operation, while the decimation factor is used to discard redundant information after look-extraction. An additional over-sampling factor arises (and is subsequently removed) by stepping through the look-up table. This permits freedom for accurate sub-pixel target placement.

The number of points generated for each impulse response is based upon twice the equivalent rectangular width of the detected multi-look impulse response. This could cause many zero contributions in the event of a large focus error. However, the relative look registration is preserved—a critical property to accurately maintain the multi-look system resolution. Representative examples of sets of impulse responses are shown in Fig. 24.

The complex range impulse response is generated using the above complex impulse response with $N = 1$, $t_i = 0$, $T = \sqrt{2}$, $B \rightarrow B/N$, and $\delta\eta = \eta_r$ (the range processor

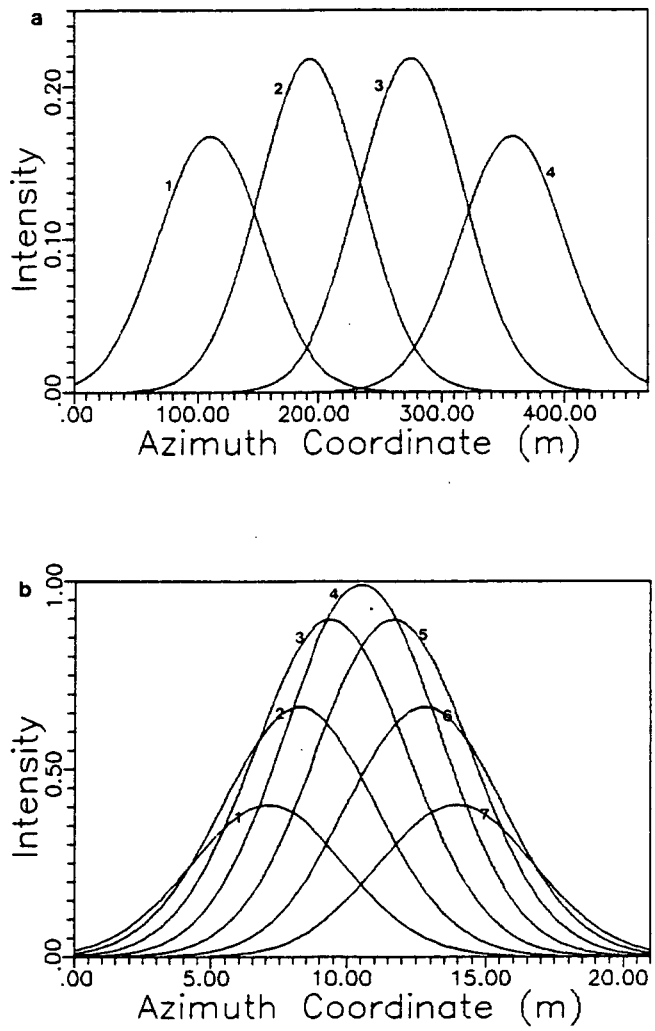

Figure 24: Representative examples of detected impulse responses.
a) The case of the SEASAT SAR, and b) the case of the CCRS C-band SAR each with $\eta = 0.05$.

focus error). Sampling is again at the rate f_s. The range impulse response has the same resolution as the multi-look azimuthal response and has unity amplitude. It is assumed that the scene does not contribute any range channel focus errors, and that there is no coherence time impact upon the range channel.

The two-dimensional complex impulse response is formed as the matrix product of the azimuthal and range responses.

A.2.3 Target Parameter Generation

The three target distributions currently available in the simulation are a regular grid, a random distribution, and a line of targets at an angle ϕ_l to the azimuth. The regular grid is generally used as a test pattern. For each target location generated, the target's radial velocity v, radial acceleration a, and coherence time τ are calculated. The velocity and acceleration are based upon the orbital motion of the azimuthally travelling wave. The coherence time is generated independently for each target based upon a Rayleigh distribution of coherence times with a mean of τ_c. The corresponding focus errors then follow the distribution

$$f_\eta(\eta) = \frac{2\pi}{\tau_c^2 B^2 \eta^3} \cdot \exp\left\{-\frac{\pi}{\tau_c^2 B^2 \eta^2}\right\} . \tag{115}$$

Focus errors are divided into eleven bins of equal probability ranging from 0.05 to 0.95. The azimuthal target location is shifted by the radial velocity component. The acceleration and coherence time are used to specify the appropriate response to select from the look-up table.

The target location and response parameters are stored in a target parameter disk file. This reduces the amount of core computer memory required since the simulation proceeds on a look-by-look basis requiring this information be retained for each look.

A.2.4 Response Summation

Each target is weighted by its reflectivity and intrinsic phase prior to summation into the complex grid. To date, the reflectivity used has always been unity since we are primarily interested in the dynamic effects. The intrinsic phase is assumed to be uniformly distributed on 0 to 2π from target-to-target and from look-to-look (even in the event of overlapping look-extraction windows).

A.2.5 Complex Output

The complex looks may be optionally output to the disk to permit later use for summation with other complex outputs. Such a procedure is possible because of the SAR's linear nature. Also, the complex looks may be output at any intermediate stage in the simulation. This permits, for example, a single run of ten targets per resolution element to provide any smaller target density case.

A line of point targets in a nominally diffuse background is generated by making two separate simulation runs and combining the complex outputs of each. The line and the background are each independently simulated. The line is weighted by its relative reflectivity $\sqrt{\sigma_{\text{rel}}}$ (based upon the mean value of the detected multi-look diffuse background) and each of the complex looks associated with the line are summed with the corresponding complex looks of the diffuse background.

A.2.6 Detection and Real Output

As an option, the detected real looks may be output to the disk along with the complex looks. The real outputs are generally scaled to between 0 and 255 in preparation for interpretation on an image analysis system.

A.2.7 Output to Other Analysis Systems

The simulation products may be output to any other systems and the detected products treated in the same manner as actual SAR imagery.

A.3 Implementation

The simulation was written in Fortran-77 and currently resides on the VAX 11-750 at the RADARSAT Project Office (RPO) in Ottawa, Ontario. The RPO system runs the VAX/VMS operating system and has an interactive Dipix Aries III image analysis work station. Original simulation development was on the VAX 11-750 at the Satellite Oceanography Lab at The University of British Columbia (Department of Oceanography) in Vancouver, British Columbia.

A.4 Future Extensions

Many enhancements could be incorporated relatively simply into the framework of the simulation developed thus far. For example, it is straightforward to include Doppler suppression for the case of an airborne SAR, range dependent radar cross-section modulation mechanisms so that off-azimuthally travelling waves may be imaged, a full spectrum of waves or at least several wave components, and variable/selectable target reflectivities. Such extensions would increase the simulation's flexibility and applications.

A.5 Conclusions

The simulation model presented in this Appendix is unique in its explicit treatment of each target which constitutes the scene being imaged. This approach allows point and diffuse targets (and all intermediate cases) to be simulated in exactly the same manner—that is, via explicit summation of the appropriately weighted and shifted complex impulse responses.

This model is applied to the simulation of several SAR image phenomena in Appendix B, and provides some rather insightful results. There are potential future applications as well. These could include, the *a priori* assessment of arbitrary SAR systems for ocean surface imaging, and the investigation of corrections for the system transfer function in the event of non-diffuse scattering.

B Simulation of SAR Image Phenomena

Abstract

Varying target densities and a linear target, consisting of a line of point targets, are investigated using the two-dimensional simulation model of Appendix A and the statistical analysis methodology of Chapter 7. It is shown that significantly different image statistics due to varying target densities are not necessarily accompanied by a noticeably different image appearance—a fact which suggests why ocean scattering is traditionally dismissed as being diffuse in nature.

A linear target composed of a line of discrete point targets is proposed as a model for a narrow "V" ship wake. The results of the statistical analysis are consistent with predictions if the linear target is oriented perpendicular to the channel in which the processor focus is perturbed.

B.1 Introduction

As an aid in understanding how a SAR images the ocean surface, a simulation model has been developed. This model is unique in that careful account is taken of the scattering nature; there are no *a priori* assumptions as to the statistical behaviour of each resolution element since each scattering centre is explicitly considered. In this Appendix, two experiments with this simulation model are outlined. The first addresses the scattering nature associated with Bragg resonant scattering while the second considers the imaging of narrow "V" ship wakes.

B.2 Varying Point Target Density

It is relatively well established that a dominant ocean surface scattering mechanism is Bragg resonant scattering [89]. It is also true that if a single coherent scattering centre dominates the return from a resolution cell, then the scattering is rather more coherent than diffuse. A single coherent patch of Bragg waves for a given resolution cell likewise results in a coherent specular-like return [64]. Thus, Bragg scattering is not necessarily equivalent to diffuse scattering, a position which is generally not taken [23]. Such specular occurrences impact both the way in which SAR imagery is formed, and quantitative measures derived from such SAR imagery.

This experiment with the simulation model is intended to help establish the relative

Table X: Scene simulation parameters (target density study).
Target densities and focus perturbations for a 128-by-128 pixel subscene with nominal SEASAT SAR parameters.

case	log(density)	density	number of targets	focus error	depth of focus	
					per look	multi-look
1	-1.0	0.10	460	0%	0	0
2	-0.8	0.16	729	1%	0.86	3.45
3	-0.6	0.25	1155	2%	1.73	6.90
4	-0.4	0.40	1831	3%	2.59	10.35
5	-0.2	0.63	2902	5%	4.31	17.25
6	0.0	1.00	4600			
7	0.2	1.58	7290			
8	0.4	2.51	11,555			
9	0.6	3.98	18,313			
10	0.8	6.31	29,024			
11	1.0	10.00	46,000			

density of ensembles of point targets for which specular or diffuse scattering properties dominate SAR imagery. The number of targets is varied in a controlled manner based upon the target density per N-look, zero focus-error resolution cell size. Each target is randomly positioned across the simulation region. The appropriate complex impulse response is weighted by its cross-section and its intrinsic phase, and is summed to produce N complex looks.

In this experiment, the target cross-sections are all chosen to be unity. This means that the results are best-case estimates for convergence towards diffuse scattering. (A distribution of target cross-sections would cause the scattering to retain aspects of a specular-like nature for larger scatterer densities.) The intrinsic phase is assumed to be distributed uniformly on 0 to 2π.

The target densities considered range from 0.1 to 10 targets per resolution cell and the azimuthal processor focus is varied through roughly 0, 1, 2, 3, and 5 depth of foci in each individual look for nominal SEASAT SAR parameters. Specific simulation values considered are listed in Table X and some representative outputs from the simulation model are shown in Fig. 25 and in Fig. 26. Plots of the image statistics considered,

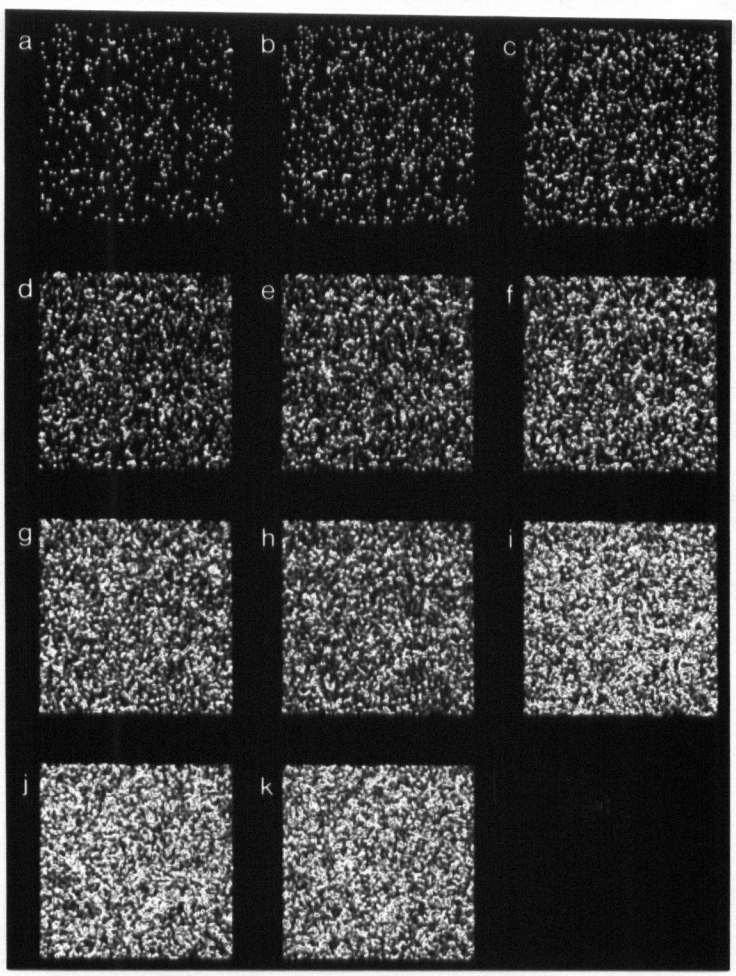

Figure 25: Variable target density simulation with $\eta = 0.00$.
The densities range from 0.1 (a) to 10 (k) targets per resolution element according to Table X.

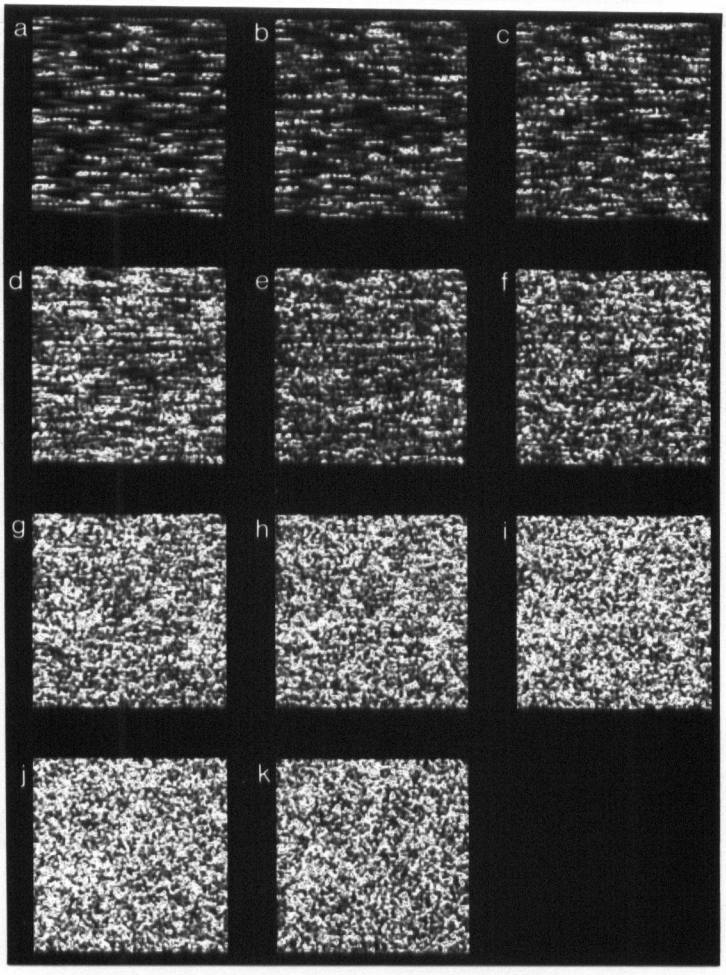

Figure 26: Variable target density simulation with $\eta = 0.03$.
The densities range from 0.1 (a) to 10 (k) targets per resolution element according to Table X.

specifically the inter-look cross-correlation coefficient, the scaling of peak-heights as looks are summed, and the image spectral width as a function of processor focus error are given in Fig. 27. The ideal behaviors are illustrated by the diffuse (dashed line) and specular (dotted line) cases included in Fig. 27b. It is apparent that the asymptotic behaviour of these cases is correct. However, it is equally apparent that these asymptotes are approached rather slowly. That is, even the extreme cases represented by 0.1 (nominally specular) and 10 (nominally diffuse) targets per resolution cell have not completely reached their limiting behaviors.

As may be judged from Fig. 25 and from Fig. 26, there is not a significant difference visually between the appearance of say, 0.63 targets per resolution cell (image e) and the denser cases considered in those figures. It is evident that significantly different image statistics are not necessarily accompanied by noticeably different image appearance. This suggests why even rather specular-like cases could be construed as being purely diffuse in nature on the basis of image appearance alone. Perhaps ocean reflectivity, dominated by Bragg resonant scattering, is often dismissed as being diffuse in nature since the imagery "looks" like it is derived from a diffuse scattering mechanism.

Bearing this assertion in mind, actual SAR ocean surface imagery may be subjected to the same analysis as has been done to the controlled simulated images to assess the true nature of Bragg resonant scattering.

B.3 Linear Targets

The imaging of ship wakes by SAR could prove to be a valuable tool in assessing SAR ocean imaging mechanisms. It is well established that ship wakes often manifest themselves as a bright narrow "V" pattern in SAR imagery, rather than as the classic Kelvin wake pattern, which is, in fact, rarely observed in SAR imagery. It has been established on the basis of group velocity versus ship velocity arguments and the opening angle of the "V" that this feature is a result of reflectivity from Bragg scale waves

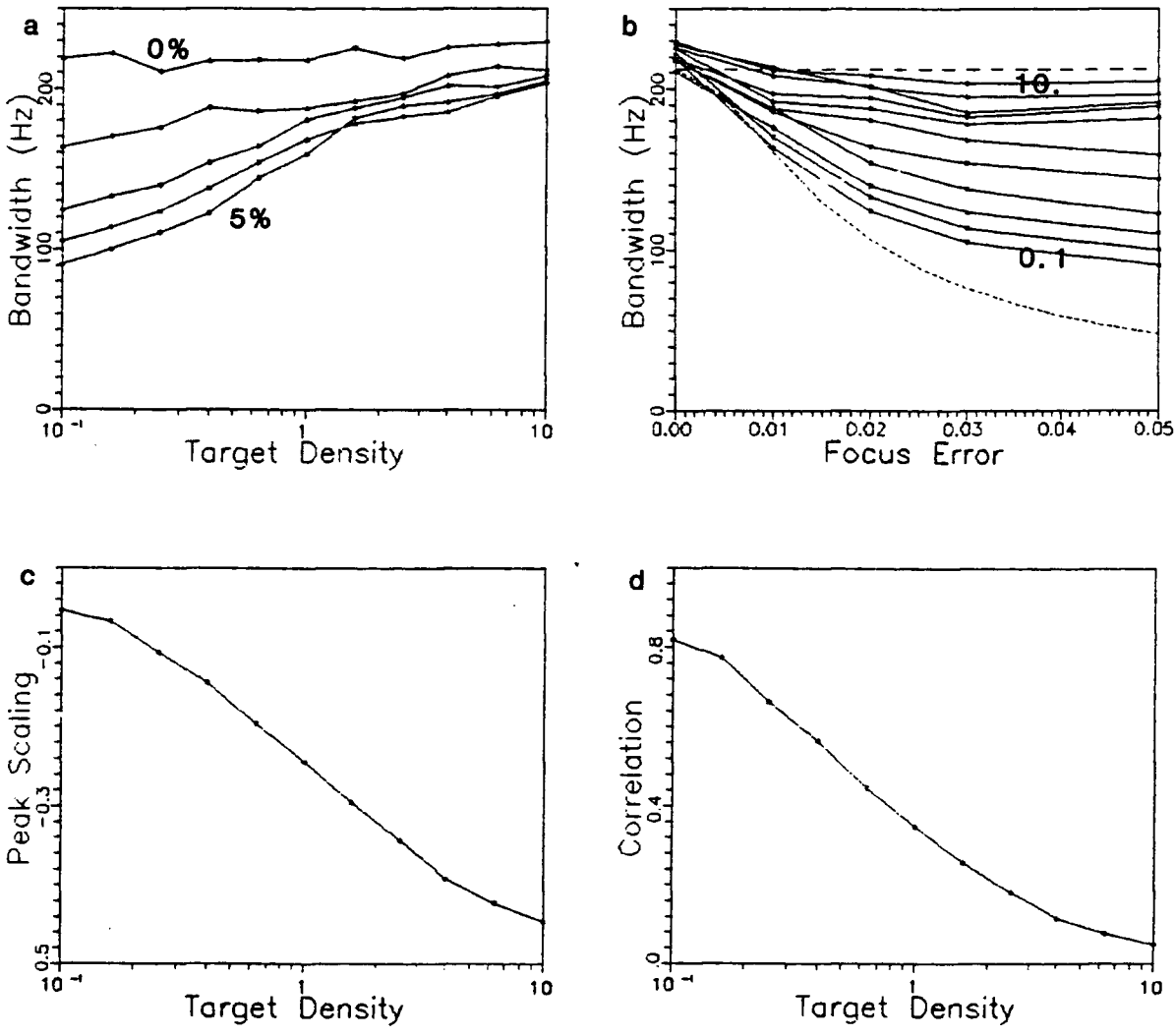

Figure 27: Derived statistics for variable target density.
a) Azimuthal image bandwidth as a function of target density, b) azimuthal image bandwidth as a function of processor focus error, c) peak-height scaling as a function of target density, and d) correlation as a function of target density.

produced by the passage of the ship [41]. This phenomena seems exclusively associated with nominally azimuthally travelling ships.

In this experiment with the simulation model, one arm of the narrow "V" ship wake is modeled as a linear target consisting of a line of coherent point targets. There are two objectives: first, to assess the detectability of such a well defined structure in a nominally speckled background subject to the chosen analysis methodology; and second, to assess the applicability of such a model and analysis to the narrow "V" wake problem.

In this experiment the linear target is composed of individual targets separated by a single resolution element. The complex linear target in zero background is first generated with unity cross-section and randomly distributed intrinsic phase at angles ranging from $\phi_l = 0°$ (along azimuth) to $\phi_l = 90°$ (along range) in 10° increments. Subsequently, the linear target is weighted and summed into the nominally diffuse complex background composed of 100 unity cross-section targets per resolution element. The weighting is based upon the single N-look resolution element being σ_{rel} dB above the mean background level, that is, the mean value of the nominally diffuse, multi-look background scene. The cross-sections considered range from $\sigma_{\text{rel}} = 0$ dB to $\sigma_{\text{rel}} = 10$ dB in 1 dB increments. The simulation is again subjected to the processor focus errors of Table X. Examples of these simulation outputs are given in Fig. 28 and in Fig. 29.

Plots of the statistics for the linear target in zero background, that is, the infinite signal-to-noise ratio case, are shown in Fig. 30. The plot of azimuthal image bandwidth versus linear target angle in Fig. 30b appears to be tending towards zero bandwidth at $\phi_l = 0°$ (*i.e.* azimuthally oriented). However, for small angles this trend disappears since the bandwidth has become a measure of the structure along the linear target. Note that the separation between the curves (Fig. 30a) and the sensitivity to focus (Fig. 30b) are reduced as the linear target becomes azimuthally oriented. The sensitivity is best, and in fact compares with the 0.1 target per resolution cell case of Fig. 27b, for the

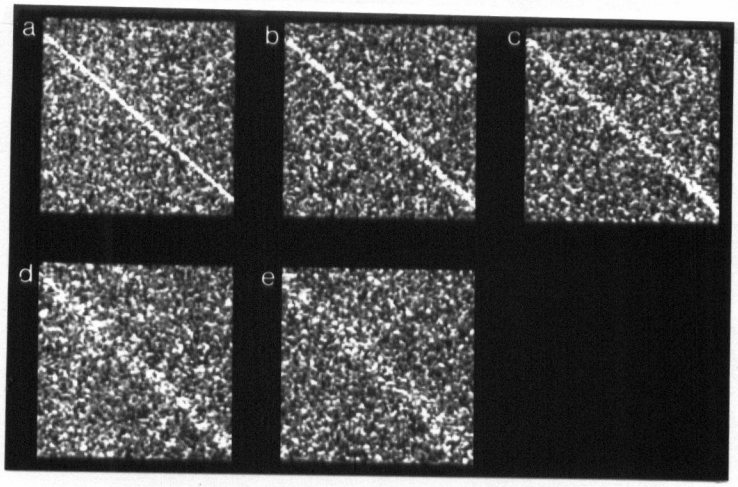

Figure 28: Variable focus error linear target simulations.
The case of $\phi_l = 40°$, $\sigma_{\text{rel}} = 8$ dB, and the five focus errors considered ranging from $\eta = 0.00$ (a) to $\eta = 0.05$ (e) according to Table X.

range oriented linear target.

This lack of sensitivity for the azimuthally oriented linear target is unfortunate since all observed cases of narrow "V" wakes are azimuthally oriented. However, in the event of a static target, as is very nearly the case with the Bragg scale waves, the range and azimuthal SAR channels are logically interchangeable. Thus, focus sensitivity tests may be performed using the range channel with no loss in generality. In this case, the sensitivity to focus will correspond to the most sensitive case presented (given an equivalent time-bandwidth product). The peak-height scaling and correlation measures are not affected by such considerations since they are based upon nominally zero focus-error cases.

Fig. 31 shows the analysis results for the linear target of varying orientations, cross-sections, and azimuthal focus-errors in the case of a nominally diffuse background. It is apparent that although the results are tending towards those of Fig. 30 as the cross-section σ_{rel} increases, they do so rather slowly. In the case of the azimuthally oriented

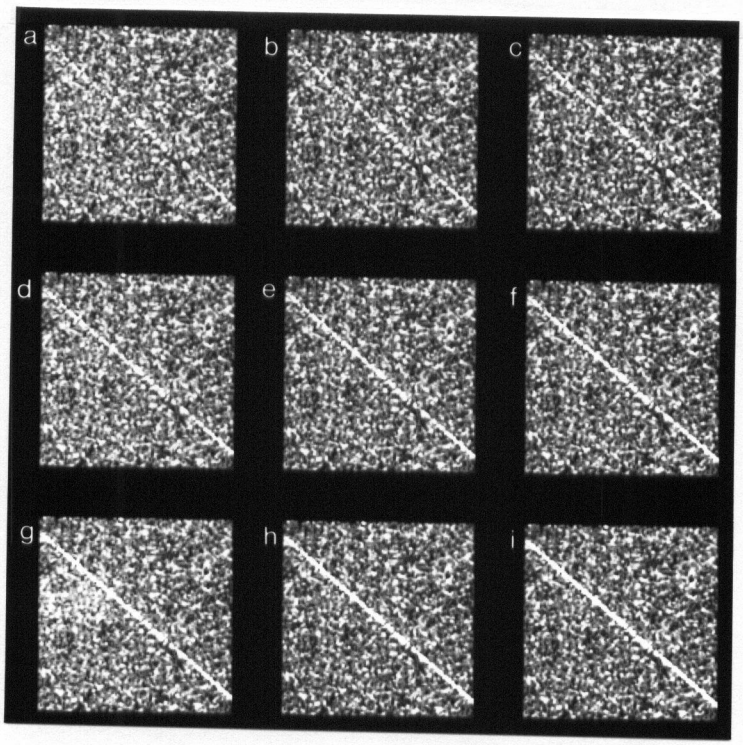

Figure 29: Variable relative cross-section linear target simulations.
The case of $\phi_l = 40°$, $\eta = 0.00$, and σ_{rel} ranging from 0 dB (a) to 8 dB (i) in 1 dB increments.

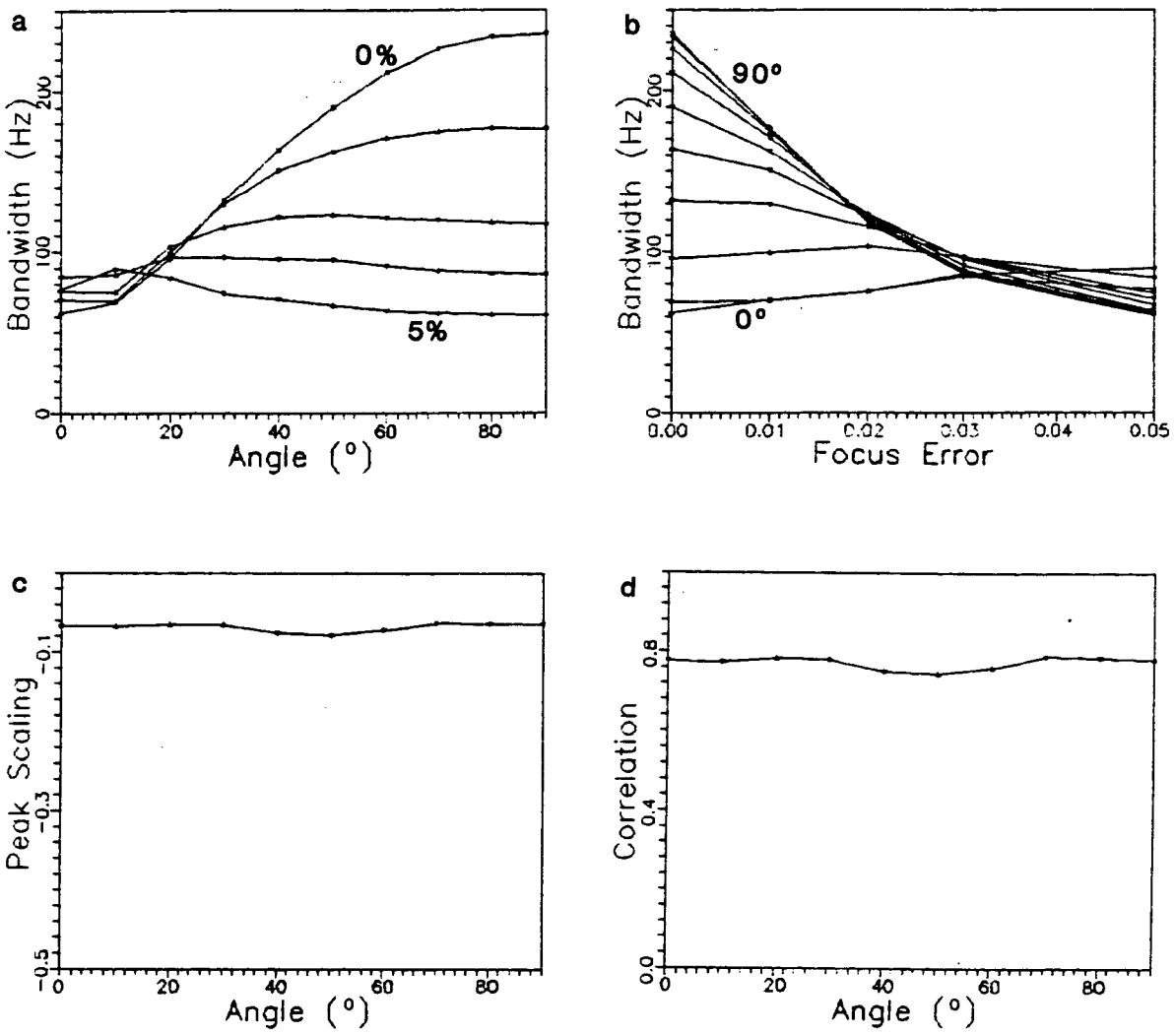

Figure 30: Derived statistics for linear targets in zero background.
a) Azimuthal image bandwidth as a function of linear target angle, b) azimuthal image bandwidth as a function of processor focus error, c) peak-height scaling as a function of linear target angle, and d) correlation as a function of linear target angle.

Table XI: Scene simulation parameters (linear target study).
Target densities along the azimuthally oriented linear target and range channel focus perturbations for a 128-by-128 pixel subscene with nominal SEASAT SAR parameters.

case	log(density)	density	error	depth focus
1	-0.6	0.25	0%	0
2	-0.3	0.50	0.5%	1.06
3	0.0	1.00	1.0%	2.12
4	0.3	2.00	1.5%	3.18
5	0.6	4.00	2.5%	5.30

linear target, Fig. 31a(i) shows the image bandwidth measure decreasing with increasing cross-section. This is due to the structure along the linear target dominating the width measure as the linear target emerges above the background speckle pattern. In the case of the range oriented linear target, Fig. 31a(iv) shows that the width measure is responding to the linear target broadening as the processor focus is perturbed. Fig. 31b and Fig. 31c further illustrate the slow tendency towards the behaviour of the linear target in zero background as shown in Fig. 30a and in Fig. 30b. The peak-height scaling and correlation measures of Fig. 31d and of Fig. 31e are essentially independent of linear target orientation, but again, are only slowly approaching their anticipated specular-like behaviour as the linear target cross-section increases.

With these results in mind, two further cases were simulated to observe the sensitivity to target density within the linear target. The linear target is fixed at $\phi_l = 0°$ (azimuthally oriented) and the cross-section set to $\sigma_{\text{rel}} = 8$ dB. The target densities considered range from 0.25 to 4 targets per resolution element and the range and azimuthal processor focus is varied through roughly 0, 1, 2, 3, and 5 depth of foci. Specific values considered are listed in Table XI. Note that the smaller time-bandwidth product associated with the range channel, coupled with one-look range processing, imposes a stricter tolerance on the focus error than in the range channel. Some representative outputs from the simulation model are shown in Fig. 32.

Fig. 33 shows the analysis results for the linear target of varying point target den-

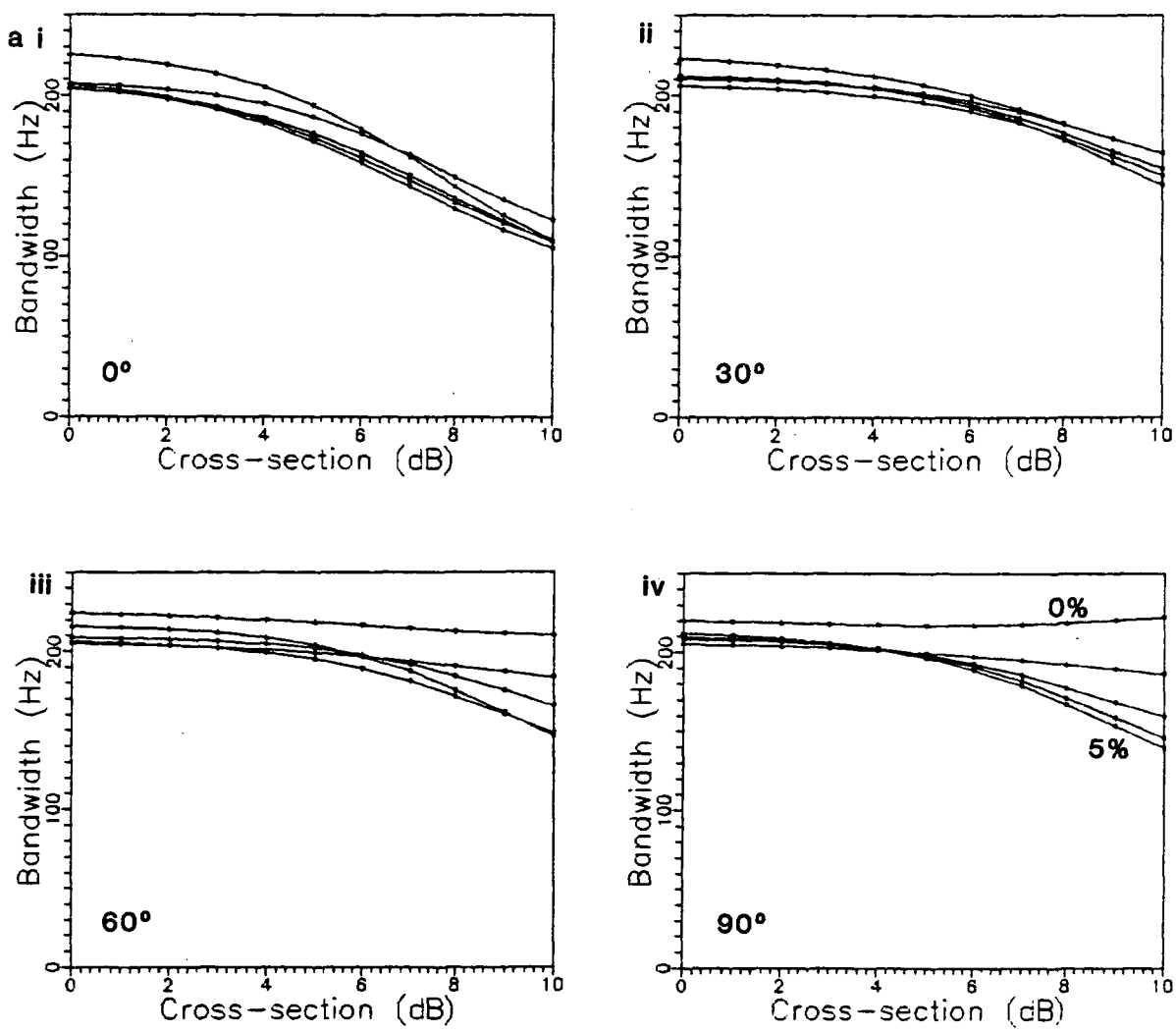

Figure 31: Derived statistics for linear targets in a diffuse background.
a) Azimuthal image bandwidth as a function of linear target cross-section for various target angles at various azimuthal processor focus errors. (continued)

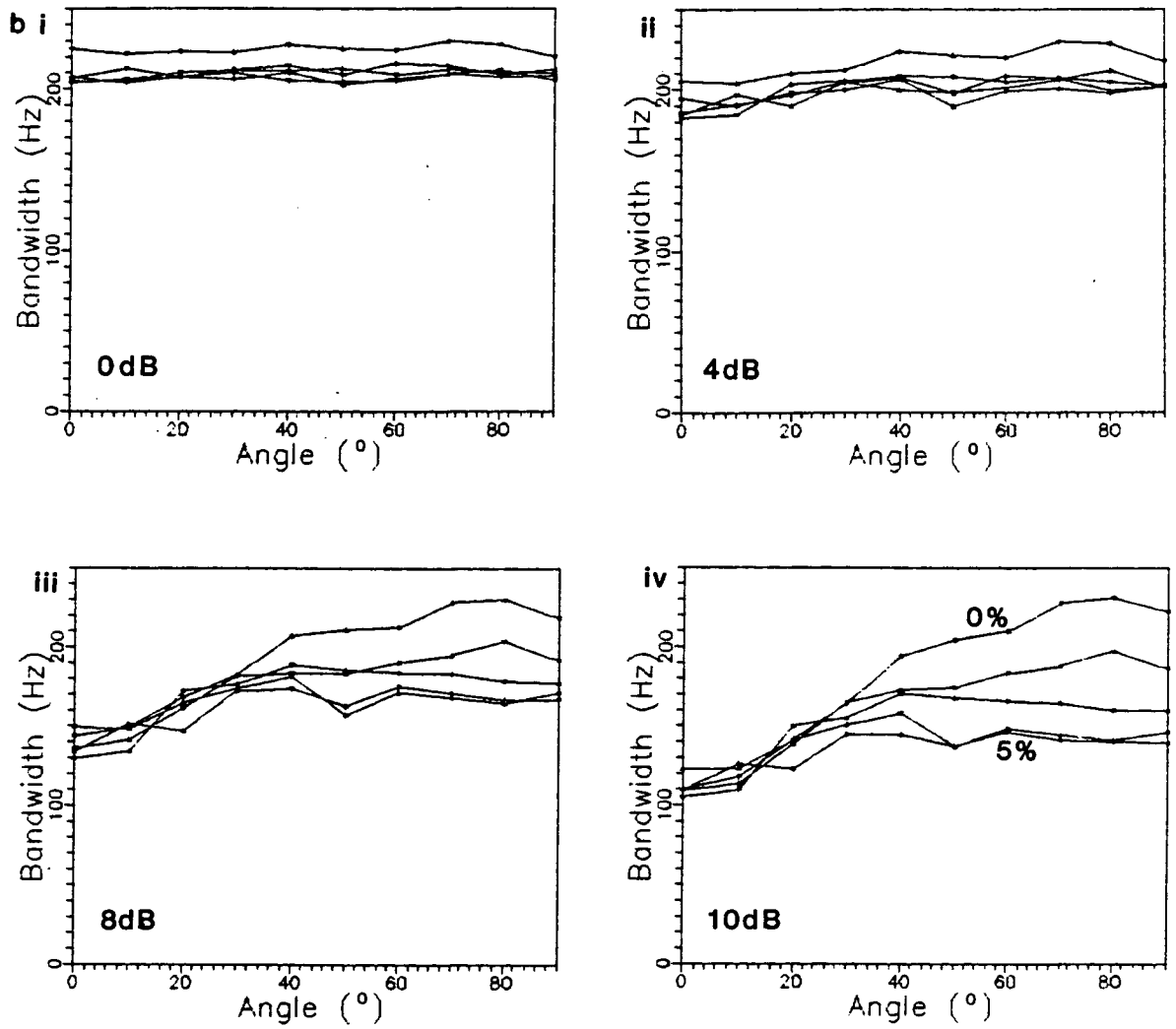

Figure 31: Continued.
b) Azimuthal image bandwidth as a function of target angle for various azimuthal processor focus errors at various target cross-sections. (continued)

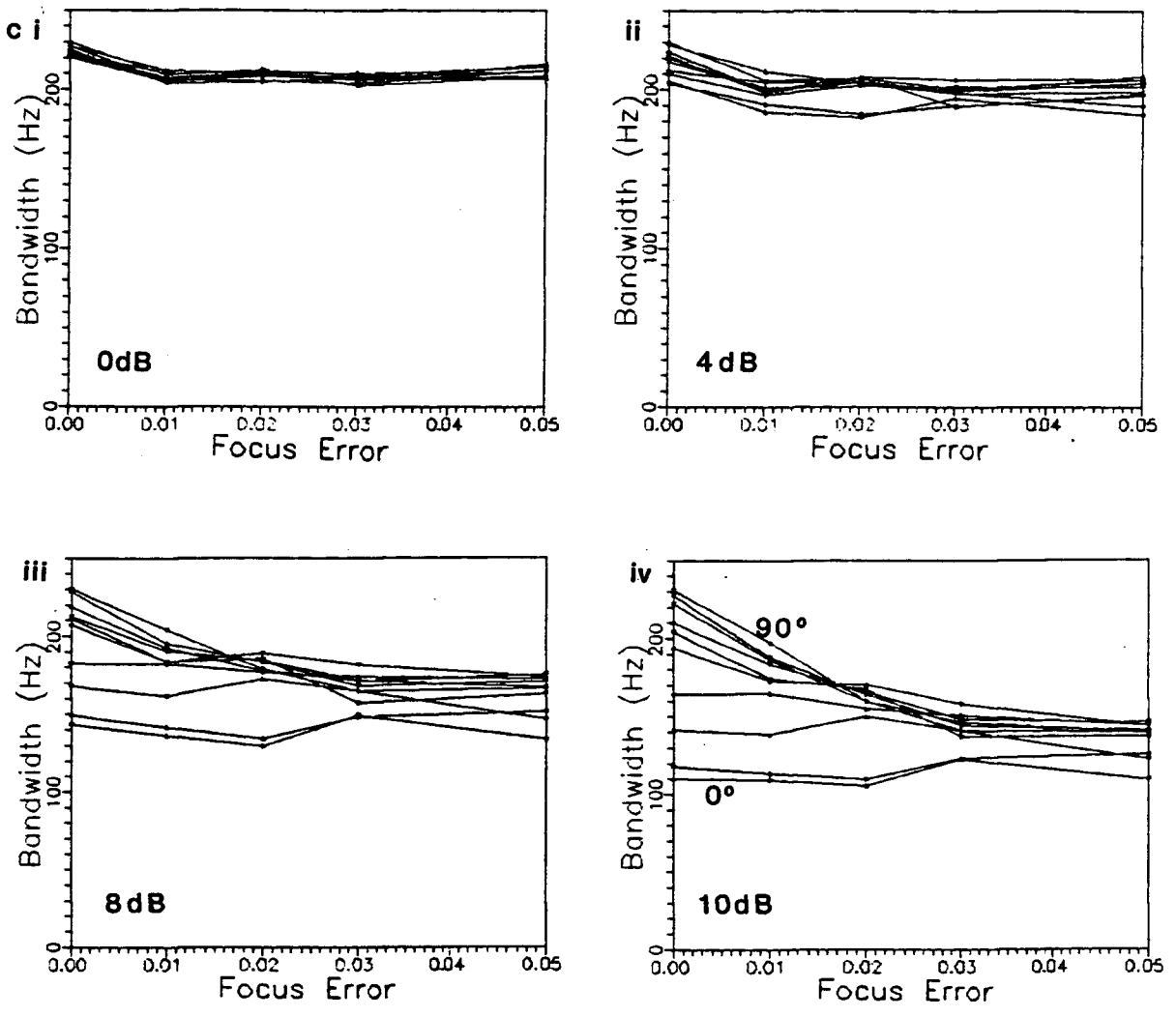

Figure 31: Continued.

c) Azimuthal image bandwidth as a function of azimuthal processor focus error for various target angles at various target cross-sections. (continued)

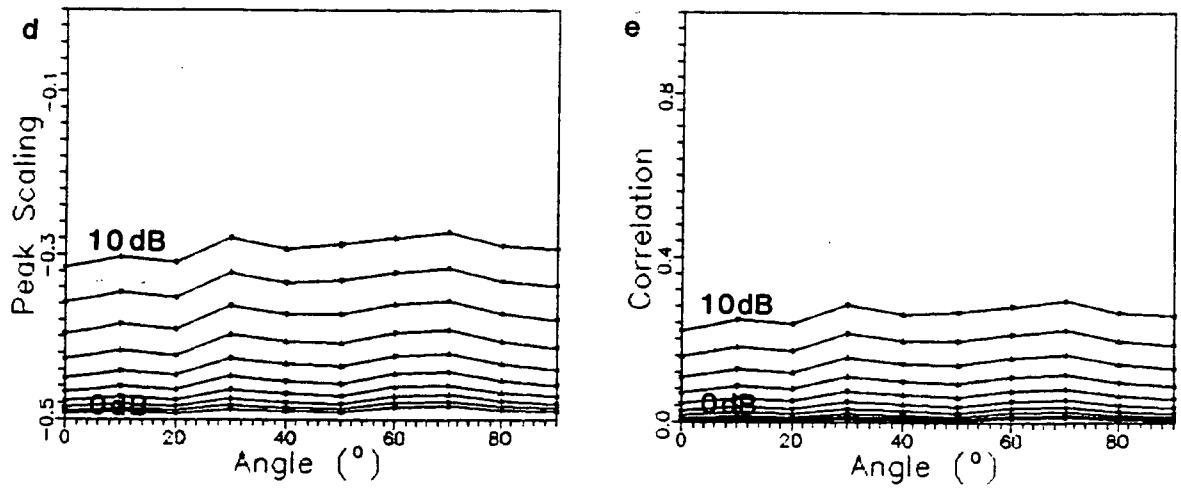

Figure 31: Continued.
d) Peak-height scaling as a function of linear target angle, and e) correlation as a function of linear target angle.

sity with azimuthal and range processor focus errors. It is of note that there is almost no focus error sensitivity along the linear target (*i.e.* in azimuth) while there is high sensitivity in range. However, the sensitivity to a range focus error is essentially independent of the actual point target density within the linear target. This is expected since in the case of a focus error, the linear target is being subjected to a broader point spread function. Then, as long as the individual target's cross-sections are large relative to the mean speckle-noise level, the measured spectral width in range will decrease with increasing focus error.

Bearing these results in mind, the SAR imagery of narrow "V" ship wakes may be subjected to the same analysis methodology, that is, introduction of a focus error in range followed by a rangeward image bandwidth measurement. A similar pattern of responses would suggest that the Bragg resonant scattering associated with narrow "V" ship wakes is the result of specular-like scattering. This result could be generalized to any ocean surface Bragg-scale structure since an identical dispersion relationship is

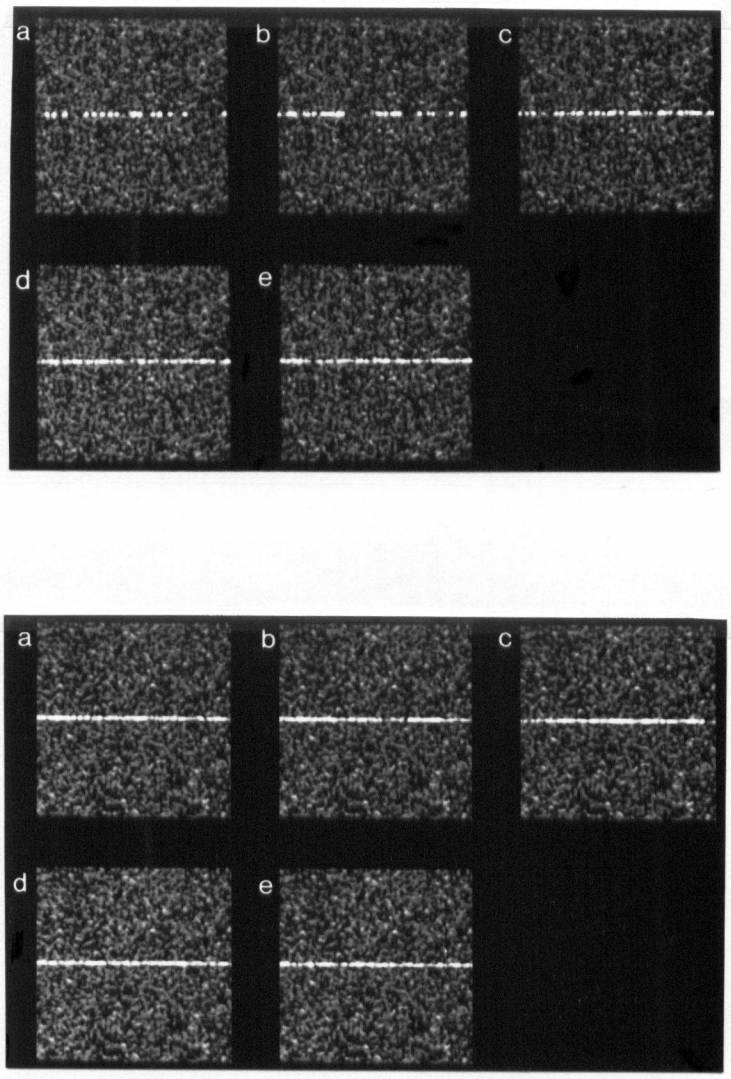

Figure 32: Variable point target density linear target simulations.
The case of varying point target density with I) no processor focus errors, II) azimuthal processor focus errors ranging from $\eta = 0.00$ (a) to $\eta = 0.05$ (e) according to Table X. (continued)

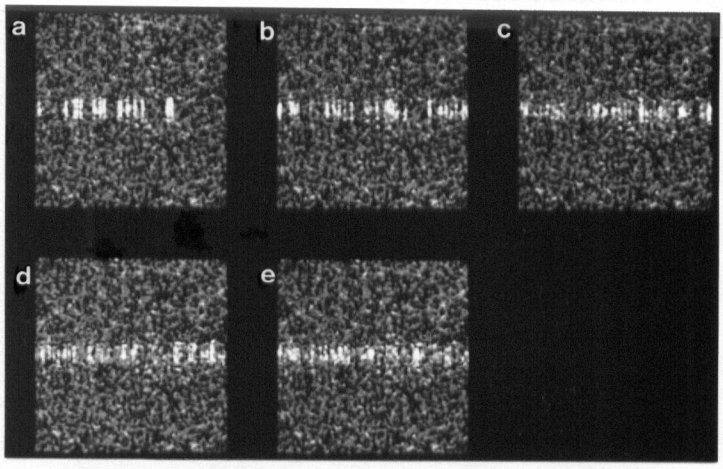

Figure 32: Continued.
III) Range processor focus errors ranging from $\eta_r = 0.00$ (a) to $\eta_r = 0.025$ (e) according to Table XI.

obeyed for any ocean surface roughness of this scale.

B.4 Conclusions

This Appendix has presented simulation results and corresponding statistics for two SAR image phenomena.

The first phenomenon is the case of a varying target density. Simulated target densities ranging from 0.1 to 10. targets per resolution element have demonstrated that:

1. A target density of 0.1 targets per resolution element (nominally a point target) does not behave in a completely specular manner.

2. A target density of 10. targets per resolution element (nominally a diffuse target and well above the classical guideline of 5 [34]) does not behave in a completely diffuse manner.

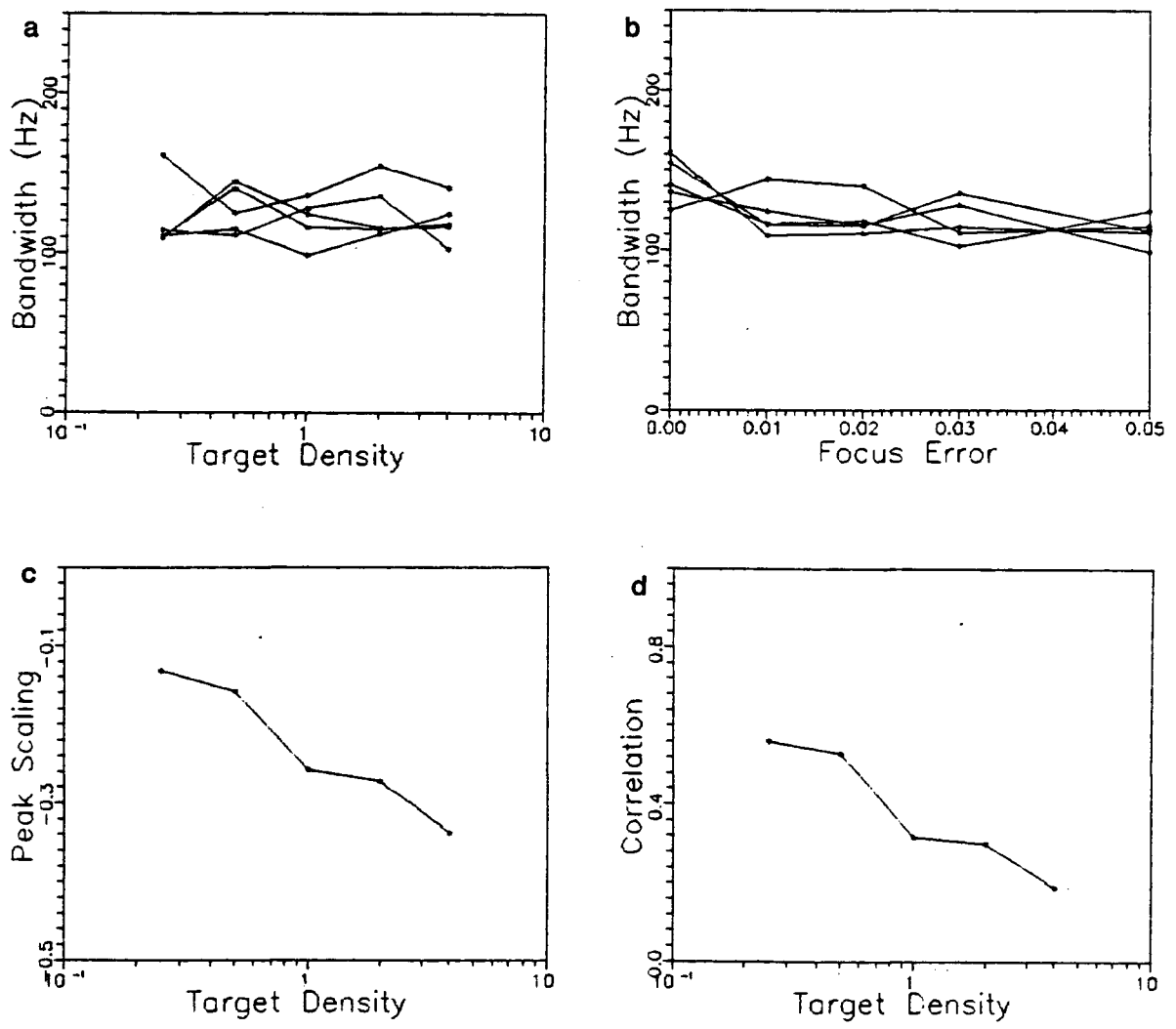

Figure 33: Derived statistics for linear target of varying point target density. a) Azimuthal image bandwidth as a function of point target density for the various azimuthal processor focus errors, b) azimuthal image bandwidth as a function of azimuthal processor focus error for the various target densities, c) peak-height scaling as a function of point target density, and d) correlation as a function of point target density in a nominally diffuse background. (continued)

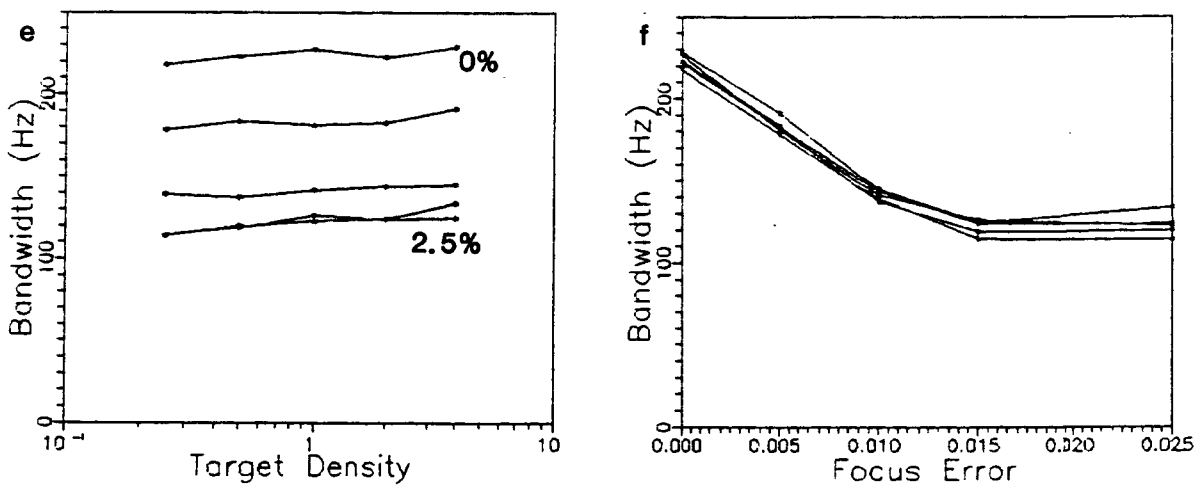

Figure 33: Continued.
e) Rangeward image bandwidth as a function of point target density for the various range processor focus errors, and f) rangeward image bandwidth as a function of range processor focus error for the various target densities in a nominally diffuse background.

3. Significantly different image statistics due to different target densities are not necessarily accompanied by noticeably different image appearance.

The second phenomenon is the case of a linear target consisting of a line of discrete point targets. This target is proposed as a model for one arm of a narrow "V" ship wake. The methodology to perform a comparison between this model and actual SAR imagery of a ship wake exists, but thus far, appropriate SAR data has been unavailable. It is also shown that the range channel focus, rather than the azimuthal channel focus, should be perturbed to maximize the sensitivity of the statistical measures.

C Actual SAR Image Data Sets

Abstract

The two types of actual SAR imagery used in the comparisons in this work are discussed in this Appendix: the first, is satelliteborne SAR imagery from the SEASAT SAR processed to four complex looks on the GSAR processor; and the second, is airborne SAR imagery from the CCRS C-band SAR processed to seven looks on the real-time processor. Difficulties in processing the data are discussed, particularly subtleties in processing the complex looks.

C.1 SEASAT SAR

The L-band SAR on the SEASAT satellite provides the most extensive satellite SAR data set available to date (and available for the next several years). The SEASAT satellite system became operational in July 1978 and ceased operation after about 100 days due to an electrical failure. Despite such a short operational time span, and requirements of direct transmission of raw signal data to one of five ground receiving stations, the available SEASAT SAR data set is rather extensive [59].

C.1.1 SEASAT SAR Processing

All of the SEASAT SAR imagery used in this work was processed on an MDA GSAR processor at either MDA or CCRS. The data is required as individual detected looks for the prescribed statistical tests. Unfortunately, the GSAR cannot directly provide such a data product. Instead, the processor must be halted prior to the detection and look-sum module, and each of the looks extracted in their complex form. The looks may be subsequently registered, interpolated, and detected to provide the individual looks suitable for the testing procedure.

The look-detection procedure was performed upon 128-by-128 (post interpolation) pixel sized subscenes. The interpolation requires some care due to the GSAR's range-segment mode of operation [9]. The data is sectioned into segments of range data, and a single compression filter matched to the centre of the range segment is used to

compress all of the azimuthal lines in the segment. Focus errors resulting from range changes towards the edges of the segments lead to several problems in the resulting imagery. The GSAR tolerates broadening of the individual responses due to the focus error, and it corrects azimuthal shifts due to the focus errors by physically shifting the azimuthal lines back into alignment. The GSAR accounts for large phase rotations across range segment seams due to a large net focus error by using two interpolation procedures: first, a complex cubic convolution resampling is used within the segments; and second, a nearest neighbor resampling is used near the segment seams. This procedure is used because the phase rotation across the seam, in conjunction with the complex cubic convolution resampling, results in a loss of signal energy along the seam. This interpolation procedure was duplicated prior to detecting the extracted subscenes. These phase rotations must be considered when dealing with complex imagery produced by a processor operating in such a mode.

C.1.2 Selected SEASAT Scenes

Three SEASAT SAR scenes were chosen for this work:

1. The Irish Sea off Ballyquinton Point (orbit 633, provided by RAE) contains examples of various ships and their wakes. The data was processed through to a multi-look image, and is only used for qualitative comparisons with linear target simulations.

2. Goldstone, California (orbit 882, provided by CCRS) contains many features of interest. A corner reflector array provides examples of point targets while regions of desert provide examples of diffuse targets. The scene was chosen to supply control data for the statistical analysis work.

3. Duck Island, North Carolina (orbit 1339, provided by CCRS), known as Duck-X, has been subjected to intense study because of its ocean wave imagery [6,7]. This

scene was chosen as the test scene for the analysis methodology.

Scenes 2 and 3 were each processed five times with focus errors of 0%, 1%, 2%, 3%, and 5%.

C.2 C-SAR

The C-band SAR on the CCRS Convair 580 marked its first operational use during the recent LIMEX/LEWEX experiments which took place off the east coast of Newfoundland over the Labrador Sea [15]. One objective of this experiment was to image ocean waves as they propagate from the open ocean into ice covered regions.

C.2.1 C-SAR Processing

The C-SAR has a real-time processor which produces a seven look, square-root mapped image. The C-SAR system can also store the raw signal data on high density digital tape for subsequent processing on the GSAR. Unfortunately, this system was not enabled for the scenes of interest for this work. Thus, the individual looks are not available from this data set.

C.2.2 Selected C-SAR Scenes

Two scenes were selected from the LIMEX/LEWEX data set:

1. 87-03-13 (Line 10 Pass 8) contains examples of open ocean waves propagating into an ice covered region. The waves are at about 45° to the azimuth.

2. 87-03-14 (Line 10 Pass 1) contains an example of nearly azimuthally oriented waves propagating through an ice covered region.

These scenes were processed in narrow-swath mode, meaning that the near scene edge is at an incidence angle of 45°. A 16 km ground range swath is imaged.

C.3 Conclusions

This Appendix has discussed the preprocessing of and indicated the scenes chosen from the actual SAR image data sets considered in this work. Some care is required in dealing with the complex SEASAT imagery due to the range-segment GSAR processing. Three SEASAT scenes were chosen: one contains examples of narrow "V" ship wakes; another contains examples of static point and diffuse targets; and the last contains an arbitrary ocean scene showing ocean waves. The C-SAR imagery is more straightforward to deal with. Two scene were chosen which show ocean surface waves propagating through an ice-covered region.

D One-Dimensional Velocity Bunching Simulations

Abstract

This Appendix presents an idealized one-dimensional velocity bunching simulation model designed to study the contrast of a scene produced by velocity bunching. The simulation is over one cycle of an azimuthally travelling monochromatic wave and includes acceleration defocus, Doppler suppression, and finite scene coherence time. It is demonstrated that acceleration defocus and Doppler suppression may be important in some cases, and oppose the effects of velocity bunching. Furthermore, a finite scene coherence time can smooth the cusped wave image and can obliterate the possible double-peaked nature of some images.

D.1 Introduction

The objective of this simulation work is to systematically study the roles of target acceleration, Doppler suppression, and a finite scene coherence time upon the velocity bunching wave imaging mechanism. The simulation performs a pseudo-convolution of the detected impulse response over a dense, uniform array of point targets. We term the procedure a pseudo-convolution because the appropriate impulse response varies from target-to-target dependent upon the motion parameters. Thus, fast convolution techniques may not be used.

This simulation procedure, while straightforward to implement, has several inherent assumptions which could prove to be limiting. Only the mean contrast is considered so that a large target density is coupled with heavy averaging. The one-dimensional procedure is related to the two-dimensional point-by-point simulation developed in Appendix A by integrating the two-dimensional simulation in range (or more generally in the direction of the wave crests). This removes the effects of the target density leaving only the mean contrast function (providing the area integrated over is large).

The one-dimensional simulation procedure developed has similarities to the one-dimensional Monte-Carlo simulations of Alpers [1]. However, there are departures from Alpers' work in several key areas. One departure is that we treat only a single cycle of a monochromatic wave rather than a full wave spectrum. While this simulation is

not restricted to monochromatic waves, this approach permits the explicit assessment of the roles of specific parameters to velocity bunching. On the other hand, Alpers was interested in studying the modulation transfer function which relates the radar image to the ocean wave field.

Another departure from Alpers' work is that we include a finite scene coherence time while Alpers did not. Alpers has since recognized the role of the scene coherence time and it has been included in his subsequent two-dimensional simulation work [2].

D.2 Method

The one-dimensional simulation proceeds by generating a monochromatic azimuthally travelling surface gravity wave consisting of a large number of point targets uniformly spaced at locations t_j and each having unity cross-section. Associated with each point target is a specific radial velocity component v_j and radial acceleration component a_j based upon the wave's orbital motion, and an average scene coherence time τ_c. The appropriate (expected) detected impulse response $g^j_{md}(t)$ is generated for each target along the wave. Included in the impulse response are the azimuthal shift, acceleration defocus, Doppler suppression, and finite scene coherence time. Each impulse response contribution is summed to produce the final SAR image.

The output image is

$$g(t) = \sum_j g^j_{md}(t_j - t) \ , \tag{116}$$

where each target which contributes energy to the output at time t is included in the sum (including contributions from targets on adjacent wavelengths). The impulse response of the j^{th} target is given by

$$g^j_{md}(t) = \frac{T^2}{2\sqrt{N^2 + (TB\hat{\eta}_j/2)^2 + (T/\tau_c)^2}} \cdot \exp\left\{-\pi \frac{t^2_{Dj}}{T^2}\right\}$$

$$\cdot \exp\left\{-2\pi \frac{B^2}{N^2 + (TB\hat{\eta}_j/2)^2 + (T/\tau_c)^2}\left[t + \left(1 - \frac{\hat{\eta}_j}{2}\right) t_{Dj}\right]^2\right\} \ , \tag{117}$$

Table XII: One-dimensional simulation parameters for C-SAR.

Fig. 34	α	A	a	D	$T/N\tau$	τ (msec)	C
a (i)	$1/3\pi$	0.90	no	no	~ 0	$\gg T$	1.858
(ii)	$1/2\pi$	1.34	no	no	~ 0	$\gg T$	7.070
(iii)	$1/\pi$	2.69	no	no	~ 0	$\gg T$	3.326
b (i)	$1/\pi$	2.69	no	no	~ 0	$\gg T$	3.326
(ii)	$1/\pi$	2.69	yes	no	~ 0	$\gg T$	2.729
(iii)	$1/\pi$	2.69	no	yes	~ 0	$\gg T$	2.947
(iv)	$1/\pi$	2.69	yes	yes	~ 0	$\gg T$	2.431
c (i)	$1/2.5\pi$	1.08	no	no	~ 0	$\gg T$	3.199
(ii)	$1/2.5\pi$	1.08	yes	no	~ 0	$\gg T$	2.825
(iii)	$1/2.5\pi$	1.08	no	yes	~ 0	$\gg T$	3.321
(iv)	$1/2.5\pi$	1.08	yes	yes	~ 0	$\gg T$	2.929
d (i)	$1/2.5\pi$	1.08	no	no	~ 0	$\gg T$	3.199
(ii)	$1/2.5\pi$	1.08	no	no	1	140	2.845
(iii)	$1/2.5\pi$	1.08	no	no	2	70	2.308
(iv)	$1/2.5\pi$	1.08	no	no	3	47	1.887
(v)	$1/2.5\pi$	1.08	no	no	4	35	1.575
(vi)	$1/2.5\pi$	1.08	no	no	5	28	1.335
(vii)	$1/2.5\pi$	1.08	no	no	10	14	0.673
(viii)	$1/2.5\pi$	1.08	no	no	15	9	0.364
(ix)	$1/2.5\pi$	1.08	no	no	20	7	0.190

where $\hat{\eta}_j = a_j R_0/V^2$ and $t_{Dj} = v_j R_0/V^2$. The impulse response is augmented by selectively enabling the acceleration defocus contribution $\hat{\eta}_j$ and the Doppler suppression contribution (the first exponentiation) in order to directly assess the effects of these terms.

D.3 Results

Simulations using the radar parameters of Appendix A were performed. The results are summarized in Table's XII and XIII and in Fig.'s 34, 35, and 36. For each configuration, simulations were performed to demonstrate the role of four parameters: first, the role of α showing one-to-one, critical, and many-to-one mapping regimes; second, the role of acceleration defocus and Doppler suppression in the many-to-one mapping case; third, the role of acceleration defocus and Doppler suppression in a near

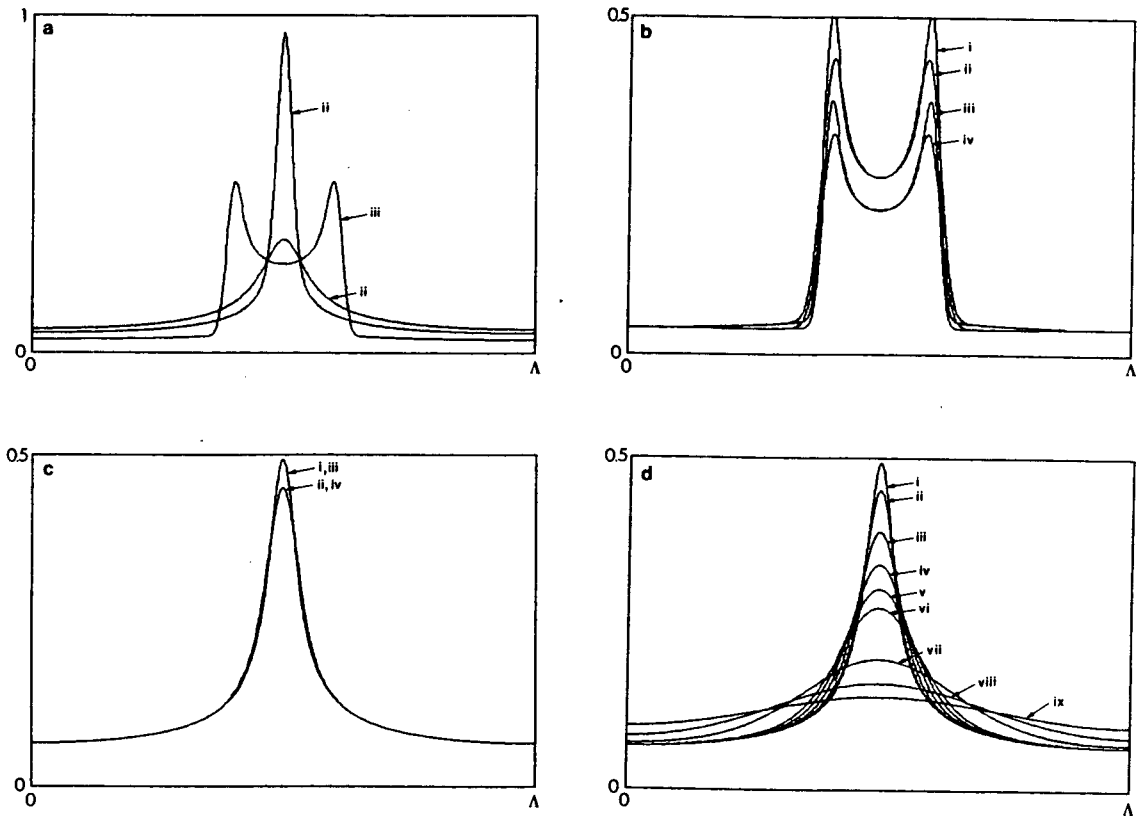

Figure 34: Results of one-dimensional simulations for C-SAR.

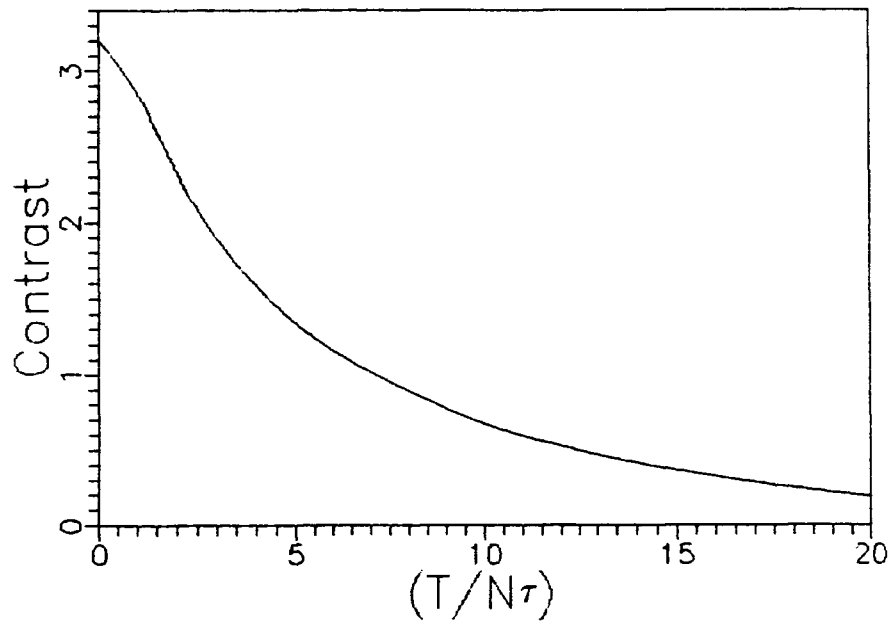

Figure 35: Degradation in contrast as a function of coherence time for C-SAR.

Table XIII: One-dimensional simulation parameters for SEASAT.

Fig. 36	α	A	a	$T/N\tau$	τ (msec)	C
a (i)	$1/3\pi$	0.23	no	~ 0	$\gg T$	1.271
(ii)	$1/2\pi$	0.35	no	~ 0	$\gg T$	2.519
(iii)	$1/\pi$	0.70	no	~ 0	$\gg T$	1.673
b (i)	$1/\pi$	0.70	no	~ 0	$\gg T$	1.673
(ii)	$1/\pi$	0.70	yes	~ 0	$\gg T$	1.532
c (i)	$1/2.5\pi$	0.28	no	~ 0	$\gg T$	1.742
(ii)	$1/2.5\pi$	0.28	yes	~ 0	$\gg T$	1.567
d (i)	$1/2.5\pi$	0.28	yes	~ 0	$\gg T$	1.567
(ii)	$1/2.5\pi$	0.28	yes	0.94	575	1.294
(iii)	$1/2.5\pi$	0.28	yes	1.88	288	0.898
(iv)	$1/2.5\pi$	0.28	yes	9.40	58	0.001

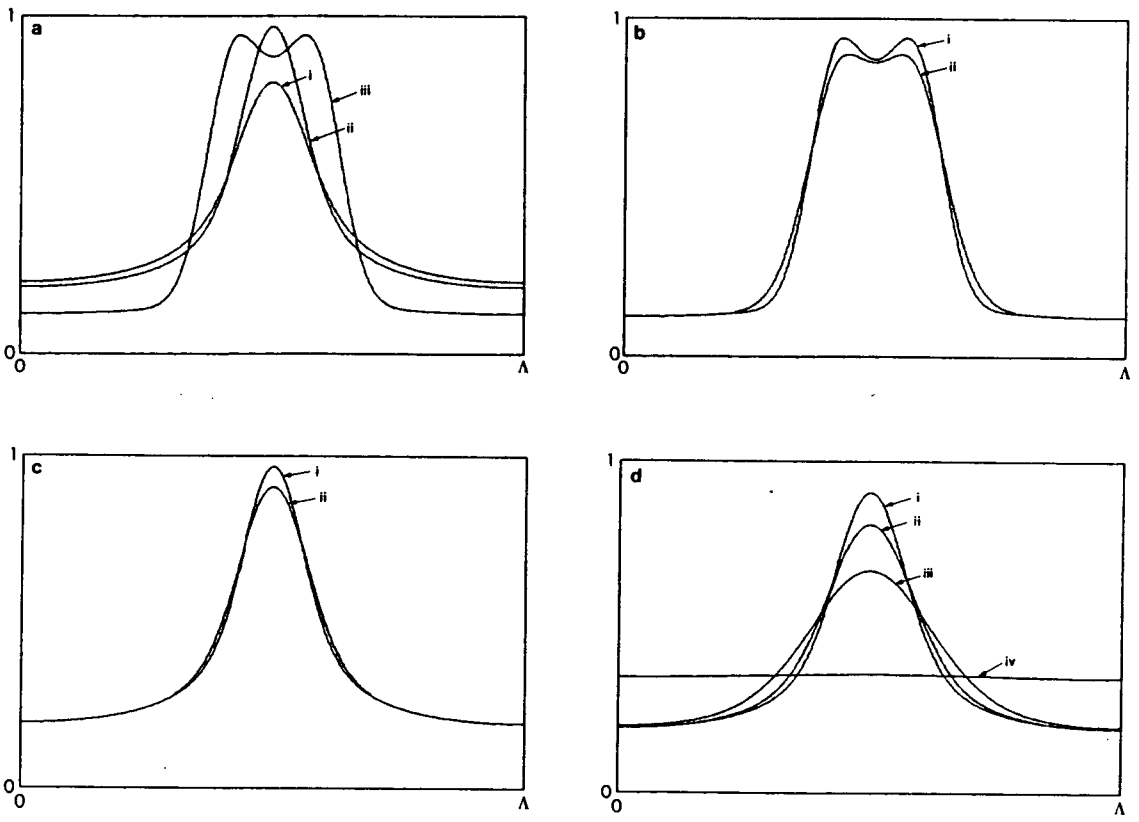

Figure 36: Results of one-dimensional simulations for SEASAT.

critical one-to-one mapping case; and fourth, the role of a finite scene coherence time. For each simulation, a wavelength of 150 m was chosen. As well, $\alpha = 1/2.5\pi$ was chosen for the one-to-one mapping case. The contrast measure used in this work is

$$C = \frac{I_{\text{peak}} - I_{\text{mean}}}{I_{\text{mean}}}, \tag{118}$$

where the I's are the indicated intensity values. Note that it is not relevant to directly compare the contrast of the double peaked cases to the single peaked cases.

D.4 Conclusions

Using the one-dimensional velocity bunching simulation we have demonstrated that:

1. Target acceleration-induced defocus will smooth a cusped peak in a velocity bunching model.

2. Doppler suppression will reduce the maximum intensity, but may not reduce the contrast. Doppler suppression is only important if the platform velocity is relatively slow. Thus, its impact will be more apparent (and critical) in airborne SAR ocean imagery than in similar imagery from a satellite SAR.

3. A finite scene coherence time will smooth a cusped peak and may completely obliterate a double peak.

We have also judged the parameters which are relevant and should be included in the two-dimensional simulation. A coherence time of 14 msec is acceptable for C-SAR, but 60 msec may be too short for the imaging of azimuthally travelling waves by SEASAT.

E Estimation of the System Transfer Function

Abstract

The system transfer function (STF) is required to correct wave spectra derived from SAR ocean imagery. A new approach to estimating the STF is to defocus a portion of the wave image to simulate a large, diffuse target rather than to use a different nominally smooth diffuse scene. The concept is shown to work well with a 5% focus error for a $\sim$ 200 m azimuthal wave component in SEASAT SAR imagery.

E.1 Introduction

Ocean wave spectra derived from SAR imagery require correction for the system transfer function (STF) to allow reliable extraction of ocean wave properties [6]. The procedure involves division of the image spectrum by a replica of the spectrum of an impulse response. The impulse response spectrum, the spectrum of the perfect focus processor response to a stationary point target, has been shown to be proportional to the speckle spectrum, the spectrum of the response to a nominally diffuse target [63]. This normalization procedure "whitens" the effect of the speckle noise which may then be removed by subtraction of an easily calculated bias value [17].

The usual procedure for estimating the STF involves calculation of the spectrum of a nominally diffuse scene [6,7,8,45,46]. Unfortunately, this requirement could lead to complications in that a known, large, diffuse target is required. That target should be from the same SAR, recorded at the same ground station, and the imagery produced on the same processor. Furthermore, the example of a diffuse target should be gathered at about the same instant in time to ensure reliable estimation of the STF. In the past, the diffuse target constraint has been satisfied by a fetch-limited body of water. Such a scene is difficult to find for open ocean cases.

E.2 Method

A new approach to the calculation of the STF hinges upon the fact that as the processor focus is perturbed, the scene contrast is lost at the processor output. The

output becomes diffuse in nature—that is, a uniform speckle pattern is created.

Thus, the scene in use for calculation of the ocean wave spectrum could be reprocessed with a focus error to produce the uniform speckle pattern, the output of a nominally diffuse target. This approach to estimating the STF has the advantage that it is not necessary to find an example of a diffuse target which satisfies the previously mentioned constraints. As long as the focus perturbation is large enough, all the contrast in the processor output will be obliterated, and the STF may be reliably calculated.

The necessary focus error can be estimated from the equation for focus limited resolution, which is

$$\rho_m = \frac{V}{B}\frac{(TB)\eta}{2} . \tag{119}$$

If the azimuthal resolution cell dimension is of the order of the azimuthal wavelength component imaged we find, for SEASAT SAR parameters and a wavelength of 200 m, that $\eta \sim 0.024$ or a 2.4% error in the processor's azimuthal FM rate will suffice.

E.3 Example

This procedure was performed upon a sample of the azimuthal spectrum of SEASAT SAR imagery from orbit 1339. The imagery was available with azimuthal focus errors of 0% and 5%. Fig. 37 shows the results of using a smoothed version of the azimuthal spectrum with a 5% focus error to normalize the spectrum calculated from the 0% focus error case (solid line). This normalization compares well with the normalization based upon a nominally diffuse section of desert scene from the Goldstone California orbit 882 scene (dashed line). The differences between the two spectra in Fig. 37 are small, and may not be statistically significant.

E.4 Conclusions

This approach to the calculation of the STF would seem to be feasible. The disadvantage is that the scene must be processed twice. However, only a relatively small

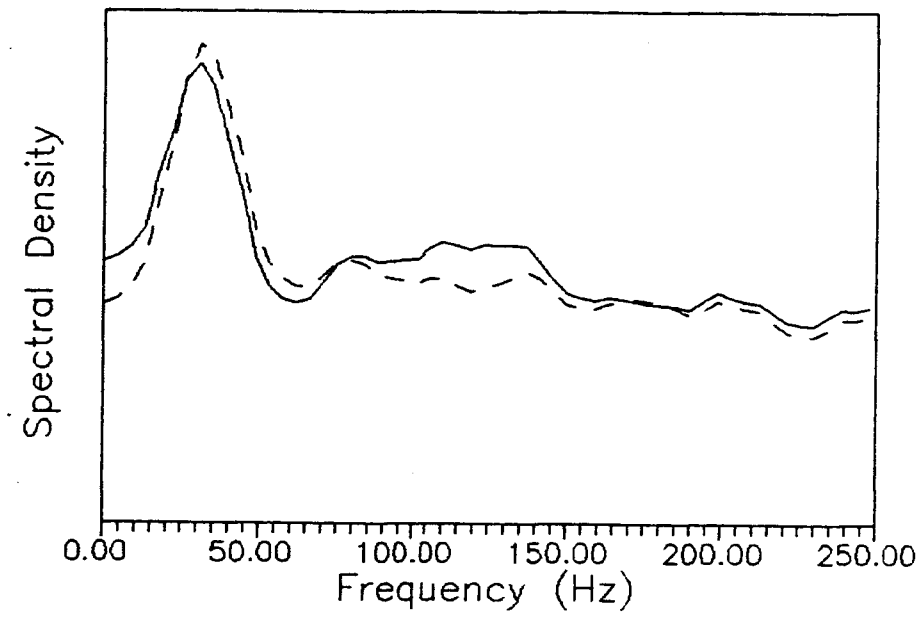

Figure 37: Azimuthal spectrum corrected for STF.
The solid line is the result of using the 5% focus error case for normalization while the dashed line is the result of using a nominally diffuse region of the Goldstone scene. The azimuthal wavenumber coordinate in cycles per meter is found through division by V. The peak corresponds to about a 220 m wavelength.

region need be reprocessed with a focus error, or perhaps a post-compression refocussing scheme could be used if the complex image data is available [83]. Note that the reprocessed version must have a focus perturbation in both the azimuth and the range to remove the STF effects in both image dimensions.